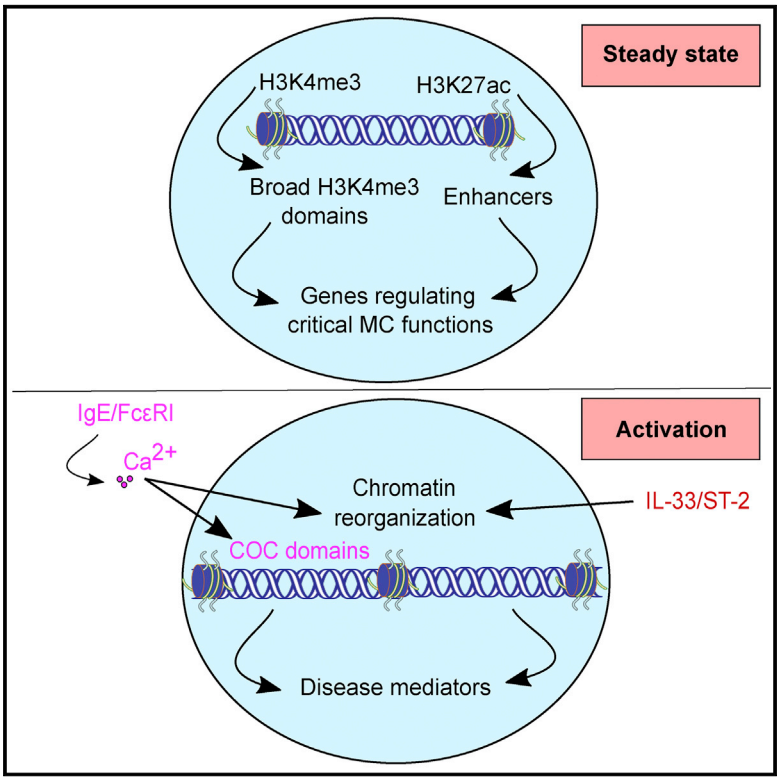
Resource

Immunity

Genome-wide Analyses of Chromatin State in Human Mast Cells Reveal Molecular Drivers and Mediators of Allergic and Inflammatory Diseases

Graphical Abstract



Authors

Gökhan Cildir, John Toubia, Kwok Ho Yip, ..., Michele A. Grimbaldeston, Angel F. Lopez, Vinay Tergaonkar

Correspondence

vinayt@imcb.a-star.edu.sg

In Brief

Cildir et al. map the genomic and transcriptomic changes in human mast cells upon diverse stimuli, defining chromatin changes associated with activation and Ca^{2+} flux and revealing potential effectors of mast cell function. Disease-associated SNPs mapped onto *cis*-regulatory regions of mast cells suggest that mast cell function may impact a broad range of pathologies.

Highlights

- Enhancers and broad H3K4me3 domains are enriched in genes regulating MC functions
- Intracellular calcium levels govern the chromatin landscape upon FcεRI crosslinking
- Disease-associated SNPs are enriched in regulatory chromatin regions of human MCs

Cildir et al., 2019, Immunity *51*, 949–965
November 19, 2019 © 2019 Elsevier Inc.
https://doi.org/10.1016/j.immuni.2019.09.021

CellPress

Immunity
Resource

Genome-wide Analyses of Chromatin State in Human Mast Cells Reveal Molecular Drivers and Mediators of Allergic and Inflammatory Diseases

Gökhan Cildir,[1,2] John Toubia,[1,3] Kwok Ho Yip,[1] Mingyan Zhou,[1] Harshita Pant,[5] Pravin Hissaria,[6] Jingxian Zhang,[4] Wanjin Hong,[4] Nirmal Robinson,[1] Michele A. Grimbaldeston,[7] Angel F. Lopez,[1] and Vinay Tergaonkar[1,2,8,9,*]
[1]Centre for Cancer Biology, University of South Australia and SA Pathology, Adelaide, SA 5000, Australia
[2]Laboratory of NF-κB Signaling, Institute of Molecular and Cell Biology (IMCB), 61 Biopolis Drive, Proteos, Singapore 138673, Singapore
[3]ACRF Cancer Genomics Facility, Centre for Cancer Biology, University of South Australia and SA Pathology, Adelaide, SA 5000, Australia
[4]Institute of Molecular and Cell Biology (IMCB), 61 Biopolis Drive, Proteos, Singapore 138673, Singapore
[5]School of Medicine, University of Adelaide, Adelaide, SA, Australia
[6]Royal Adelaide Hospital, Adelaide, SA 5000, Australia
[7]OMNI-Biomarker Development, Genentech Inc, South San Francisco, CA 94080, USA
[8]Department of Pathology, Yong Loo Lin School of Medicine, National University of Singapore, Singapore 119074, Singapore
[9]Lead Contact
*Correspondence: vinayt@imcb.a-star.edu.sg
https://doi.org/10.1016/j.immuni.2019.09.021

SUMMARY

Mast cells (MCs) are versatile immune cells capable of rapidly responding to a diverse range of extracellular cues. Here, we mapped the genomic and transcriptomic changes in human MCs upon diverse stimuli. Our analyses revealed broad H3K4me3 domains and enhancers associated with activation. Notably, the rise of intracellular calcium concentration upon immunoglobulin E (IgE)-mediated crosslinking of the high-affinity IgE receptor (FcεRI) resulted in genome-wide reorganization of the chromatin landscape and was associated with a specific chromatin signature, which we term Ca^{2+}-dependent open chromatin (COC) domains. Examination of differentially expressed genes revealed potential effectors of MC function, and we provide evidence for fibrinogen-like protein 2 (FGL2) as an MC mediator with potential relevance in chronic spontaneous urticaria. Disease-associated single-nucleotide polymorphisms mapped onto *cis*-regulatory regions of human MCs suggest that MC function may impact a broad range of pathologies. The datasets presented here constitute a resource for the further study of MC function.

INTRODUCTION

Allergic diseases such as asthma, allergic rhinitis (hay fever), atopic dermatitis (eczema), and food allergies afflict millions of individuals worldwide, and a large number of immunomodulatory molecules are causally linked to allergic symptoms in the skin, lung, and gastrointestinal tract (de Kleer et al., 2016; Lyons and Milner, 2018; Tordesillas et al., 2017). In these diseases, *in situ* recognition of allergens, processing of allergic peptides by antigen-presenting cells, generation of a predominant T helper 2 (Th2)-type cell response, and production of allergen-specific immunoglobulin E (IgE) by class-switched B cells represent the chain of events in an allergen-specific immune response (Platts-Mills and Woodfolk, 2011). IgE binding to the high-affinity IgE receptor (FcεRI) on target cells such as mast cells (MCs) and basophils sensitizes these cells to subsequent exposure to specific antigens that crosslink FcεRI molecules in the membrane (Galli and Tsai, 2012).

MCs are tissue-resident immune cells with important roles in innate and adaptive immune responses. MCs contain cytoplasmic granules that store bioactive molecules including, but not limited to, proteases, cytokines, and biologically active amines (Cildir et al., 2017). Diverse stimuli trigger MC activation through IgE-dependent or -independent mechanisms in different pathologies (McNeil et al., 2015; Redegeld et al., 2018; St John and Abraham, 2013). IgE-mediated FcεRI crosslinking is the most common initiator of MC activation during allergic responses. In certain individuals, anaphylactic responses resulting from the crosslinking of FcεRIs turn fatal due to uncontrolled release of MC mediators. In addition, cytokines such as interleukin (IL)-33 also regulate MC functions (Cayrol and Girard, 2018).

Organization of the chromatin landscape is an important mechanism in controlling cell-type-specific functions in the immune system (Beyaz et al., 2017; Bunting et al., 2016; Johnson et al., 2018). Enhancers are important *cis*-regulatory elements typically located far away from transcriptional start sites (TSSs) and characterized by the presence of specific post-translational modifications of histones and nucleosome-depleted regions. Enhancers positively regulate gene expression by long-range interactions with the gene promoters (Long et al., 2016) and play central roles in cellular differentiation and function. Lineage-specific or signal-activated transcription factors (TFs) bind to enhancers and regulate the recruitment of other co-factors and the general transcriptional

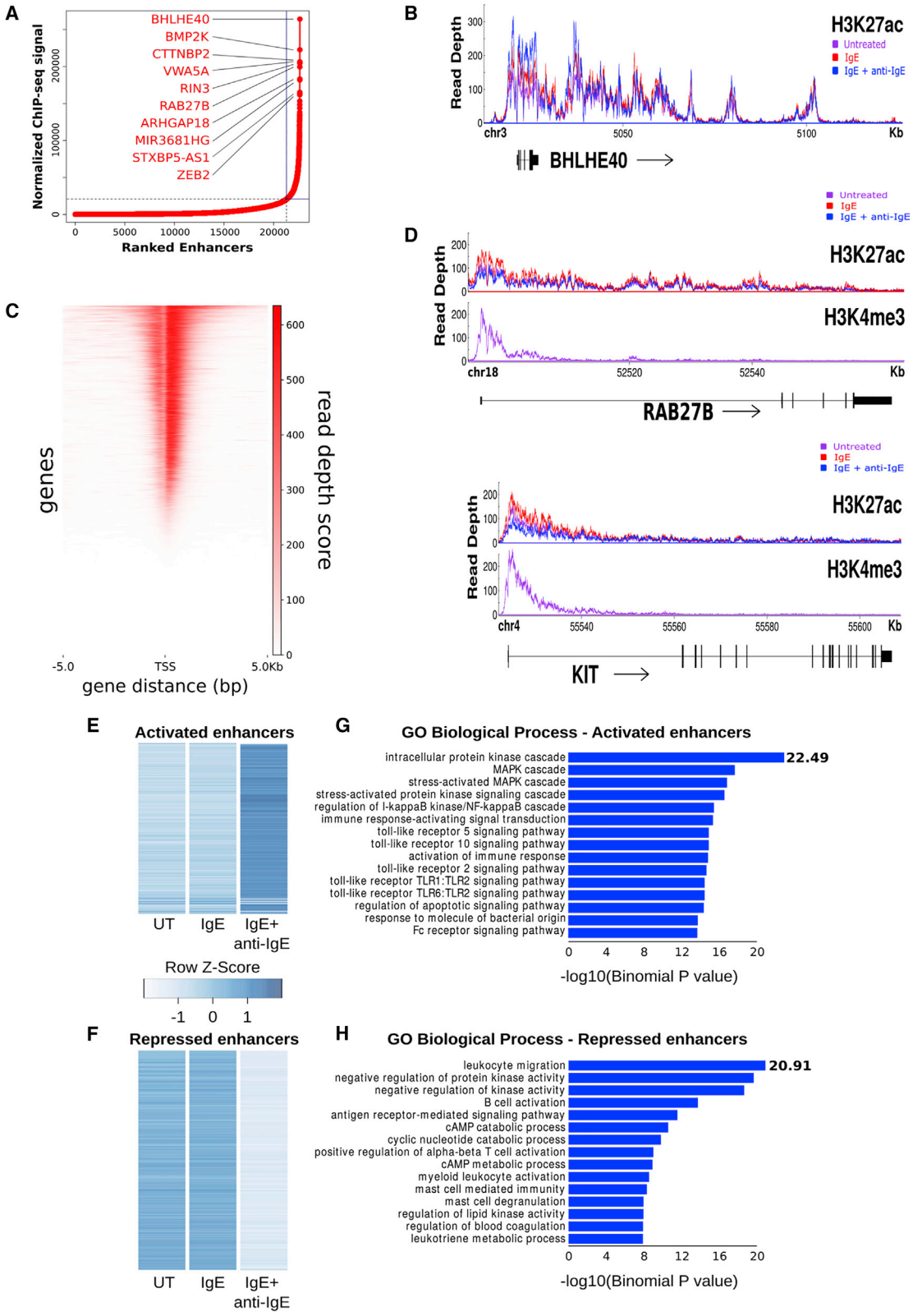


Figure 1. Epigenomic Profiling of Human Peripheral-Blood-Derived MCs

(A) ROSE was used to identify top enhancers based on normalized H3K27ac ChIP-seq signals. Genes harboring top-10 enhancer regions were indicated. Data are from two independent biological replicates.

(legend continued on next page)

machinery (Shlyueva et al., 2014). Chromatin immunoprecipitation sequencing (ChIP-seq) analysis of histone acetyltransferase p300 or different combinations of histone marks, such as H3K4me1, H3K4me2, and H3K27Ac or DNase I hypersensitivity assays, can be used to identify various classes of enhancers (Calo and Wysocka, 2013). The activation of enhancers is cell-type and stimulus specific, and alterations in enhancer activation are associated with disease progression in various settings (Rickels and Shilatifard, 2018). Therefore, characterization of cell-type-specific epigenome, including enhancers and other *cis*-regulatory elements, is an active area of investigation (Davis et al., 2017; Kundaje et al., 2015; Stunnenberg et al., 2016). Similar to enhancers, broad H3K4me3 domains, extending from a TSS to a gene body to achieve transcriptional consistency, are also linked to the cell-type identity and cell-type-enriched functions (Benayoun et al., 2014). In line with this, broad H3K4me3 domains play important roles in developmental programs and disease progression (Chen et al., 2015; Dahl et al., 2016; Dhar et al., 2018).

Chromatin profiling is a powerful tool in identifying the molecular drivers of disease and studying the roles of disease-associated variants in the immune system. Given the critical roles of MCs in allergic and inflammatory diseases, profiling the human MC chromatin landscape holds potential in gaining crucial insights into the roles of these cells in health and disease. Here, we examined the chromatin landscape of resting and activated human MCs from peripheral blood and defined enhancer regions and broad H3K4me3 domains. Changes in intracellular calcium levels upon crosslinking of FcεRI, unlike activation of IL-33 receptor ST2 (IL1RL1), were central to the genome-wide reorganization of the enhancer landscape. Chromatin accessibility analyses defined Ca^{2+}-dependent open chromatin (COC) domains induced upon FcεRI crosslinking in human MCs. These genome-wide changes were also observed in tonsillar MCs isolated from patients with tonsilitis. Using these epigenomic and transcriptomic analyses, we further identified FGL2 as a human-MC-derived soluble mediator and showed that expression of FGL2 is increased in urticaria skin samples. We mapped disease-associated single-nucleotide polymorphisms (SNPs) from 30 inflammatory and autoimmune diseases to regulatory regions in human MCs. These comprehensive epigenomic analyses provide a resource for the identification of regulators of human MC functions and for the further understanding of the impact of MCs in disease.

RESULTS

Characterization of the Enhancer and Broad H3K4me3 Domain Repertoire of Human MCs

To interrogate the enhancer repertoire of human MCs, we first used peripheral-blood-derived MCs, performed H3K27ac ChIP-seq, and ranked enhancers with H3K27ac mark as previously described (Whyte et al., 2013). We consistently obtained highly purified MCs (>98%), very similar biological replicates in terms of H3K27ac reads, and high-quality ChIP-seq datasets with negative and positive control regions (Figures S1A–S1E; Table S1). Using Rank Ordering of Super Enhancers (ROSE), we identified top enhancer regions in human MCs (Figure 1A; Table S1). When genes nearest to these enhancers were further investigated, genes with known functions in MCs, such as RIN3 (Janson et al., 2012), RAB27B (Mizuno et al., 2007), and ZEB2 (Barbu et al., 2012), as well as numerous genes with as-yet-unknown functions in MCs, were identified (Table S1). A snapshot of the top enhancer in BHLHE40 locus, whose function is unknown in human MCs, is shown in Figure 1B, and the other top 4 enhancers are shown in Figure S1F.

To further identify broad H3K4me3 domains of human MCs, we performed H3K4me3 ChIP-seq and ranked genome-wide H3K4me3 signals that were highly enriched in TSS regions (Figure 1C). Typical H3K4me3 signals were around 2 kb, whereas genes with important functions in MCs, such as RAB27B and KIT, showed up to 20 kb H3K4me3 signals (Figure 1D; Table S1). Many genes harboring top enhancer regions were also found to possess broad H3K4me3 domains (Table S1), suggesting cooperation between different chromatin entities to regulate higher-order chromatin structure in human MCs.

FcεRI Crosslinking Governs Specific Enhancer Dynamics in Human MCs

To gain further insights into chromatin reorganization and possible enhancer remodeling in response to FcεRI crosslinking (IgE+anti-IgE treatment), we used H3K27ac as an active enhancer mark (Creyghton et al., 2010). We observed a genome-wide activation and repression of specific chromatin regions upon FcεRI crosslinking, but not upon IgE-sensitization alone (Figure S2; Table S1). We then specifically focused on typical enhancers as previously annotated (Farh et al., 2015) and identifed FcεRI-crosslinking-mediated activated and repressed distal enhancers (Figures 1E and 1F). To further explore these remodeled enhancers, differential H3K27ac

(B) Sushi plot of top enhancer in BHLHE40 gene in untreated, IgE-sensitized, and IgE+anti-IgE-treated conditions. Data are from two independent biological replicates.

(C) Using heatmap analysis, genome-wide H3K4me3 signals were ranked in TSS regions with 5 kb window size. Each red line represents a unique H3K4me3 peak. Data are from two independent biological replicates.

(D) Sushi plot of H3K4me3 and H3K27ac signals in RAB27B and KIT genes in untreated, IgE-sensitized, and IgE+anti-IgE-treated conditions. Data are from two independent biological replicates.

(E) Using H3K27ac ChIP-seq datasets, activated enhancer regions upon IgE+anti-IgE treatment compared to untreated MCs were identified. Each blue line represents a unique activated enhancer region. Data are from two independent biological replicates.

(F) Using H3K27ac ChIP-seq datasets, repressed enhancer regions upon IgE+anti-IgE treatment compared to untreated MCs were identified. Each blue line represents a unique repressed enhancer region. Data are from two independent biological replicates.

(G) Top 15 significantly enriched Gene Ontology (GO) biological process terms for activated enhancers as determined by the Database for Annotation, Visualization, and Integrated Discovery (DAVID) software. Data are from two independent biological replicates.

(H) Top 15 significantly enriched GO biological process terms for repressed enhancers as determined by the DAVID software. Data are from two independent biological replicates.

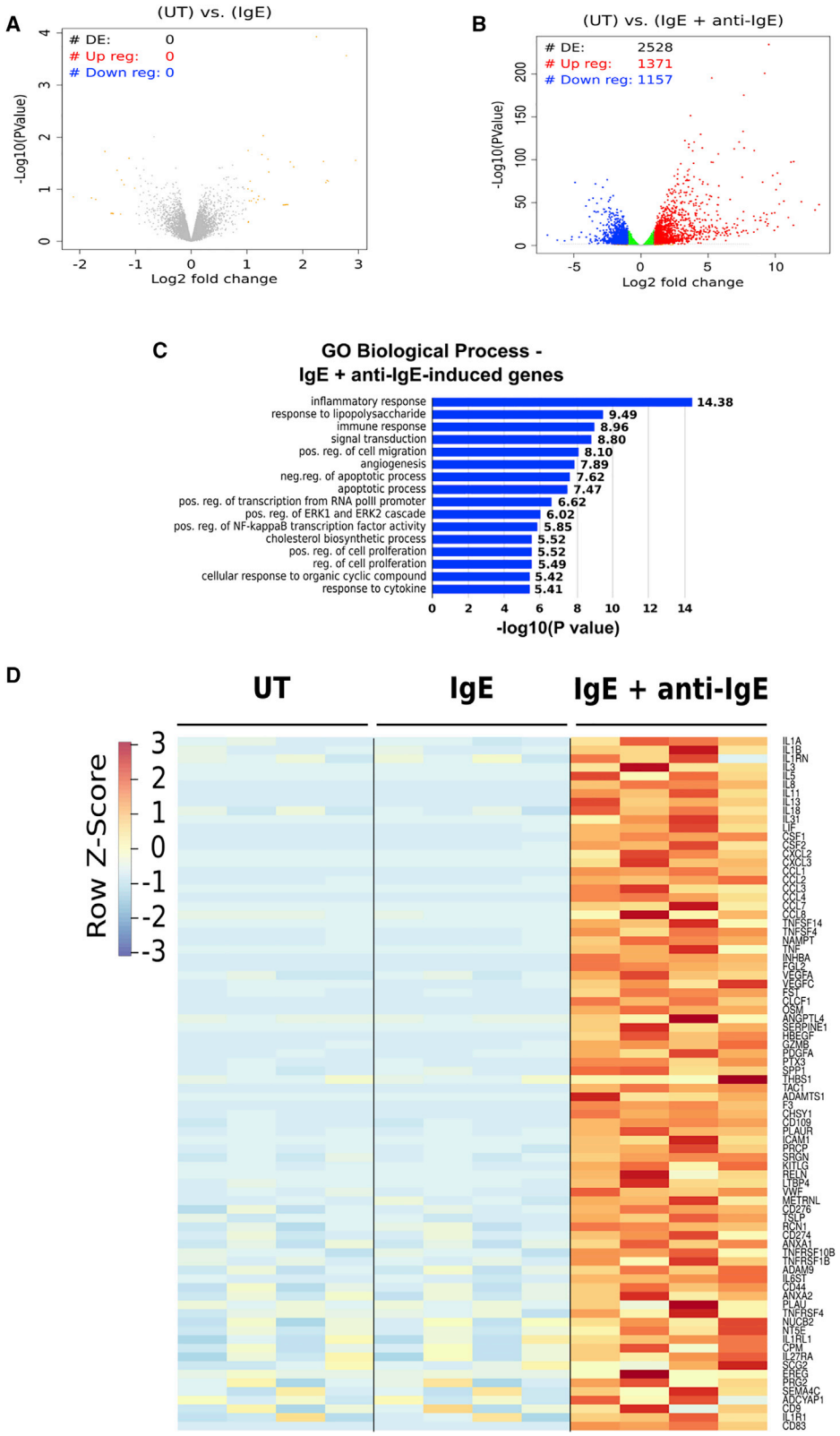


Figure 2. Characterization of Human MC Transcriptome upon FcεRI Crosslinking

(A) Volcano plot showing the differentially expressed genes in IgE-sensitized versus untreated human MCs using paired-end RNA-seq results with four independent biological replicates. Log_2 fold change:1, FDR: 0.05, p = 0.05.

(legend continued on next page)

ChIP-seq peaks were assigned to their nearest genes. Gene Ontology (GO) analysis for the activated enhancers identified significantly enriched biological processes, such as mitogen-activated protein kinase (MAPK) and nuclear factor κB (NF-κB) signaling pathway, regulation of apoptotic signaling pathway, and activation of immune response (Figure 1G). Similarly, repressed enhancers were also associated with distinct GO terms such as negative regulation of protein kinase activity, antigen-receptor-mediated signaling pathway, and MC-mediated immunity (Figure 1H).

Identification of Fibrinogen-like Protein 2 (FGL2) as an MC Mediator

Coupled to the chromatin analysis, we also interrogated the human MC transcriptome with paired-end RNA sequencing (RNA-seq) with 4 independent biological replicates. Similar to H3K27ac ChIP-seq results (Figures S2A and S2C), IgE-sensitization alone did not lead to significant changes in gene expression (Figure 2A). On the other hand, anti-IgE stimulation of IgE-sensitized cells altered the expression of >2,500 RNAs (log_2 fold change: 1; false discovery rate [FDR]: 0.05, p: 0.05) (Figure 2B; Table S2). GO analysis indicated that genes induced upon FcεRI crosslinking were involved in processes such as inflammatory response, apoptotic response, and angiogenesis, among others (Figure 2C). We further validated RNA-seq results by performing RT-qPCR on selected genes such as chemokine (C-C motif), ligand 1 (CCL1), and CCL4, whose expression was highly increased upon FcεRI crosslinking (Figures S3A and S3B).

MCs release a diverse array of soluble mediators via degranulation and conventional exocytosis (Blank et al., 2014). To gain insights into human MC mediators, we limited our RNA-seq analysis only to genes coding for secretory proteins after FcεRI crosslinking. To this end, we first filtered differentially expressed protein-coding transcripts (with mean counts per million [CPM] value >10) using the Human Protein Atlas database (Thul et al., 2017) for "predicted secreted proteins" and cell surface proteins with known extracellular soluble forms. Then, we scoured the published literature to identify bona fide secretory proteins. Using this approach, we identified 80 secretory mediators, including proteins known to be involved in allergic inflammation, such as IL-31, Pentraxin 3 (PTX3), and Oncostatin M (OSM) (Figure 2D). We also identified fibrinogen-like protein 2 (FGL2) and cardiotrophin-like cytokine factor 1 (CLCF1) as candidate soluble mediators produced by human MCs. FGL2 is implicated in several human diseases such as glioma, renal carcinoma, and inflammatory bowel disease (IBD) (Dong et al., 2014; Tang et al., 2017; Yan et al., 2015) and exists in two different forms: membrane-bound and secreted. Regulatory T cells (Tregs) secrete FGL2 (Hu et al., 2016), and FGL2 plays a critical role in some settings, such as in T cell immunoreceptor with Ig and ITIM domains (TIGIT)-induced Treg-mediated suppression of Th1 and Th17, but not in Th2 cell responses (Joller et al., 2014). FGL2 is also associated with cellular damage in cell types such as sinusoidal endothelial cells (Selzner et al., 2012). CLCF1 is a member of the IL-6 family of cytokines involved in cold-induced sweating syndrome (Rousseau et al., 2006).

We confirmed in our H3K27ac ChIP-seq datasets that FGL2 loci were modified upon FcεRI crosslinking (Figure 3A). In line with this, FGL2 mRNA expression was highly increased upon FcεRI crosslinking as determined by RT-qPCR (Figure 3B). To understand whether human MC-derived FGL2 is a secretory mediator, we performed FGL2 enzyme-linked immunosorbent assay (ELISA) in culture supernatants and found that MCs secrete high levels of FGL2 upon FcεRI crosslinking (>3 ng/mL FGL2 per 2 × 10^5 human MCs) (Figure 3C). On the other hand, although CLCF1 loci were also identified to be modified in H3K27ac ChIP-seq datasets (Figure S3C) and CLCF1 mRNA levels were also highly increased upon FcεRI crosslinking (Figure S3D), we could not detect measurable amounts of secreted CLCF1 (<0.1 pg/mL CLCF1/2 × 10^5 human MCs) upon FcεRI crosslinking using two different commercially available ELISA kits (Figure S3E). This highlights the notion that CLCF1 is unable to be efficiently secreted on its own and may require additional factors for secretion (Sims, 2015). As a positive control for the secretory mediators of activated human MCs, we detected IL-4 in the same supernatants (Figure S3F).

To further investigate whether our findings on FGL2 using peripheral-blood-derived human MCs have clinical relevance in the context of allergic diseases where MCs are involved, we focused on chronic spontaneous urticaria (CSU) patients. CSU, also known as itchy hives, is an inflammatory skin condition involving IgE-mediated MC activation (Siebenhaar et al., 2018). After a reported acute allergic reaction in a cohort of CSU patients, biopsy samples from lesional and non-lesional skin were collected and processed to check whether FGL2 could be detected in skin-resident human MCs. To this end, we performed confocal microscopy analysis co-staining for MC tryptase and FGL2. FGL2 foci colocalizing with MCs were significantly increased in lesional CSU skin samples compared to non-lesional samples (Figures 3D–3F) in line with our findings using IgE-activated peripheral-blood-derived human MCs.

Identification of COC Domains upon FcεRI Crosslinking in Human MCs

FcεRI crosslinking triggers the increase of intracellular calcium levels in MCs, which is critical for the fusion of cytoplasmic granules with the plasma membrane upon MC activation (Nishida et al., 2005). Given the epigenomic changes that we observed upon FcεRI crosslinking, we asked whether intracellular calcium levels modulate the chromatin landscape. To investigate the role of intracellular calcium in chromatin reorganization after FcεRI crosslinking, we used BAPTA-AM, a highly selective and cell-

(B) Volcano plot showing the differentially expressed genes in IgE+anti-IgE-treated versus untreated human MCs using paired-end RNA-seq results with four independent biological replicates. Log_2 fold change: 1, FDR: 0.05, p = 0.05.

(C) Top 16 significantly enriched GO biological process terms for the genes with increased expression in IgE+anti-IgE-treated versus untreated human MCs as determined by the DAVID software. Data are from four independent biological replicates.

(D) Heatmap analysis of 80 genes with significantly increased expression (with >10 counts per million [CPM] cutoff values as determined by EdgeR normalization) upon IgE+anti-IgE stimulation and coding for secretory proteins using RNA-seq results with four independent biological replicates. Log_2 fold change: 1, FDR: 0.05, p = 0.05.

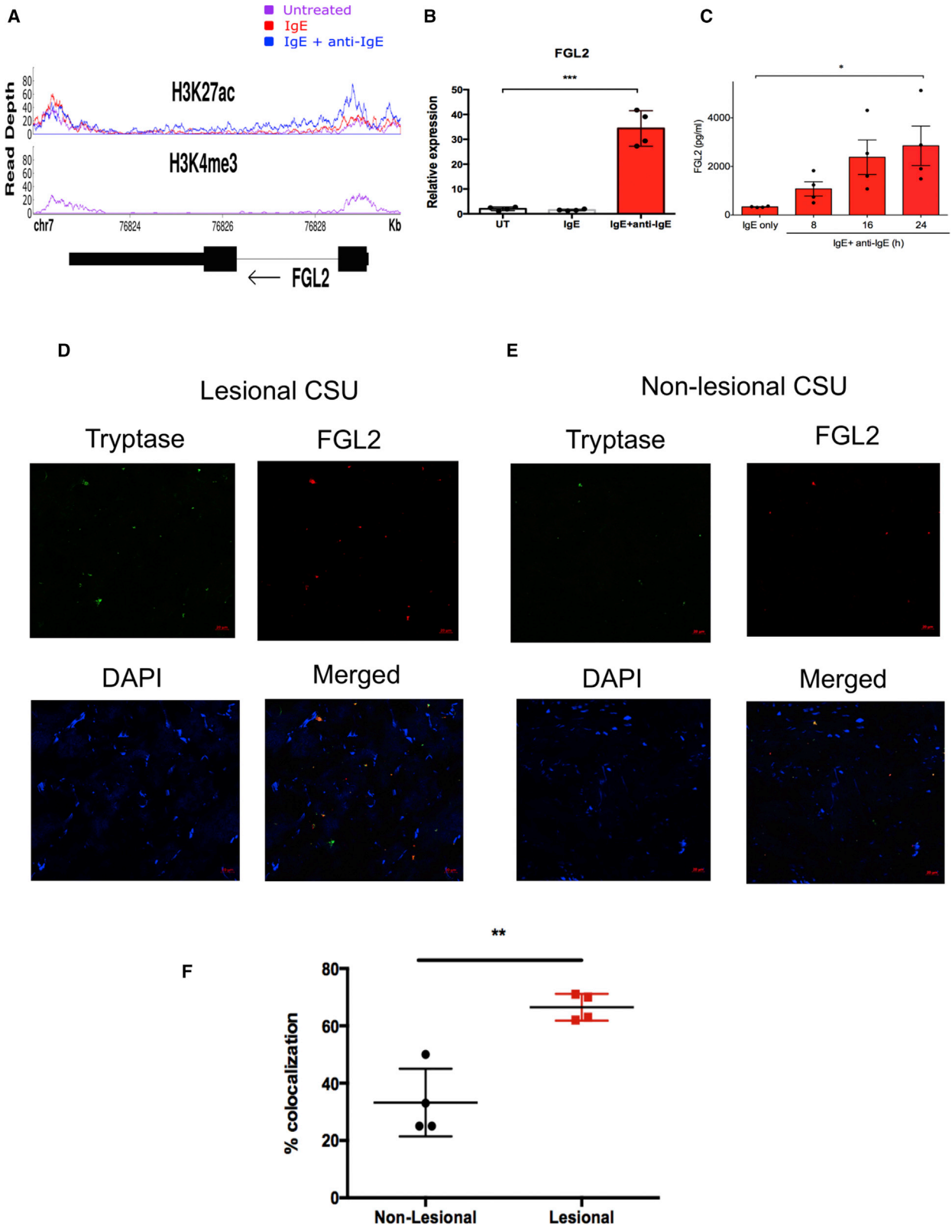


Figure 3. FGL2 is a Human MC-Derived Mediator

(A) Sushi plot of H3K27ac signals of human FGL2 loci in untreated, IgE-sensitized, and IgE+anti-IgE-treated conditions and H3K4me3 signals in untreated condition. Data are from two independent biological replicates.

(legend continued on next page)

permeant calcium chelator. IgE-sensitized human peripheral-blood-derived MCs were pretreated with BAPTA-AM (30 min, 20 μM) or DMSO control before anti-IgE treatment. As expected, BAPTA-AM almost completely blocked anti-IgE-mediated intracellular calcium increase as determined by time-lapse imaging of calcium indicator Fluo-3 AM-loaded human MCs (Figures 4A and 4B). To find out the effects of calcium depletion in chromatin reorganization, we performed Omni-ATAC-seq, an improved version of ATAC-seq that substantially eliminates reads from the mitochondrial genome (Corces et al., 2017). Principal-component analysis (PCA) (Figure 4C) and cluster analysis (Figure 4D) suggested a very high correlation of biological replicates in each treatment condition. Differential Omni-ATAC-seq peak analysis suggested that 2 h treatment with anti-IgE resulted in the opening of chromatin regions in thousands of genomic loci (Figure 4E; Table S3). Moreover, 24 h treatment with anti-IgE led to further reorganization of thousands of new loci, suggesting a dynamic nature of chromatin response (Figure S4, Table S4). A large proportion of Omni-ATAC-seq peaks (92%) was significantly dampened by BAPTA-AM treatment compared to DMSO control (Figure 4F), suggesting an essential role of intracellular calcium for chromatin opening in human MCs. We defined this chromatin signature as Ca^{2+}-dependent COC domains. The majority of Omni-ATAC-seq peaks were located in intronic and intergenic chromatin regions together with promoters (Figure 4G). Similarly, COC domains were also highly enriched in intronic and intergenic regions in human MCs (Figure 4H). TF motif analysis in COC domains indicated binding sites for several TFs such as ATF3, BATF, and AP-1 complex (Figure 5A), all of which are implicated in regulating allergic inflammation (Gilchrist et al., 2010; Lee et al., 2004; Übel et al., 2014). Peak affinities for these binding sites were significantly decreased upon BAPTA-AM treatment (Figure 5B). Thus, the elevation of cytoplasmic calcium levels mediated through endoplasmic reticulum calcium channels and store-operated calcium entry (SOCE) (Suzuki et al., 2012) not only regulates the fusion of granules with the membrane, but also determines a distinct chromatin signature in human MCs.

IL-33 Stimulation Reveals Conserved and Distinct Features of Chromatin Reorganization upon FcεRI Crosslinking

IL-33 is an IL-1 family member nuclear cytokine, and IL-33 receptor (also known as ST2 or IL1RL1) is highly expressed in MCs. Extracellular IL-33 is critically involved in allergic inflammation and has context-dependent functions (Cayrol and Girard, 2018). For instance, IL-33 pre-treatment increases the magnitude of IgE-mediated MC degranulation and chemokine synthesis (Joulia et al., 2017). However, IL-33 treatment alone does not induce calcium mobilization, degranulation, or NFAT pathway activation in MCs, unlike IgE-mediated activation (Andrade et al., 2011; Ball et al., 2018; Joulia et al., 2017). Therefore, the impact of IL-33 on MC chromatin reorganization is also largely unknown. We used Omni-ATAC-seq to investigate IL-33-mediated genome-wide chromatin remodeling and compared this signature with MC activation upon FcεRI crosslinking. IL-33 treatment for 2 h resulted in genome-wide chromatin opening in thousands of genomic locations (Figure 5C; Table S4). TF motif analysis in IL-33-induced Omni-ATAC-seq peaks identified significantly enriched sites for ATF3, BATF, and AP-1 complex (Figure 5D). We then compared these Omni-ATAC-seq peaks with peaks identified upon FcεRI crosslinking and observed both conserved and distinct chromatin regions (Figure 5E; Table S4). When the conserved peaks identified upon both FcεRI crosslinking and IL-33 treatment were compared with COC domains, we observed that 9,805 of 12,071 Omni-ATAC-seq peaks (81.2%) were unique to COC domains (Table S7), suggesting that IL-33 treatment recapitulated the opening of calcium-dependent domains only to a certain extent (Figure 5E). However, the ability of IL-33—which does not increase intracellular calcium levels—to reorganize certain COC domains suggested the existence of chromatin regions in human MCs that were equally responsive to different stimuli. Given the capacity of MCs to recognize a wide range of danger signals, these chromatin regions might provide important clues to the evolutionary adaptations of MC functions.

Peripheral-Blood-Derived Human MCs Recapitulate Unique Features of Human Tissue-Resident MCs

MCs are tissue-resident immune cells that show transcriptomic and phenotypic plasticity depending on the developmental origin and tissue location (Dwyer et al., 2016; Gentek et al., 2018; Li et al., 2018). To investigate whether genomic and transcriptomic signatures observed in human peripheral-blood-derived MCs is relevant to human tissue-resident MCs, we first reanalyzed published cap analysis of gene expression (CAGE) data on human skin-derived MCs (Motakis et al., 2014). Although the comparison is limited by the different methods used for transcriptomics (CAGE versus RNA-seq), we examined the expression of genes harboring top-100 enhancers and broad H3K4me3 domains identified in our datasets. Almost all genes harboring top-100 enhancers (98 of 100) (Figure 6A) and broad H3K4me3 domains (97 of 100) (Figure 6B) were highly expressed in both peripheral-blood-derived and skin-derived human MCs (CPM > 20 in both datasets), suggesting a positive correlation between two different MC types (Table S5). In addition, when genes expressed in common were analyzed (CPM > 1 in both datasets), we still observed a high level of overlap (90%) (Figure 6C; Table S5). To further investigate the utility of our datasets obtained in peripheral-blood-derived human MCs, we next performed Omni-ATAC-seq using human tonsillar MCs isolated with

(B) FGL2 mRNA expression analysis in untreated, IgE-sensitized, and IgE+anti-IgE-treated MCs using RT-qPCR. Results are from four independent biological replicates; $p < 0.001$. Error bars are mean ± SD.

(C) FGL2 ELISA analysis using supernatants of untreated, IgE-sensitized, and IgE+anti-IgE-treated MCs. Results are from four biological replicates; $p < 0.05$. Error bars are mean ± SD.

(D) Representative confocal microscopy images of FGL2 and tryptase foci in lesional CSU skin biopsy samples. Scale bars are 20 microns.

(E) Representative confocal microscopy images of FGL2 and tryptase foci in non-lesional CSU skin biopsy samples. Scale bars are 20 μm.

(F) Quantification of percentage of MCs colocalizing with FGL2 foci in lesional and non-lesional CSU skin biopsies; n = 4 independent patient samples, $p < 0.01$. Error bars are mean ± SD.

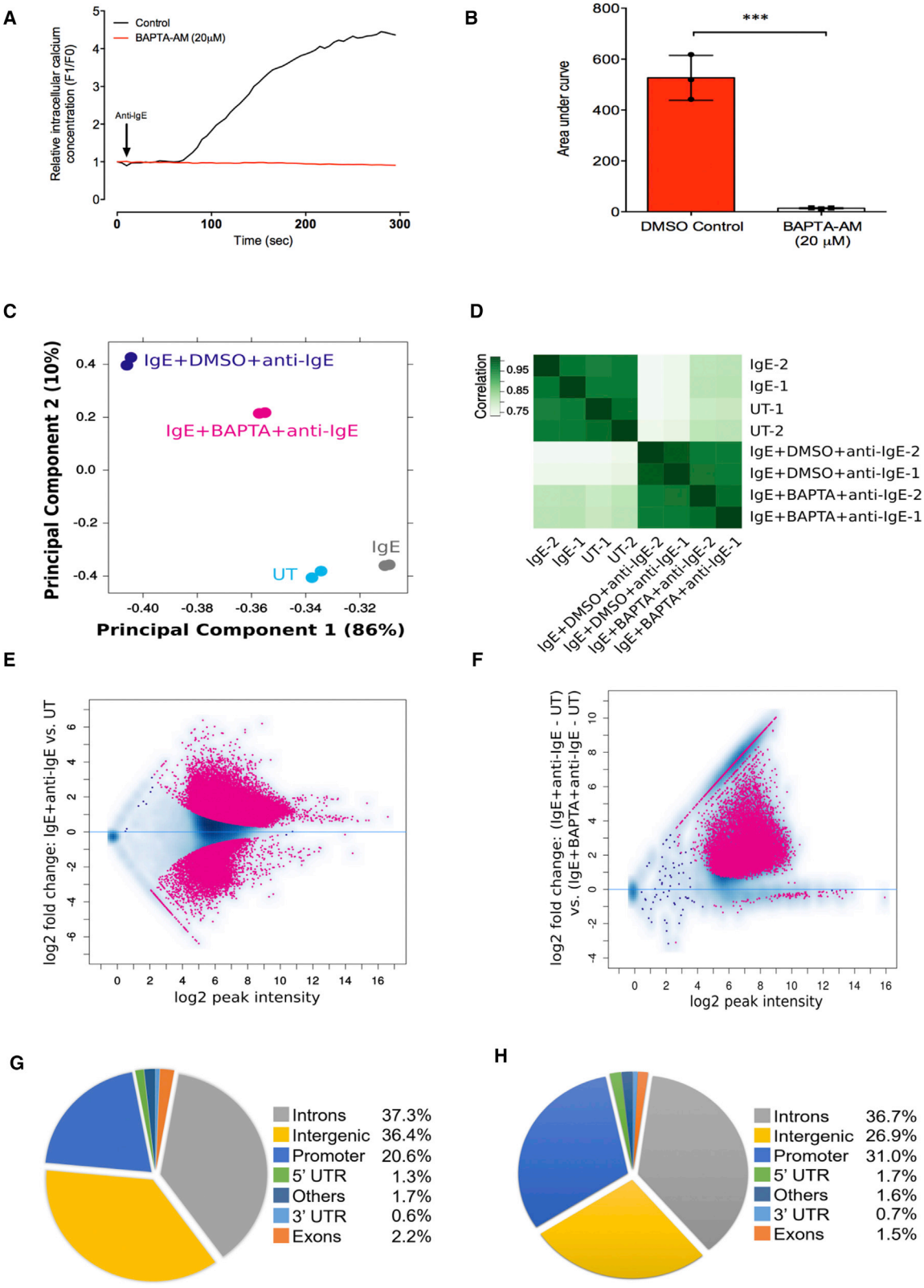


Figure 4. Identification of Ca^{2+}-Dependent Open Chromatin (COC) Domains Induced upon FcεRI Crosslinking

(A) Measurement of intracellular calcium levels using Fluo-3 AM in IgE+DMSO+anti-IgE- versus IgE+BAPTA-AM+anti-IgE-treated MCs. Data are from a representative experiment from three biological replicates.

(legend continued on next page)

CD117 (C-kit) magnetic beads and FcεRI-antibody-mediated sorting (Figures S5A and S5B). Tonsillar MC abundance was highly variable in each donor (Figure S5C). However, we managed to obtain enough MCs from two donors to perform Omni-ATAC-seq. Because the FcεRI antibody clone used for sorting (clone CRA1) also activates human MCs (Motakis et al., 2014), we immediately performed Omni-ATAC-seq on sorted cells. In both biological replicates, we identified Omni-ATAC-seq peaks in histidine decarboxylase (HDC) and tryptase (TPSAB1) gene loci critical for MCs (Figure S5C). We observed a large degree of overlap in Omni-ATAC-seq peaks (95,336 of 113,446) (84%) between IgE+anti-IgE-activated peripheral-blood-derived MCs and isolated tonsillar MCs (Figure 6D). Selected loci in IL1RL1 and SIGLEC6 genes, which are highly expressed in MCs (Figures 6E and 6F), and in CXCL8 (IL8) and CSF2 genes, which display increased expression upon MC activation, are shown for comparison (Figures S5D and S5E). We also investigated the genomic regions of top human MC enhancers and genomic regions of FGL2 and CLCF1 and observed largely coherent Omni-ATAC-seq peaks in tonsillar MCs (Figure S6).

Mapping Disease-Associated SNPs onto Human MC Chromatin Regions

There is extensive genetic variation (84.7 million SNPs) in the human genome as determined by the 1,000 Genomes Project (Auton et al., 2015). Thousands of SNPs are causally associated with the disease heterogeneity or disease prognosis (Lee et al., 2013, 2017). SNPs are also crucial in allergic diseases, which are notoriously heterogeneous in the population (Ferreira et al., 2017). However, despite the critical functions of MCs in allergic, inflammatory, and autoimmune diseases, the locations of disease-associated SNPs in human MC chromatin are largely uncharacterized. Therefore, to gain insights into the association of human MC chromatin and disease-associated SNPs, we extracted 2,049 non-human leukocyte antigen (HLA) SNPs with genome-wide significance ($p \leq 5.0 \times 10^{-8}$) from 30 autoimmune, inflammatory, and allergic disease traits using the National Human Genome Research Institute-European Bioinformatics Institute (NHGRI-EBI) catalog of published genome-wide association studies (GWASs) (MacArthur et al., 2017) (Figures 7A and 7B) and overlaid these SNPs on to our Omni-ATAC-seq, H3K27ac ChIP-seq, and H3K4me3 ChIP-seq datasets (Table S6). We next identified SNPs located precisely in Omni-ATAC-seq peaks of tonsillar MCs (Figure 7C). High-dimensional network analysis suggested that genes harboring these disease-associated SNPs located in Omni-ATAC-seq peaks of tonsillar MCs cooperate with each other in several biological processes (Figure S7). For further analysis, we also included flanking regions of these Omni-ATAC-seq peaks (500 bp upstream and 500 bp downstream) due to the fact that peak boundaries may not be well defined or vary among individuals (Finucane et al., 2015). We observed that each disease trait has a different percentage of SNPs located in Omni-ATAC-seq peaks and in flanking regions of these peaks (Figure 7D). For instance, certain diseases such as allergic rhinitis, ulcerative colitis, and IBD have higher percentages of SNPs in open chromatin regions of human tonsillar MCs (Figure 7D), suggesting a more active involvement of these SNPs in regulating MC functions in these diseases. On the other hand, disorders such as stroke or restless leg sydnrome had the lowest percentage of SNPs in the same Omni-ATAC-seq peaks (Figure 7D). Furthermore, we also identified disease-associated SNPs precisely located in COC domains (Table S6), which could provide important clues about intracellular calcium levels and regulation of gene expression in different diseases. Certain SNPs are located in regulatory chromatin regions of both peripheral-blood-derived and tonsillar MCs. For instance, rs17293632 is an intronic variant in SMAD3 gene loci and is associated with many diseases including asthma, IBD, Crohn's disease, and ulcerative colitis (de Lange et al., 2017; Demenais et al., 2018). rs17293632 is located both in H3K27ac ChIP-seq peaks and Omni-ATAC-seq peaks of peripheral-blood-derived and tonsillar MCs (Figure 7E), suggesting an active involvement of rs17293632 to regulate MC functions. It is important to further investigate the role of this and other SNPs located in regulatory regions of human MCs. Overall, it is conceivable that in a disease state, SNPs could be involved in complex alterations in chromatin landscape to fine-tune gene expression (Smemo et al., 2014).

DISCUSSION

MCs are located in close proximity to blood vessels and nerves in many tissues and express a diverse array of receptors to rapidly respond to extracellular cues (Cildir et al., 2017). The current understanding of the roles of MCs in different disease

(B) Area under the curve (AUC) analysis of intracellular calcium levels in (A). Data are from three independent biological replicates; $p < 0.001$. Error bars are mean ± SD.

(C) Principal-component analysis (PCA) of Omni-ATAC-seq peaks using biological replicates in each condition. The closer the replicates, the stronger the similarity between them. Data are from two independent biological replicates.

(D) Clustering and correlation analysis of biological replicates in Omni-ATAC-seq datasets. The stronger chromatin similarity between different conditions is associated with darker green color in chart. Data are from two independent biological replicates.

(E) Differential Omni-ATAC-seq peaks were identified in untreated versus IgE+anti-IgE-treated human MCs using $\log_2$ peak-intensity (x axis) versus $\log_2$ fold-change (y axis) analyses. Unique Omni-ATAC-seq peaks differentially opening upon IgE+anti-IgE treatment were indicated in pink color. Data are from two independent biological replicates.

(F) Differential Omni-ATAC-seq peaks were identified in IgE+DMSO+anti-IgE-treated versus IgE+BAPTA-AM+anti-IgE-treated human MCs using log peak-intensity (x axis) versus log fold-change (y-xis) analyses. Unique Omni-ATAC-seq peaks differentially opening in these two conditions were indicated in pink color. Data are from two independent biological replicates.

(G) Pie chart showing the genomic locations of differential Omni-ATAC-seq peaks in untreated versus IgE+anti-IgE-treated human MCs. Data are from two independent biological replicates.

(H) Pie chart showing the genomic locations of differential Omni-ATAC-seq peaks in IgE+DMSO+anti-IgE-treated versus IgE+BAPTA-AM+anti-IgE-treated human MCs. Data are from two independent biological replicates.

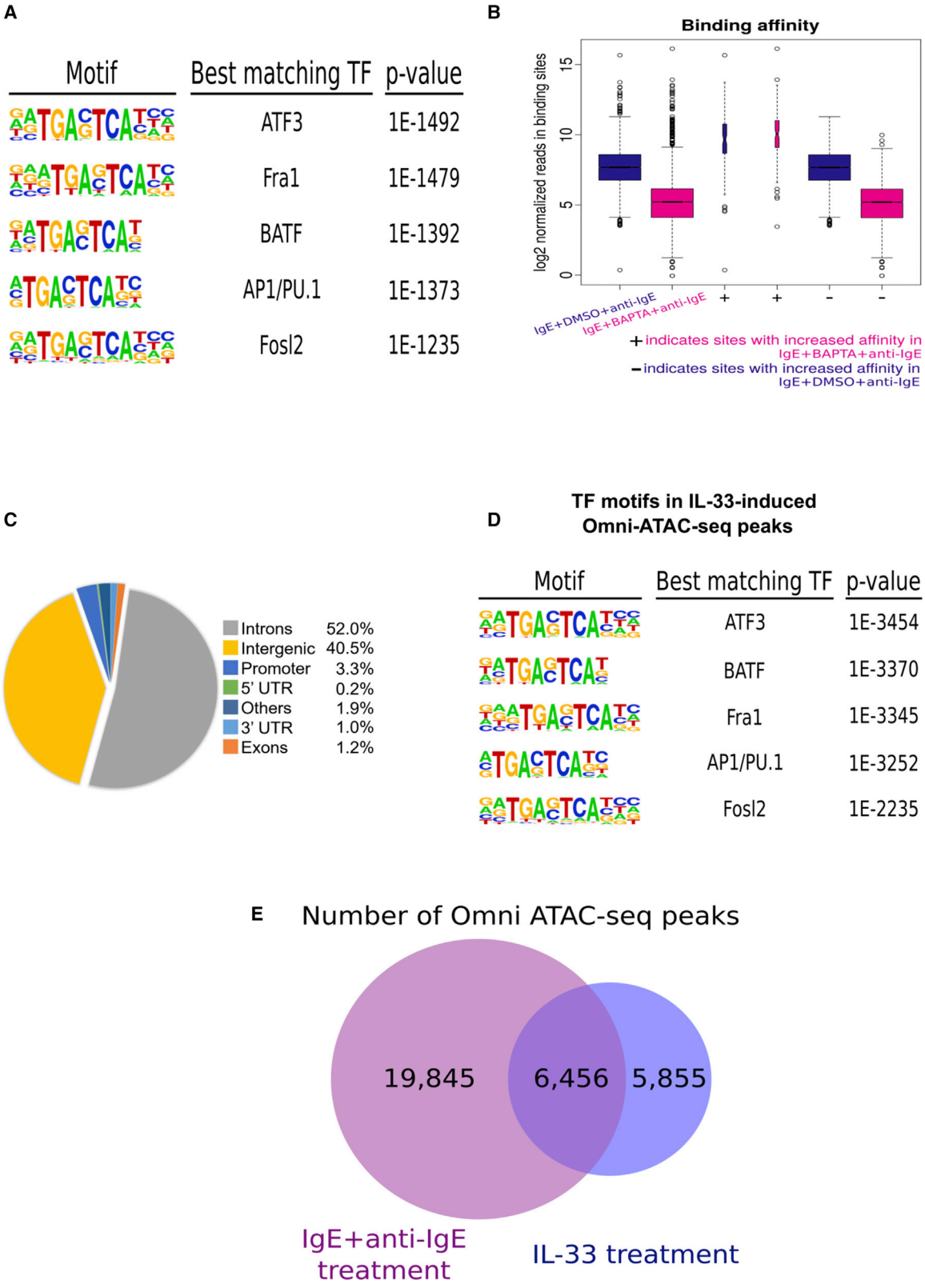


Figure 5. Comparison of the Chromatin Remodeling upon FcεRI Crosslinking and IL-33 Stimulation

(A) TF motif analysis by Hypergeometric Optimization of Motif EnRichment (HOMER) to identify significantly enriched TF motifs in COC domains of human MCs upon FcεRI crosslinking. Data are from two independent biological replicates.

(legend continued on next page)

contexts is largely based on studies in mouse models. The study of human MCs is difficult due to challenges associated with the isolation of sufficient numbers of highly pure and functional MCs from clinical samples. In addition, MC isolation methods based on mechanical tissue dissociation, enzymatic digestion, magnetic cell separation, and sorting impair the functional capacity of MCs (Lorentz et al., 2015). Here, we characterized the chromatin landscape of peripheral-blood-derived primary human MCs, observed genome-wide chromatin remodeling upon FcεRI crosslinking or IL-33 stimulation, and identified broad H3K4me3 domains and enhancers associated with MC activation. Analyses of CAGE data from human skin-derived MCs and Omni-ATAC-seq from *de novo* isolated tonsillar MCs suggest that the genomic changes observed in peripheral-blood-derived MCs upon activation reflect those occurring in tissue-resident MCs. Thus, these datasets present a resource for the identification of regulators of MC function in health and disease. We provide evidence for one such mediator, FGL2. FGL2 secretion was significantly increased upon FcεRI crosslinking in human MCs, and its expression was also increased in lesional skin samples of CSU patients.

Expression profiling of MCs from different mouse tissues provides important insights into the plasticity and diversity of the MC transcriptome (Dwyer et al., 2016). Mouse MCs in different organs share a conserved transcriptional signature, as well as a tissue-specific transcriptional profile likely dictated by the local tissue microenvironment (Dwyer et al., 2016). For instance, mouse MCs from esophagus, tongue, and trachea show a similar transcriptional profile, which is distinct from the peritoneal MCs. Skin and peritoneal MCs are the most distinct subtypes compared with the other constitutive MCs (Dwyer et al., 2016). However, the regulation of tissue-specific transcriptional changes remains elusive. It is also unclear whether different tissue-resident MCs respond differently to the same activating stimuli such as IgE or IL-33. Because data on external stimulation and chromatin reorganization of MCs are not reported in the study by Dwyer et al. (2016), we were unable to compare our results with them. Transcriptional profiling of human skin-derived MCs also provides critical insights into MC activation (Motakis et al., 2014). MCs are distinct from all the other immune cells, and upon expansion in culture and activation with FcεRI crosslinking, human skin-derived MCs show a differential transcriptional response (Motakis et al., 2014). We observed that genes associated with top enhancers and broad H3K4me3 domains in peripheral-blood-derived MCs also have high expression levels in skin-derived MCs. Because data on activation-induced genome-wide chromatin reorganization are not reported in the study by Motakis et al. (2014), we were unable to compare chromatin reorganization between skin-derived human MCs and peripheral-blood-derived MCs. However, our comparison of the chromatin state of peripheral-blood-derived MCs upon FcεRI crosslinking with *de novo* isolated tonsillar MCs showed a high degree of correlation in open chromatin regions. It is likely that the already existing inflammation in tonsils, mechanical dissociation and enzymatic digestion of tonsillar tissue, and isolation of MCs with magnetic beads and FcεRI-based sorting each contributed to an activated state of chromatin in tonsillar MCs.

Immune cells reorganize specific chromatin regions upon different danger signals. Human macrophages, for example, employ a complex interferon (IFN)-γ-mediated enhancer reorganization involving repression, activation, and differential TF binding (Kang et al., 2017). Similarly, stimulation of mouse bone-marrow-derived macrophages with lipopolysaccharide (LPS) leads to remodeling of distinct classes of enhancers (Ostuni et al., 2013). However, involvement of calcium in genome-wide enhancer reorganization in these contexts is unclear. One of the important findings from this study was the regulation of chromatin landscape after FcεRI crosslinking by intracellular calcium levels in human MCs. Intracellular calcium levels are tightly controlled and could be elevated in certain cell types upon stimulation. In T cells, for instance, T cell receptor (TCR) activation triggers a calcium response mediated by store-operated calcium channels, crucial for antigen-dependent T cell proliferation (Vaeth et al., 2017). In MCs, although increased intracellular calcium levels are not critical for microtubule dynamics, they are required for granule exocytosis upon FcεRI crosslinking (Nishida et al., 2005). In addition, calcium is critical for the activation of NFAT and NF-κB pathways (Cildir et al., 2017), but the role of intracellular calcium in genome-wide chromatin reorganization of human MCs is unexplored. Our identification of COC domains suggested that increased levels of calcium are crucial not only for orchestrating the release of the preformed granules, but also for defining the landscape of the chromatin upon FcεRI crosslinking. Notably, we observed that nearly 20% of COC domains are also shared with IL-33 stimulation. Because different extracellular stimuli have secondary biological effects after stimulation, which happens in minutes to hours and could be common for many stimuli, these secondary events are possibly the major contributors to these 20% common regions.

Recent fate-mapping studies in mice suggest that MCs have dual developmental origin (Gentek et al., 2018) and show preferences for different tissue locations depending on their origin (Li et al., 2018). Mucosal MCs (MMCs), such as certain populations of MCs located in the gut, are derived from the fetal HSC-derived cells and are renewed by the bone marrow. In contrast, adult connective-tissue MCs (CTMCs), such as skin-resident MCs, are mainly derived from yolk-sac late-erythro-myeloid progenitors (EMPs) and are self-maintained independently of HSCs (Li et al., 2018). Further studies in the human system are needed to better understand the developmental origin of different tissue-resident human MCs (Grootens et al., 2018).

(B) Peak analysis by HOMER for identified TF binding sites in (A). Data are from two independent biological replicates.
(C) Pie chart showing the genomic locations of Omni-ATAC-seq peaks differentially regulated upon IL-33 treatment. Data are from two independent biological replicates.
(D) TF motif analysis by HOMER to identify significantly enriched TF motifs in Omni-ATAC-seq peaks differentially open upon IL-33 treatment. Data are from two independent biological replicates.
(E) Venn-diagram comparison of Omni-ATAC-seq peaks upon IL-33 stimulaion for 2 h or IgE+anti-IgE stimulation for 2 h (Omni-ATAC-seq peaks in untreated samples were used as background). Data are from two independent biological replicates.

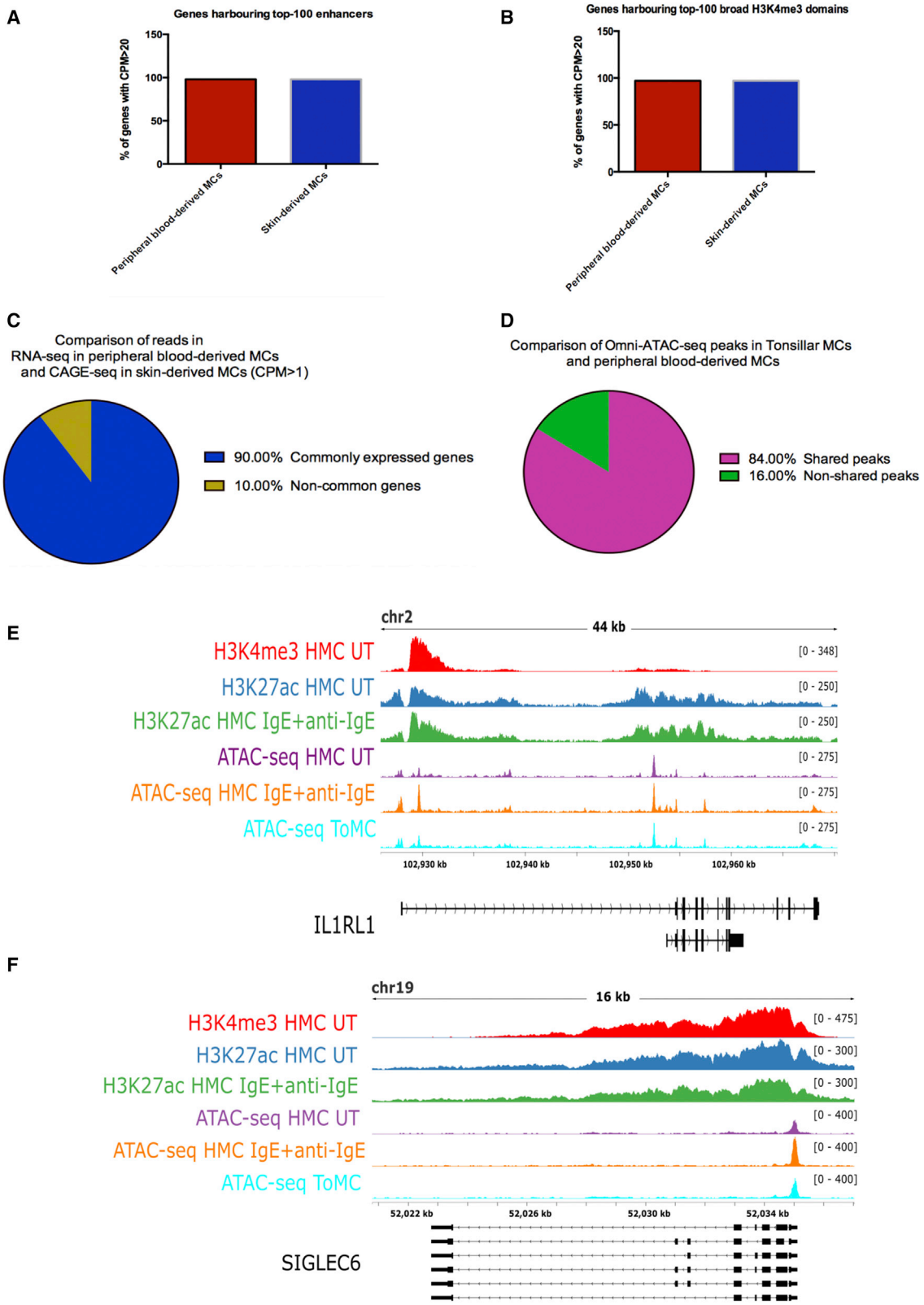


Figure 6. Epigenomic and Transcriptomic Comparison of Peripheral-Blood-Derived Human MCs with Skin-Derived and Tonsillar MCs

(A) Comparison of the expression of genes harboring top-100 enhancers (CPM > 20) in both peripheral-blood-derived and skin-derived MCs (CAGE data were extracted from public databases).

(legend continued on next page)

In our study, we used human MCs derived from the blood progenitors and tonsils to characterize the genome-wide chromatin landscape, and therefore, we note that our findings may be limited to human MCs derived from the bone marrow progenitors. Whether the chromatin response of CTMCs and MMCs to external stimuli could significantly differ remains to be explored.

The relationship between disease-associated variants and regulatory chromatin regions of immune cells is being increasingly appreciated (Farh et al., 2015). GWAS variants are linked to the immune cells where their effects are most pronounced (Schmiedel et al., 2018). Our GWAS analyses of 30 different inflammatory and autoimmune disease traits identified numerous SNPs located in H3K27ac+ chromatin regions and Omni-ATAC-seq peaks in human MCs, suggesting active involvement of these SNPs in regulating epigenome and transcriptome. As expected, a high percentage of SNPs associated with the allergic rhinitis and the trait of ''shared asthma, hay fever, and eczema'' are located in *cis*-regulatory regions of MCs. The roles of MCs in these allergic diseases are well accepted. Our data also suggest the involvement of MCs in other inflammatory and autoimmune diseases (Brown and Hatfield, 2012; Siebenhaar et al., 2018). Further investigation of MCs on disease settings such as Behcet's disease, tuberculosis, ulcerative colitis, and systemic lupus will be required to validate previous reports (Brown and Hatfield, 2012; Garcia-Rodriguez et al., 2017; Hamilton et al., 2014; Lichtig et al., 1981).

Our chromatin-profiling-based approach identified several candidate genes that could be further studied. For instance, we identified the BHLHE40 enhancer region as one of the top candidates in human MCs. BHLHE40 is a repressor of IL-10 production during *Mycobacterium tuberculosis* infection (Huynh et al., 2018) and also regulates cytokine production in T cells in autoimmune diseases (Lin et al., 2014). Therefore, the roles of BHLHE40 in human MCs should be further deciphered in the context of inflammatory diseases. Similarly, further research on genes associated with top enhancers such as BMP2 Inducible Kinase (BMP2K) or Rho GTPase Activating Protein 18 (ARHGAP18) is required. To investigate some of the identified candidate genes, we focused on FGL2. MCs release numerous soluble mediators, including proteases, growth factors, cytokines, and chemokines (Shubin et al., 2017). Our screen identified FGL2, which in its soluble form is mainly linked to Tregs and has suppressor activities against Th1 and Th17 cells, but not against Th2 cells (Joller et al., 2014). Given the well-established role of the Th2-high microenvironment in allergic diseases, it is tempting to speculate that FGL2 plays an important role in the context of allergic diseases.

Overall, chromatin regions reorganized upon activation and associated with disease variants, genes interacting with human MC enhancers, and broad H3K4me3 domains provide crucial links between MC biology and common diseases. Therefore, our study provides an important framework for understanding the role of chromatin reorganization in human MCs and serves as a useful resource to further explore the roles of MCs in human physiology and disease.

STAR★METHODS

Detailed methods are provided in the online version of this paper and include the following:

- KEY RESOURCES TABLE
- LEAD CONTACT AND MATERIALS AVAILABILITY
- EXPERIMENTAL MODEL AND SUBJECT DETAILS
- METHOD DETAILS
  - Peripheral blood-derived MCs
  - Isolation of tonsillar MCs
  - Flow cytometric analysis
  - ELISA
  - CSU skin biopsy samples and confocal microscopy
  - Calcium mobilization study
  - CHIP and CHIP-seq
  - Omni-ATAC-seq
  - RNA isolation and RNA-seq
  - GWAS analysis
  - Bioinformatics analysis of CHIP-seq data
  - Bioinformatics analysis of Omni-ATAC-seq data
  - Bioinformatics analysis of RNA-seq data
- QUANTIFICATION AND STATISTICAL ANALYSIS
- DATA AND CODE AVAILABILITY

SUPPLEMENTAL INFORMATION

Supplemental Information can be found online at https://doi.org/10.1016/j.immuni.2019.09.021.

ACKNOWLEDGMENTS

We thank Tim Hercus and Frank Stomski for assistance and Zbigniew Adam Opala for the cover art. We gratefully acknowledge funding provided by the Agency for Science, Technology, and Research (A*STAR) of Singapore through Institute of Molecular and Cell Biology (IMCB) core fund NFR-CRP17-2017-02; the National Health and Medical Research Council (NHMRC) of Australia through program grant 105253; and the Premier's Research and Industry Fund grant provided by the South Australian Government Department of State Development.

AUTHOR CONTRIBUTIONS

G.C. performed all ChIP-seq, RNA-seq, Omni-ATAC-seq, and confocal microscopy experiments and wrote the manuscript. J.T. and J.Z. performed all bioinformatics analyses. K.H.Y. generated human peripheral-blood-derived MCs

(B) Comparison of the expression of top-100 broad H3K4me3 domain-harboring genes (CPM > 20) in both peripheral-blood-derived and skin-derived MCs.
(C) Pie chart for the comparison of the overlap of expressed genes (CPM > 1) in both peripheral-blood-derived and skin-derived MCs.
(D) Pie chart for the comparison of the overlap of Omni-ATAC-seq peaks in peripheral-blood-derived and tonsillar MCs. Data are from two independent biological replicates.
(E) Integrative Genomics Viewer (IGV) tracks of H3K4me3 and H3K27ac ChIP-seq, Omni-ATAC-seq datasets from peripheral-blood-derived MCs, and Omni-ATAC-seq datasets from tonsillar MCs in human IL1RL1 gene loci. Data are from two independent biological replicates.
(F) IGV tracks of H3K4me3 and H3K27ac ChIP-seq, Omni-ATAC-seq datasets from peripheral-blood-derived MCs, and Omni-ATAC-seq datasets from tonsillar MCs in human SIGLEC6 gene loci. Data are from two independent biological replicates.

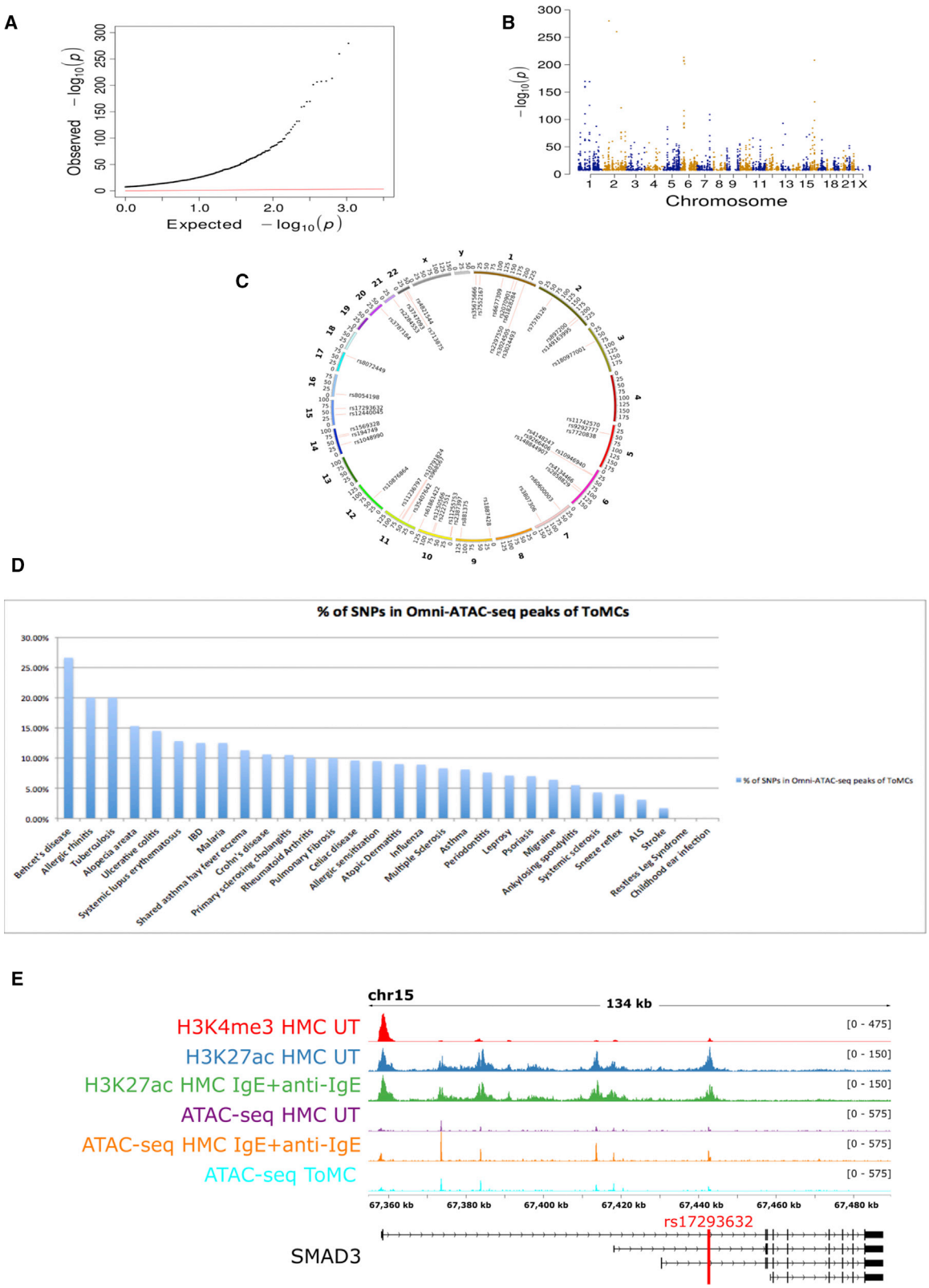


Figure 7. Analysis of Disease-Associated SNPs Located in Regulatory Regions of Human MCs

(A) Q-Q plot analysis of "expected" and "observed" distribution of p values from 2,049 disease-associated non-HLA SNPs with genome-wide significance ($p \leq 5.0 \times 10^{-8}$) extracted from NHGRI-EBI GWAS catalog. The x axis shows expected $-\log_{10}$ (p value) of all SNPs in this study, and the y axis shows the

(legend continued on next page)

for ChIP-seq experiments and performed calcium measurement experiments. M.Z. prepared CSU skin biopsy samples. H.P. provided tonsil samples. P.H. provided CSU skin biopsy samples. N.R., M.A.G., A.F.L., and W.H. provided intellectual input. V.T. supervised the project.

DECLARATION OF INTERESTS

The authors declare no competing interests.

Received: February 28, 2018
Revised: February 18, 2019
Accepted: September 25, 2019
Published: October 22, 2019

REFERENCES

Andrade, M.V., Iwaki, S., Ropert, C., Gazzinelli, R.T., Cunha-Melo, J.R., and Beaven, M.A. (2011). Amplification of cytokine production through synergistic activation of NFAT and AP-1 following stimulation of mast cells with antigen and IL-33. Eur. J. Immunol. *41*, 760–772.

Auton, A., Brooks, L.D., Durbin, R.M., Garrison, E.P., Kang, H.M., Korbel, J.O., Marchini, J.L., McCarthy, S., McVean, G.A., and Abecasis, G.R.; 1000 Genomes Project Consortium (2015). A global reference for human genetic variation. Nature *526*, 68–74.

Ball, D.H., Al-Riyami, L., Harnett, W., and Harnett, M.M. (2018). IL-33/ST2 signalling and crosstalk with FcεRI and TLR4 is targeted by the parasitic worm product, ES-62. Sci. Rep. *8*, 4497.

Barbu, E.A., Zhang, J., Berenstein, E.H., Groves, J.R., Parks, L.M., and Siraganian, R.P. (2012). The transcription factor Zeb2 regulates signaling in mast cells. J. Immunol. *188*, 6278–6286.

Benayoun, B.A., Pollina, E.A., Ucar, D., Mahmoudi, S., Karra, K., Wong, E.D., Devarajan, K., Daugherty, A.C., Kundaje, A.B., Mancini, E., et al. (2014). H3K4me3 breadth is linked to cell identity and transcriptional consistency. Cell *158*, 673–688.

Beyaz, S., Kim, J.H., Pinello, L., Xifaras, M.E., Hu, Y., Huang, J., Kerenyi, M.A., Das, P.P., Barnitz, R.A., Herault, A., et al. (2017). The histone demethylase UTX regulates the lineage-specific epigenetic program of invariant natural killer T cells. Nat. Immunol. *18*, 184–195.

Blank, U., Madera-Salcedo, I.K., Danelli, L., Claver, J., Tiwari, N., Sánchez-Miranda, E., Vázquez-Victorio, G., Ramírez-Valadez, K.A., Macias-Silva, M., and González-Espinosa, C. (2014). Vesicular trafficking and signaling for cytokine and chemokine secretion in mast cells. Front. Immunol. *5*, 453.

Brown, M.A., and Hatfield, J.K. (2012). Mast Cells are Important Modifiers of Autoimmune Disease: With so Much Evidence, Why is There Still Controversy? Front. Immunol. *3*, 147.

Bunting, K.L., Soong, T.D., Singh, R., Jiang, Y., Béguelin, W., Poloway, D.W., Swed, B.L., Hatzi, K., Reisacher, W., Teater, M., et al. (2016). Multi-tiered Reorganization of the Genome during B Cell Affinity Maturation Anchored by a Germinal Center-Specific Locus Control Region. Immunity *45*, 497–512.

Calo, E., and Wysocka, J. (2013). Modification of enhancer chromatin: what, how, and why? Mol. Cell *49*, 825–837.

Cayrol, C., and Girard, J.P. (2018). Interleukin-33 (IL-33): A nuclear cytokine from the IL-1 family. Immunol. Rev. *281*, 154–168.

Chen, K., Chen, Z., Wu, D., Zhang, L., Lin, X., Su, J., Rodriguez, B., Xi, Y., Xia, Z., Chen, X., et al. (2015). Broad H3K4me3 is associated with increased transcription elongation and enhancer activity at tumor-suppressor genes. Nat. Genet. *47*, 1149–1157.

Cildir, G., Pant, H., Lopez, A.F., and Tergaonkar, V. (2017). The transcriptional program, functional heterogeneity, and clinical targeting of mast cells. J. Exp. Med. *214*, 2491–2506.

Corces, M.R., Trevino, A.E., Hamilton, E.G., Greenside, P.G., Sinnott-Armstrong, N.A., Vesuna, S., Satpathy, A.T., Rubin, A.J., Montine, K.S., Wu, B., et al. (2017). An improved ATAC-seq protocol reduces background and enables interrogation of frozen tissues. Nat. Methods *14*, 959–962.

Creyghton, M.P., Cheng, A.W., Welstead, G.G., Kooistra, T., Carey, B.W., Steine, E.J., Hanna, J., Lodato, M.A., Frampton, G.M., Sharp, P.A., et al. (2010). Histone H3K27ac separates active from poised enhancers and predicts developmental state. Proc. Natl. Acad. Sci. USA *107*, 21931–21936.

Dahl, J.A., Jung, I., Aanes, H., Greggains, G.D., Manaf, A., Lerdrup, M., Li, G., Kuan, S., Li, B., Lee, A.Y., et al. (2016). Broad histone H3K4me3 domains in mouse oocytes modulate maternal-to-zygotic transition. Nature *537*, 548–552.

Davis, C.A., Hitz, B.C., Sloan, C.A., Chan, E.T., Davidson, J.M., Gabdank, I., Hilton, J.A., Jain, K., Baymuradov, U.K., Narayanan, A.K., et al. (2017). The Encyclopedia of DNA elements (ENCODE): data portal update (Nucleic Acids Res).

de Kleer, I.M., Kool, M., de Bruijn, M.J., Willart, M., van Moorleghem, J., Schuijs, M.J., Plantinga, M., Beyaert, R., Hams, E., Fallon, P.G., et al. (2016). Perinatal Activation of the Interleukin-33 Pathway Promotes Type 2 Immunity in the Developing Lung. Immunity *45*, 1285–1298.

de Lange, K.M., Moutsianas, L., Lee, J.C., Lamb, C.A., Luo, Y., Kennedy, N.A., Jostins, L., Rice, D.L., Gutierrez-Achury, J., Ji, S.G., et al. (2017). Genome-wide association study implicates immune activation of multiple integrin genes in inflammatory bowel disease. Nat. Genet. *49*, 256–261.

Demenais, F., Margaritte-Jeannin, P., Barnes, K.C., Cookson, W.O.C., Altmüller, J., Ang, W., Barr, R.G., Beaty, T.H., Becker, A.B., Beilby, J., et al.; Australian Asthma Genetics Consortium (AAGC) collaborators (2018). Multiancestry association study identifies new asthma risk loci that colocalize with immune-cell enhancer marks. Nat. Genet. *50*, 42–53.

Dhar, S.S., Zhao, D., Lin, T., Gu, B., Pal, K., Wu, S.J., Alam, H., Lv, J., Yun, K., Gopalakrishnan, V., et al. (2018). MLL4 Is Required to Maintain Broad H3K4me3 Peaks and Super-Enhancers at Tumor Suppressor Genes. Mol. Cell *70*, 825–841.

Dobin, A., Davis, C.A., Schlesinger, F., Drenkow, J., Zaleski, C., Jha, S., Batut, P., Chaisson, M., and Gingeras, T.R. (2013). STAR: ultrafast universal RNA-seq aligner. Bioinformatics *29*, 15–21.

Dong, X., Ye, X., Chen, X., Chen, T., Xie, S., Li, Q., Lin, X., and Huang, Z. (2014). Intestinal and peripheral fibrinogen-like protein 2 expression in inflammatory bowel disease. Dig. Dis. Sci. *59*, 769–777.

Dwyer, D.F., Barrett, N.A., and Austen, K.F.; Immunological Genome Project Consortium (2016). Expression profiling of constitutive mast cells reveals a unique identity within the immune system. Nat. Immunol. *17*, 878–887.

Farh, K.K., Marson, A., Zhu, J., Kleinewietfeld, M., Housley, W.J., Beik, S., Shoresh, N., Whitton, H., Ryan, R.J., Shishkin, A.A., et al. (2015). Genetic and epigenetic fine mapping of causal autoimmune disease variants. Nature *518*, 337–343.

observed $-\log_{10}$ (p value) of all SNPs in this study. Deviation from x = y line (red line) indicates a highly significant genome-wide association for SNPs, and each black point indicates a unique SNP deviating from x = y line.

(B) Manhattan plot showing the chromosomal distribution of all SNPs used in this study. The x axis shows the chromosome numbers, and the y axis shows $-\log_{10}$ (p value) of all SNPs in this study. Each blue and yellow point represents a unique SNP.

(C) CIRCOS plot representation of SNPs with genome-wide significance ($p \leq 5.0 \times 10^{-8}$) located in Omni-ATAC-seq peaks of tonsillar MCs. SNP locations were indicated in each chromosome.

(D) Percentages of disease-associated SNPs with genome-wide significance ($p \leq 5.0 \times 10^{-8}$) located in Omni-ATAC-seq peaks and in flanking regions (±500 bp of Omni-ATAC-seq peaks) of human tonsillar MCs were indicated in 30 different disease traits.

(E) IGV tracks of H3K4me3 and H3K27ac ChIP-seq, Omni-ATAC-seq datasets from peripheral blood-derived MCs, and Omni-ATAC-seq datasets from tonsillar MCs in human SMAD3 genomic loci harboring SNP rs17293632.

Ferreira, M.A., Vonk, J.M., Baurecht, H., Marenholz, I., Tian, C., Hoffman, J.D., Helmer, Q., Tillander, A., Ullemar, V., van Dongen, J., et al.; 23andMe Research Team; AAGC collaborators; BIOS consortium; LifeLines Cohort Study (2017). Shared genetic origin of asthma, hay fever and eczema elucidates allergic disease biology. Nat. Genet. *49*, 1752–1757.

Finucane, H.K., Bulik-Sullivan, B., Gusev, A., Trynka, G., Reshef, Y., Loh, P.R., Anttila, V., Xu, H., Zang, C., Farh, K., et al.; ReproGen Consortium; Schizophrenia Working Group of the Psychiatric Genomics Consortium; RACI Consortium (2015). Partitioning heritability by functional annotation using genome-wide association summary statistics. Nat. Genet. *47*, 1228–1235.

Galli, S.J., and Tsai, M. (2012). IgE and mast cells in allergic disease. Nat. Med. *18*, 693–704.

Garcia-Rodriguez, K.M., Goenka, A., Alonso-Rasgado, M.T., Hernández-Pando, R., and Bulfone-Paus, S. (2017). The Role of Mast Cells in Tuberculosis: Orchestrating Innate Immune Crosstalk? Front. Immunol. *8*, 1290.

Gentek, R., Ghigo, C., Hoeffel, G., Bulle, M.J., Msallam, R., Gautier, G., Launay, P., Chen, J., Ginhoux, F., and Bajénoff, M. (2018). Hemogenic Endothelial Fate Mapping Reveals Dual Developmental Origin of Mast Cells. Immunity *48*, 1160–1171.

Gilchrist, M., Henderson, W.R., Jr., Morotti, A., Johnson, C.D., Nachman, A., Schmitz, F., Smith, K.D., and Aderem, A. (2010). A key role for ATF3 in regulating mast cell survival and mediator release. Blood *115*, 4734–4741.

Grootens, J., Ungerstedt, J.S., Nilsson, G., and Dahlin, J.S. (2018). Deciphering the differentiation trajectory from hematopoietic stem cells to mast cells. Blood Adv. *2*, 2273–2281.

Hamilton, M.J., Frei, S.M., and Stevens, R.L. (2014). The multifaceted mast cell in inflammatory bowel disease. Inflamm. Bowel Dis. *20*, 2364–2378.

Heinz, S., Benner, C., Spann, N., Bertolino, E., Lin, Y.C., Laslo, P., Cheng, J.X., Murre, C., Singh, H., and Glass, C.K. (2010). Simple combinations of lineage-determining transcription factors prime cis-regulatory elements required for macrophage and B cell identities. Mol. Cell *38*, 576–589.

Hu, J., Yan, J., Rao, G., Latha, K., Overwijk, W.W., Heimberger, A.B., and Li, S. (2016). The Duality of Fgl2 - Secreted Immune Checkpoint Regulator Versus Membrane-Associated Procoagulant: Therapeutic Potential and Implications. Int. Rev. Immunol. *35*, 325–339.

Huang da, W., Sherman, B.T., and Lempicki, R.A. (2009). Bioinformatics enrichment tools: paths toward the comprehensive functional analysis of large gene lists. Nucleic Acids Res. *37*, 1–13.

Huynh, J.P., Lin, C.C., Kimmey, J.M., Jarjour, N.N., Schwarzkopf, E.A., Bradstreet, T.R., Shchukina, I., Shpynov, O., Weaver, C.T., Taneja, R., et al. (2018). Bhlhe40 is an essential repressor of IL-10 during *Mycobacterium tuberculosis* infection. J. Exp. Med. *215*, 1823–1838.

Janson, C., Kasahara, N., Prendergast, G.C., and Colicelli, J. (2012). RIN3 is a negative regulator of mast cell responses to SCF. PLoS ONE *7*, e49615.

Johnson, J.L., Georgakilas, G., Petrovic, J., Kurachi, M., Cai, S., Harly, C., Pear, W.S., Bhandoola, A., Wherry, E.J., and Vahedi, G. (2018). Lineage-Determining Transcription Factor TCF-1 Initiates the Epigenetic Identity of T Cells. Immunity *48*, 243–257.

Joller, N., Lozano, E., Burkett, P.R., Patel, B., Xiao, S., Zhu, C., Xia, J., Tan, T.G., Sefik, E., Yajnik, V., et al. (2014). Treg cells expressing the coinhibitory molecule TIGIT selectively inhibit proinflammatory Th1 and Th17 cell responses. Immunity *40*, 569–581.

Joulia, R., L'Faqihi, F.E., Valitutti, S., and Espinosa, E. (2017). IL-33 fine tunes mast cell degranulation and chemokine production at the single-cell level. J. Allergy Clin. Immunol. *140*, 497–509.

Jung, M.Y., Smrž, D., Desai, A., Bandara, G., Ito, T., Iwaki, S., Kang, J.H., Andrade, M.V., Hilderbrand, S.C., Brown, J.M., et al. (2013). IL-33 induces a hyporesponsive phenotype in human and mouse mast cells. J. Immunol. *190*, 531–538.

Kang, K., Park, S.H., Chen, J., Qiao, Y., Giannopoulou, E., Berg, K., Hanidu, A., Li, J., Nabozny, G., Kang, K., et al. (2017). Interferon-γ Represses M2 Gene Expression in Human Macrophages by Disassembling Enhancers Bound by the Transcription Factor MAF. Immunity *47*, 235–250.

Kundaje, A., Meuleman, W., Ernst, J., Bilenky, M., Yen, A., Heravi-Moussavi, A., Kheradpour, P., Zhang, Z., Wang, J., Ziller, M.J., et al.; Roadmap Epigenomics Consortium (2015). Integrative analysis of 111 reference human epigenomes. Nature *518*, 317–330.

Langmead, B., Trapnell, C., Pop, M., and Salzberg, S.L. (2009). Ultrafast and memory-efficient alignment of short DNA sequences to the human genome. Genome Biol. *10*, R25.

Lee, Y.N., Tuckerman, J., Nechushtan, H., Schutz, G., Razin, E., and Angel, P. (2004). c-Fos as a regulator of degranulation and cytokine production in FcepsilonRI-activated mast cells. J. Immunol. *173*, 2571–2577.

Lee, J.C., Espéli, M., Anderson, C.A., Linterman, M.A., Pocock, J.M., Williams, N.J., Roberts, R., Viatte, S., Fu, B., Peshu, N., et al.; UK IBD Genetics Consortium (2013). Human SNP links differential outcomes in inflammatory and infectious disease to a FOXO3-regulated pathway. Cell *155*, 57–69.

Lee, J.C., Biasci, D., Roberts, R., Gearry, R.B., Mansfield, J.C., Ahmad, T., Prescott, N.J., Satsangi, J., Wilson, D.C., Jostins, L., et al.; UK IBD Genetics Consortium (2017). Genome-wide association study identifies distinct genetic contributions to prognosis and susceptibility in Crohn's disease. Nat. Genet. *49*, 262–268.

Li, H., and Durbin, R. (2009). Fast and accurate short read alignment with Burrows-Wheeler transform. Bioinformatics *25*, 1754–1760.

Li, Z., Liu, S., Xu, J., Zhang, X., Han, D., Liu, J., Xia, M., Yi, L., Shen, Q., Xu, S., et al. (2018). Adult Connective Tissue-Resident Mast Cells Originate from Late Erythro-Myeloid Progenitors. Immunity *49*, 640–653.

Lichtig, C., Haim, S., Gilhar, A., Hammel, I., and Ludatscher, R. (1981). Mast cells in Behçet's disease: ultrastructural and histamine content studies. Dermatologica *162*, 167–174.

Lin, C.C., Bradstreet, T.R., Schwarzkopf, E.A., Sim, J., Carrero, J.A., Chou, C., Cook, L.E., Egawa, T., Taneja, R., Murphy, T.L., et al. (2014). Bhlhe40 controls cytokine production by T cells and is essential for pathogenicity in autoimmune neuroinflammation. Nat. Commun. *5*, 3551.

Long, H.K., Prescott, S.L., and Wysocka, J. (2016). Ever-Changing Landscapes: Transcriptional Enhancers in Development and Evolution. Cell *167*, 1170–1187.

Lorentz, A., Sellge, G., and Bischoff, S.C. (2015). Isolation and characterization of human intestinal mast cells. Methods Mol. Biol. *1220*, 163–177.

Lun, A.T., Chen, Y., and Smyth, G.K. (2016). It's DE-licious: A Recipe for Differential Expression Analyses of RNA-seq Experiments Using Quasi-Likelihood Methods in edgeR. Methods Mol. Biol. *1418*, 391–416.

Lyons, J.J., and Milner, J.D. (2018). Primary atopic disorders. J. Exp. Med. *215*, 1009–1022.

MacArthur, J., Bowler, E., Cerezo, M., Gil, L., Hall, P., Hastings, E., Junkins, H., McMahon, A., Milano, A., Morales, J., et al. (2017). The new NHGRI-EBI Catalog of published genome-wide association studies (GWAS Catalog). Nucleic Acids Res. *45* (D1), D896–D901.

McLean, C.Y., Bristor, D., Hiller, M., Clarke, S.L., Schaar, B.T., Lowe, C.B., Wenger, A.M., and Bejerano, G. (2010). GREAT improves functional interpretation of cis-regulatory regions. Nat. Biotechnol. *28*, 495–501.

McNeil, B.D., Pundir, P., Meeker, S., Han, L., Undem, B.J., Kulka, M., and Dong, X. (2015). Identification of a mast-cell-specific receptor crucial for pseudo-allergic drug reactions. Nature *519*, 237–241.

Mizuno, K., Tolmachova, T., Ushakov, D.S., Romao, M., Abrink, M., Ferenczi, M.A., Raposo, G., and Seabra, M.C. (2007). Rab27b regulates mast cell granule dynamics and secretion. Traffic *8*, 883–892.

Motakis, E., Guhl, S., Ishizu, Y., Itoh, M., Kawaji, H., de Hoon, M., Lassmann, T., Carninci, P., Hayashizaki, Y., Zuberbier, T., et al.; FANTOM consortium (2014). Redefinition of the human mast cell transcriptome by deep-CAGE sequencing. Blood *123*, e58–e67.

Nishida, K., Yamasaki, S., Ito, Y., Kabu, K., Hattori, K., Tezuka, T., Nishizumi, H., Kitamura, D., Goitsuka, R., Geha, R.S., et al. (2005). FcepsilonRI-mediated mast cell degranulation requires calcium-independent microtubule-dependent translocation of granules to the plasma membrane. J. Cell Biol. *170*, 115–126.

Ostuni, R., Piccolo, V., Barozzi, I., Polletti, S., Termanini, A., Bonifacio, S., Curina, A., Prosperini, E., Ghisletti, S., and Natoli, G. (2013). Latent enhancers activated by stimulation in differentiated cells. Cell *152*, 157–171.

Platts-Mills, T.A., and Woodfolk, J.A. (2011). Allergens and their role in the allergic immune response. Immunol. Rev. *242*, 51–68.

Ramírez, F., Ryan, D.P., Grüning, B., Bhardwaj, V., Kilpert, F., Richter, A.S., Heyne, S., Dündar, F., and Manke, T. (2016). deepTools2: a next generation web server for deep-sequencing data analysis. Nucleic Acids Res. *44* (W1), W160–W165.

Redegeld, F.A., Yu, Y., Kumari, S., Charles, N., and Blank, U. (2018). Non-IgE mediated mast cell activation. Immunol. Rev. *282*, 87–113.

Rickels, R., and Shilatifard, A. (2018). Enhancer Logic and Mechanics in Development and Disease. Trends Cell Biol. *28*, 608–630.

Robinson, M.D., McCarthy, D.J., and Smyth, G.K. (2010). edgeR: a Bioconductor package for differential expression analysis of digital gene expression data. Bioinformatics *26*, 139–140.

Rousseau, F., Gauchat, J.F., McLeod, J.G., Chevalier, S., Guillet, C., Guilhot, F., Cognet, I., Froger, J., Hahn, A.F., Knappskog, P.M., et al. (2006). Inactivation of cardiotrophin-like cytokine, a second ligand for ciliary neurotrophic factor receptor, leads to cold-induced sweating syndrome in a patient. Proc. Natl. Acad. Sci. USA *103*, 10068–10073.

Schmiedel, B.J., Singh, D., Madrigal, A., Valdovino-Gonzalez, A.G., White, B.M., Zapardiel-Gonzalo, J., Ha, B., Altay, G., Greenbaum, J.A., McVicker, G., et al. (2018). Impact of Genetic Polymorphisms on Human Immune Cell Gene Expression. Cell *175*, 1701–1715.

Selzner, N., Liu, H., Boehnert, M.U., Adeyi, O.A., Shalev, I., Bartczak, A.M., Xue-Zhong, M., Manuel, J., Rotstein, O.D., McGilvray, I.D., et al. (2012). FGL2/fibroleukin mediates hepatic reperfusion injury by induction of sinusoidal endothelial cell and hepatocyte apoptosis in mice. J. Hepatol. *56*, 153–159.

Shlyueva, D., Stampfel, G., and Stark, A. (2014). Transcriptional enhancers: from properties to genome-wide predictions. Nat. Rev. Genet. *15*, 272–286.

Shubin, N.J., Glukhova, V.A., Clauson, M., Truong, P., Abrink, M., Pejler, G., White, N.J., Deutsch, G.H., Reeves, S.R., Vaisar, T., et al. (2017). Proteome analysis of mast cell releasates reveals a role for chymase in the regulation of coagulation factor XIIIA levels via proteolytic degradation. J. Allergy Clin. Immunol. *139*, 323–334.

Siebenhaar, F., Redegeld, F.A., Bischoff, S.C., Gibbs, B.F., and Maurer, M. (2018). Mast Cells as Drivers of Disease and Therapeutic Targets. Trends Immunol. *39*, 151–162.

Sims, N.A. (2015). Cardiotrophin-like cytokine factor 1 (CLCF1) and neuropoietin (NP) signalling and their roles in development, adulthood, cancer and degenerative disorders. Cytokine Growth Factor Rev. *26*, 517–522.

Smemo, S., Tena, J.J., Kim, K.H., Gamazon, E.R., Sakabe, N.J., Gómez-Marín, C., Aneas, I., Credidio, F.L., Sobreira, D.R., Wasserman, N.F., et al. (2014). Obesity-associated variants within FTO form long-range functional connections with IRX3. Nature *507*, 371–375.

St John, A.L., and Abraham, S.N. (2013). Innate immunity and its regulation by mast cells. J. Immunol. *190*, 4458–4463.

Stunnenberg, H.G., and Hirst, M.; International Human Epigenome Consortium (2016). The International Human Epigenome Consortium: A Blueprint for Scientific Collaboration and Discovery. Cell *167*, 1145–1149.

Su, S., Law, C.W., Ah-Cann, C., Asselin-Labat, M.L., Blewitt, M.E., and Ritchie, M.E. (2017). Glimma: interactive graphics for gene expression analysis. Bioinformatics *33*, 2050–2052.

Suzuki, Y., Inoue, T., and Ra, C. (2012). Calcium signaling in mast cells: focusing on L-type calcium channels. Adv. Exp. Med. Biol. *740*, 955–977.

Tang, M., Cao, X., Li, P., Zhang, K., Li, Y., Zheng, Q.Y., Li, G.Q., Chen, J., Xu, G.L., and Zhang, K.Q. (2017). Increased expression of Fibrinogen-Like Protein 2 is associated with poor prognosis in patients with clear cell renal cell carcinoma. Sci. Rep. *7*, 12676.

Thorvaldsdóttir, H., Robinson, J.T., and Mesirov, J.P. (2013). Integrative Genomics Viewer (IGV): high-performance genomics data visualization and exploration. Brief. Bioinform. *14*, 178–192.

Thul, P.J., Åkesson, L., Wiking, M., Mahdessian, D., Geladaki, A., Ait Blal, H., Alm, T., Asplund, A., Björk, L., Breckels, L.M., et al. (2017). A subcellular map of the human proteome. Science *356*.

Tordesillas, L., Berin, M.C., and Sampson, H.A. (2017). Immunology of Food Allergy. Immunity *47*, 32–50.

Übel, C., Sopel, N., Graser, A., Hildner, K., Reinhardt, C., Zimmermann, T., Rieker, R.J., Maier, A., Neurath, M.F., Murphy, K.M., et al. (2014). The activating protein 1 transcription factor basic leucine zipper transcription factor, ATF-like (BATF), regulates lymphocyte- and mast cell-driven immune responses in the setting of allergic asthma. J. Allergy Clin. Immunol. *133*, 198–206.

Vaeth, M., Maus, M., Klein-Hessling, S., Freinkman, E., Yang, J., Eckstein, M., Cameron, S., Turvey, S.E., Serfling, E., Berberich-Siebelt, F., et al. (2017). Store-Operated Ca^{2+} Entry Controls Clonal Expansion of T Cells through Metabolic Reprogramming. Immunity *47*, 664–679.

Whyte, W.A., Orlando, D.A., Hnisz, D., Abraham, B.J., Lin, C.Y., Kagey, M.H., Rahl, P.B., Lee, T.I., and Young, R.A. (2013). Master transcription factors and mediator establish super-enhancers at key cell identity genes. Cell *153*, 307–319.

Yan, J., Kong, L.Y., Hu, J., Gabrusiewicz, K., Dibra, D., Xia, X., Heimberger, A.B., and Li, S. (2015). FGL2 as a Multimodality Regulator of Tumor-Mediated Immune Suppression and Therapeutic Target in Gliomas. J. Natl. Cancer Inst. *107*.

Zhang, Y., Liu, T., Meyer, C.A., Eeckhoute, J., Johnson, D.S., Bernstein, B.E., Nusbaum, C., Myers, R.M., Brown, M., Li, W., and Liu, X.S. (2008). Model-based analysis of ChIP-Seq (MACS). Genome Biol. *9*, R137.

STAR★METHODS

KEY RESOURCES TABLE

REAGENT or RESOURCE	SOURCE	IDENTIFIER
Antibodies		
Human IgE, myeloma	Calbiochem	Cat#401152; RRID: AB_2810964
Goat polyclonal anti-human IgE (ε-chain specific)	Sigma-Aldrich	Cat#I6284; RRID: AB_1079106
Mouse monoclonal anti-human FceRIα-FITC (clone CRA1)	Thermo Fisher Scientific	Cat#11-5899-42; RRID: AB_10732835
Mouse monoclonal anti-human FcεRIα-APC (clone CRA1)	Miltenyi Biotec	Cat#130-095-980; RRID: AB_10828234
Mouse monoclonal anti-human CD117-PE (clone YB5.B8)	Thermo Fisher Scientific	Cat#12-1179-41; RRID: AB_1659667
Mouse monoclonal anti-human CD117-APC (clone A3C6E2)	Miltenyi Biotec	Cat#130-098-207; RRID: AB_2660103
Mouse monoclonal IgG2b-FITC (clone eBMG2b)	Thermo Fisher Scientific	Cat#11-4732-42; RRID: AB_10598648
Mouse monoclonal IgG1-PE (clone P3.6.2.8.1)	Thermo Fisher Scientific	Cat#12-4714-41; RRID: AB_1944424
Mouse monoclonal anti-human tryptase (clone G3)	Millipore	Cat#MAB1222; RRID: AB_2206479
Rabbit monoclonal anti-human tryptase (clone EPR8476)	Abcam	Cat#ab134932; RRID: AB_2811029
Mouse monoclonal anti-human FGL2 (clone 6D9)	Abnova	Cat#H00010875-M01; RRID: AB_565732
Goat polyclonal anti-rabbit IgG Secondary Antibody, Alexa Fluor 488	Thermo Fisher Scientific	Cat#A-11008; RRID: AB_143165
Goat anti-Mouse IgG Secondary Antibody, Alexa Fluor 594	Thermo Fisher Scientific	Cat#R37121; RRID: AB_2556549
Rabbit polyclonal anti-human H3K27ac	Abcam	Cat#ab4729; RRID: AB_2118291
Rabbit polyclonal anti-human H3K4me3	Millipore	Cat#07-473; RRID: AB_1977252
Chemicals, Peptides, and Recombinant Proteins		
Lymphoprep	STEMCELL Technologies	Cat#07801
Insulin-Transferrin-Selenium (ITS-G)	GIBCO	Cat#41400045
2-Mercaptoethanol	GIBCO	Cat#21985023
Bovine Serum Albumin (BSA)	Sigma-Aldrich	Cat#A7979
Liberase	Roche	Cat#05401020001
Collagenase, Type I	GIBCO	Cat#17100017
IC Fixation Buffer	eBioscience	Cat#00-8222-49
Permeabilization Buffer	eBioscience	Cat#00-8333-56
Tissue-Tek O.C.T. Compound	Sakura Finetek	Cat#4583
Trypan Blue	GIBCO	Cat#15250061
ProLong Gold Antifade Mountant with DAPI	Molecular Probes	Cat#P36931
BAPTA, AM, cell permeant chelator	Invitrogen	Cat#B6769
Fluo-3, AM, calcium indicator	Invitrogen	Cat#F1242
May-Grünwald Stain	Sigma-Aldrich	Cat#MG500
Giemsa stain	Sigma-Aldrich	Cat#GS500
Formaldehyde solution	Sigma-Aldrich	Cat#F8775
Glycine	Astral Scientific	Cat#BIOGB0235
Protein A - Sepharose 4B	Invitrogen	Cat#101041
Recombinant human SCF	Shenandoah Biotechnology	Cat#100-04
Recombinant human IL-6	Shenandoah Biotechnology	Cat#100-10
Recombinant human IL-3	Shenandoah Biotechnology	Cat#100-80
Recombinant human IL-33	Peprotech	Cat#200-33

(*Continued on next page*)

Continued

REAGENT or RESOURCE	SOURCE	IDENTIFIER
Critical Commercial Assays		
QuantiTect Reverse Transcription kit	QIAGEN	Cat#205311
SYBR Green Master Mix	Bio-Rad	Cat#1725270
CD34 MicroBead Kit, human	Miltenyi Biotec	Cat#130-046-702
CD117 MicroBead Kit, human	Miltenyi Biotec	Cat#130-091-332
Zenon Alexa Fluor 488 Mouse IgG_1 Labeling Kit	Molecular Probes	Cat#Z25002
Human FGL2 ELISA Kit	BioLegend	Cat#436907
Human CLCF1 ELISA Kit	Lifespan Biosciences	Cat#LS-F26804
CLCF1 ELISA Kit	Aviva Systems Biology	Cat#OKEH04677
Human IL-4 ELISA Kit	BioLegend	Cat#430307
QIAquick PCR Purification Kit	QIAGEN	Cat#28104
NEBNext Ultra DNA Library Prep Kit for Illumina	New England Biolabs	Cat#E7370S
Nextera DNA Library Prep Kit	Illumina	Cat#FC-121-1030
TruSeq Stranded Total RNA Library Prep Kit with Ribo-Zero Gold	Illumina	Cat#RS-122-2301
Deposited Data		
Raw and analyzed data	This paper	GEO: GSE125931
CHIP-seq data	This paper	GEO: GSE125886
RNA-seq data	This paper	GEO: GSE125887
Omni-ATAC-seq data	This paper	GEO: GSE125888
Oligonucleotides		
Primer:18 s rRNA F: GCTTAATTTGACTCAAC ACGGGA	This paper	N/A
Primer:18 s rRNA R: AGCTATCAATCTGTCA ATCCTGTC	This paper	N/A
Primer: FGL2 F: CTTGCCAAGACTGCAAGCTG	This paper	N/A
Primer: FGL2 R: CCAGGCGACCATGAAGTACA	This paper	N/A
Primer: CLCF1 F: GCCTGGCGGATGGGATTATT	This paper	N/A
Primer: CLCF1 R: TGCACAGGCACGCTAACATC	This paper	N/A
Primer: CCL1 F: TCCATCTGCTCCAATGAGGG	This paper	N/A
Primer: CCL1 R: GCTGGTAGTTTCGGGGACAG	This paper	N/A
Primer: CCL4 F: GTCTGTGCTGATCCCAGTGA	This paper	N/A
Primer: CCL4 R: GCGGAGAGGAGTCCTGAGTA	This paper	N/A
Software and Algorithms		
FlowJo v.10.0.8	FlowJo, LLC	RRID: SCR_008520
GraphPad Prism 6	GraphPad Software	RRID: SCR_002798
LDMatrix	NIH	RRID: SCR_017391
DAVID 6.8	LHRI	RRID: SCR_001881
HOMER	N/A	RRID: SCR_010881
DiffBind	Bioconductor	RRID: SCR_012918
FastQC	Babraham Bioinformatics	RRID: SCR_014583
edgeR (version 3.3)	Bioconductor	RRID: SCR_012802; (Robinson et al., 2010)
Integrative Genomics Viewer (IGV)	Broad Institute	RRID: SCR_011793; (Thorvaldsdóttir et al., 2013)
Glimma	Bioconductor	RRID: SCR_017389; (Su et al., 2017)
BWA	N/A	RRID: SCR_010910; (Li and Durbin, 2009)
MACS2 (version 2.1.1)	GitHub	RRID: SCR_013291; (Zhang et al., 2008)
Bowtie 0.12.8	N/A	RRID: SCR_005476; (Langmead et al., 2009)
deepTools	GitHub	RRID: SCR_016366; (Ramírez et al, 2016)

(*Continued on next page*)

Continued

REAGENT or RESOURCE	SOURCE	IDENTIFIER
GREAT (2.02)	N/A	RRID: SCR_005807; (McLean et al., 2010)
GeneMania	Cytoscape	RRID: SCR_005709
GWAS catalog	NHGRI-EBI	RRID: SCR_012745
dbSNP	NIH	RRID: SCR_002338
ROSE	Young Lab	RRID: SCR_017390

LEAD CONTACT AND MATERIALS AVAILABILITY

Further information and requests for resources and reagents should be directed to and will be fulfilled by the Lead Contact, Vinay Tergaonkar (vinayt@imcb.a-star.edu.sg). This study did not generate new unique reagents.

EXPERIMENTAL MODEL AND SUBJECT DETAILS

All human studies have been approved by the Human Research Ethics Committee of Central Adelaide Local Health Network (CALHN). Informed consent was obtained from all subjects. Healthy donors provided blood samples for the isolation of $CD34^+$ cells. Patients with chronic spontaneous urticaria (CSU) provided skin biopsy samples. All donors were between 18-60 years old, and samples from both male and female donors were obtained. Subjects were not involved in previous procedures and they were drug or test naive.

METHOD DETAILS

Peripheral blood-derived MCs

Mature human MCs were generated from human peripheral blood-derived $CD34^+$ progenitor cells collected from healthy volunteers (Royal Adelaide Hospital). Briefly, peripheral blood was diluted with sterile phosphate buffered saline (PBS) at a ratio of 1:1, layered gently over Lymphoprep and after centrifugation (600 *g*, 30 min), the interface containing mononuclear cells was harvested and the remaining red blood cells were disrupted with haemolytic solution (155 mM NH_4Cl, 10 mM $KHCO_3$, 0.1 mM EDTA). $CD34^+$ progenitor cells were enriched by positive immunomagnetic selection using CD34 MicroBeads and an autoMACS Pro Separator (Miltenyi Biotec) according to the manufacturer's instructions. The isolated $CD34^+$ cells were then transferred into 12-well plates at a density of 5×10^6 cells/mL in IMDM medium supplemented with 1% insulin-transferrin selenium, 5×10^{-5} M 2-mercaptoethanol, 1% penicillin-streptomycin, 0.1% bovine serum albumin (BSA), 100 ng/mL recombinant human (rh) SCF, 50 ng/mL rhIL-6 and 5 ng/mL rhIL-3, and placed in a CO_2 incubator at 37°C. The cytokine-supplemented medium was replaced weekly and rhIL-3 was omitted from the medium after the first 3 weeks of culture. From week 6 onward, 10% FBS was added to the medium, and MCs were used at 10^{th} week of culture for all experiments. At that time, the populations contained over 98% MCs as determined by May Grünwald-Giemsa staining and by flow cytometric analysis. Human MCs were divided into 3 conditions for further analysis. Cells were either untreated or sensitized with human myeloma IgE (0.5 μg/mL) overnight. Next day, sensitized cells were washed with PBS and either untreated or treated for 2 h or 24 h with anti-human IgE (1 μg/mL) for FcεRI crosslinking. For IL-33-mediated MC activation, cells were incubated with rhIL-33 (10 ng/mL) (Jung et al., 2013) for 2 h.

Isolation of tonsillar MCs

Palatine tonsils were obtained from donors suffering from tonsilitis and undergoing tonsillectomy surgeries. After tonsillectomy, tissues were kept at 4°C in RPMI medium. Tissue was digested into smaller pieces with scissors and incubated with Liberase or Collagenase-1 in RPMI medium for 1 h at 37°C with intermittent shaking. The lysate was then filtered 3 times with 70 μm cell strainer and single cell suspension was washed with PBS containing 2% FBS and 1 mM EDTA. Red blood cells were lysed with haemolytic solution and the remaining cells were then filtered with 40 μm cell strainer. Afterward, $CD117^+$ cells were isolated using CD117 MicroBead Kit and autoMACS Pro Separator according to manufacturer's instructions. $CD117^+$ cells were then incubated with FcεRI-APC antibody (clone CRA1) for 20 min at RT and sorted with MoFlo Astrios EQ Cell Sorter (Beckman Coulter). Sample collection, cell sorting and Omni-ATAC-seq were performed on the same day. Cell viability after sorting was > 95% as determined by trypan blue staining.

Flow cytometric analysis

Peripheral blood-derived MCs were washed with PBS before incubation with human Fc Receptor blocking solution on ice for 15 min. After Fc blocking, MCs were incubated with anti-FcεRI-FITC and anti-CD117 (c-kit)-PE antibodies or isotype control IgG2b-FITC and IgG1-PE antibody for 30 min on ice. Cells were washed and then analyzed on a Beckman Coulter Gallios. For tonsillar MCs, an aliquot of magnetically isolated $CD117^+$ cells were incubated with anti-FcεRI-APC for 20 min at RT. Cells were fixed with 1% PFA for 15 min on ice, washed and then analyzed in flow cytometry. For determination of MC tryptase expression, cells were fixed in IC fixation buffer

(eBioscience) for 20 min at RT and incubated in permeabilization buffer (eBioscience) containing mouse anti-tryptase antibody or isotype control mouse IgG1 antibody that were pre-conjugated with Alexa Flour® 488 using Zenon® Mouse IgG labeling kit. After 30 min, cells were washed and then analyzed in flow cytometry.

ELISA

Supernatants from peripheral blood-derived human MCs were collected after stimulation with IgE+anti-IgE for 8 h, 16 h and 24 h. Cell debris was removed with centrifugation at 11,000 rpm for 10 min and supernatants were stored at −80°C. Supernatants were then used to measure the levels of soluble FGL2, CLCF1 and IL-4 according to the protocols described in ELISA kits.

CSU skin biopsy samples and confocal microscopy

After an acute allergic reaction, skin biopsies (4 mm punch biopsy) were collected from CSU patients attending a research clinic after taking their informed consent. Skin biopsies were immediately embedded in OCT compound and frozen blocks were stored at −80°C till retrieval for performing the assays. Samples were cut (8 μm sections) in cryostat, mounted on slides at −20°C and incubated at RT for 10 min. Subsequently, samples were fixed with 4% formaldehyde in PBS for 10 min at RT, washed 3 times with PBS and blocked with 10% goat serum for 1 h. Primary antibodies anti-FGL2 (mouse monoclonal, 1:75 dilution) and anti-Tryptase (rabbit monoclonal, 1:150 dilution) were incubated with samples overnight. Next day, samples were washed with PBS 3 times and secondary antibodies (AF488-conjugated goat anti-rabbit and AF594-conjugated goat anti-mouse, 1:200 dilution) were incubated with samples for 1 h at RT and slides were washed with PBS 5 times. Finally, slides were mounted with anti-fade mounting medium with DAPI and images were taken using Zeiss LSM 800 confocal microscope.

Calcium mobilization study

MCs were sensitized with myeloma IgE (1 μg/mL) for 16 h and incubated with BAPTA-AM (20 μM, Thermo Fisher) for 30 min before incubation with Fluo-3 AM (5 μM, Life Technologies) in Tyrodes buffer for 30 min at 37°C. Cells were placed in a 15μ-slide Microscopy Chamber (ibidi GmbH). Fluorometric measurements were commenced when > 95% of the cells had settled to the base of the chamber. 5 min after anti-IgE (1 μg/mL) treatment fluorescence intensity was measured at 5 s intervals by a Carl Zeiss LSM 700 Axio Observer. Changes in intracellular $Ca^{2+}[Ca^{2+}]_i$ were expressed as F1/F0 ratios where F1 and F0 were the fluorescence intensity at a specific time and at the initiation of image recording, respectively.

CHIP and CHIP-seq

For each CHIP assay, cells ($2x10^6$) were crosslinked with 1% formaldehyde for 10 min at RT on a rotating platform and formaldehyde was quenched with 125 mM glycine for 5 min. Fixed cells were washed with cold PBS twice and incubated with 5 mL Triton X-100 lysis buffer (0.25% Triton X-100, 10 mM EDTA, 10 mM Tris-HCl (pH:8.1), 100 mM NaCl and protease inhibitors) for 15 min on ice. Subsequently, for chromatin isolation and sonication, cell pellets were dissolved in SDS lysis buffer (1% SDS, 5 mM EDTA, 50 mM Tris-HCl (pH:8.1) and protease inhibitors) and incubated for 1 h at 4°C. Sonication was performed using Bioruptor (Diagenode) with 30 s on/off settings at high mode with 10 min intervals (totally 30 min). Chromatin size between 200-400 bp was considered as optimal for subsequent steps. For immunoprecipitation, sonicated chromatin was diluted 4 times with dilution buffer (1% Triton X-100, 2 mM EDTA, 20 mM Tris-HCl (pH:8.1), 150 mM NaCl and protease inhibitors) and blocked with pre-treated protein-A agarose beads (Dynabeads, Invitrogen) for 2 h on a rotating platform in cold room. Overnight immunoprecipitation was performed using 2.5 μg CHIP grade H3K27ac and H3K4me3 antibodies on a rotating platform in cold room. Next day, 40 μL pre-treated protein A beads were incubated with lysates for 2 h to capture antibody-antigen complexes. Bead-captured complexes were washed with TSE buffer-1 (0.1% NP-40, 1% Triton X-100, 2 mM EDTA, 20 mM Tris-HCl (pH:8.1), 150 mM NaCl), then with TSE buffer-2 (0.1% SDS, 1% Triton X-100, 2 mM EDTA, 20 mM Tris-HCl (pH:8.1), 500 mM NaCl), with Buffer-3 (0.25 M LiCl, 1% NP-40, 1% deoxycholate, 1 mM EDTA, 10 mM Tris-HCl (pH:8.1) and finally with TE-washing buffer (2 mM EDTA, 10 mM Tris-HCl (pH:8.1). DNA was eluted with freshly-prepared elution buffer (1% SDS, 0.1 M $NaHCO_3$) at RT on a rotating platform for 1 h. Samples were incubated at 65°C for reverse-cross-linking, and DNA was isolated with QIAquick PCR Purification Kit (QIAGEN) and quantified using Qubit fluorometer according to the manufacturer's instructions. 10 ng immunoprecipitated DNA was used to generate CHIP-seq libraries using NEB Next Ultra kit. End repair, adaptor ligation, size selection, PCR amplification and cleanup steps were performed according to the instructions in the kit. DNA libraries were sequenced on the Illumina Nextseq 500 at the Genome Institute of Singapore (GIS).

Omni-ATAC-seq

An improved version of ATAC-seq known as Omni-ATAC-seq was peformed as described before (Corces et al., 2017). Briefly, 50,000 MCs were resuspended in 50 μL ATAC-Resuspension-Buffer (RSB) (10 mM Tris-HCl pH:7.4, 10 mM NaCl, 3 mM $MgCl_2$, 0.1% NP-40, 0.1% Tween-20 and 0.01% Digitonin) and incubated 3 min on ice. Lysate was washed with 1 mL ATAC-RSB (with Tween-20 but without NP-40 and Digitonin) and Nextera DNA Library Prep Kit (Illumina, Cat No: FC-121-1030) was used for transposition reaction. Cell pellet was resuspended in 50 μL transposition mixture (25 μL 2X transposition buffer, 2.5 μL transposase, 16.5 μL PBS, 0.5 μL 1% digitonin, 0.5 μL 10% Tween-20, 5 μL H_2O) and incubated for 30 min at 37°C with 1000 RPM mixing. Cleanup was performed using QIAquick PCR Purification Kit and eluted samples (20 μl) were used for PCR amplification reaction (2.5 μL of 25 μM Primer Ad1, 2.5 μL of 25 μM Primer Ad2, 25 μL of 2X NEBNext Master Mix, 20 μL of transposed sample). Cycling conditions were: 72°C for 5 min, 98°C for 30 s, and 5 cycles of: 98°C for 10 s, 63°C 30 s, 72°C 1 min. Reaction was cleaned up with QIAquick PCR Purification Kit and library

size was determined using Agilent 2100 Bioanalyzer. To remove primer dimers and large fragments, double-sided bead purification was performed using Axygen Magnetic beads. Final library quantity was determined with Qubit® (1.0) Fluorometer (Life Technologies, California, USA). Samples with different barcodes were pooled (4 nM, 20 μl) and sequencing was performed on the Illumina NextSeq 500 using 2x75-bp reads at the Australian Cancer Research Foundation (ACRF) Cancer Genomics Facility.

RNA isolation and RNA-seq

Total RNA was isolated with TRIzol Reagent and RNeasy kit (QIAGEN) and analyzed with a Nanodrop. cDNA was synthesized using QuantiTect Reverse Transcription kit (QIAGEN) and RT-qPCR was performed using SYBR Green Master Mix (Bio-Rad). For RNA sequencing, RNA quality and quantity were further determined with Agilent Bioanalyzer. RNA integrity number (RIN) > 8 were considered to be optimal for RNA-seq preparation. Starting with 1 μg total RNA, Illumina Truseq Low Sample (LS) kit was used for generating RNA-seq libraries. Briefly, Ribosomal RNA (rRNA) depletion, 1st strand cDNA synthesis, 2nd strand cDNA synthesis, 3′ adenylation, adaptor ligation, PCR amplification, library validation and pooling were performed according to the protocols in the kit. 18S rRNA was used as housekeeping gene for normalization in all RT-qPCRs.

GWAS analysis

GWAS data were compiled using GWAS catalog (https://www.ebi.ac.uk/gwas/) using 30 different inflammatory and autoimmune disease traits with at least 5 non-HLA SNPs available with genome-wide significance (p value $\leq 5.0 \times 10^{-8}$). SNPs located in HLA regions were removed from the analysis. SNP genomic locations in Genome Assembly GRCh38.p10 was also confirmed using dbSNP database (https://www.ncbi.nlm.nih.gov/SNP/). In the same disease trait, some SNPs have been identified in multiple studies, and only single study was selected. Also, certain SNPs were implicated in multiple disease traits, and those SNPs were not removed from the analysis. R^2 and D' values of Linkage Disequilibrium (LD), as determined by LDmatrix, were included for SNPs located in Tonsillar MCs (Table S6).

Bioinformatics analysis of CHIP-seq data

Raw reads were analyzed and quality checked using the FastQC program. Reads were mapped to the human references genome (Hg19) from University of California Santa Cruz (UCSC) using Bowtie 0.12.8 (Langmead et al., 2009) with default parameters except –m 1 and –segment-mismatches 2. Only reads mapping uniquely to the genome with at most two mismatches were kept. Enriched regions of the genome were identified with the MACS2 (version 2.1.1) (Zhang et al., 2008) peak caller using default parameters and setting a p value cut-off of 1.00e-5. To limit PCR-induced biases duplicate reads were filtered by MACS. For histone marks, peak-calling mode for broad regions was employed and a p value cut-off of 1.00e-5 was again used. Differential binding analysis was performed using R (version 3.4.3) and the DiffBind package. To identify top enhancers, enhancer ranking was performed by the standard parameters of ROSE algorithm using normalized H3K27ac CHIP-seq reads (Whyte et al., 2013). TSS exclusion zone size (to exclude regions contained within ± distance from TSS to account for promoter biases) was chosen as 2500. Maximum distance between two regions that will be stitched together was chosen as 12.5kb. To identify activated and repressed enhancers upon stimulation, typical enhancer regions were annotated by removing ± 2.5kb region from TSS regions as previously described (Farh et al., 2015). Features in the vicinity of peak loci and enrichment of motifs within peaks were determined and analyzed using Homer (Heinz et al., 2010). Clustering of H3K4me3 peaks over TSS regions was carried out using deepTools2 (Ramírez et al, 2016). Heatmaps were generated using R (version 3.2.3). Integrative Genomics Viewer (IGV) (Thorvaldsdóttir et al, 2013) was used for visualizing all alignments. Gene ontology enrichment of genes nearest to peak loci were performed using GREAT (2.02) (McLean et al., 2010).

Bioinformatics analysis of Omni-ATAC-seq data

Raw reads were adaptor trimmed and filtered for short sequences using cutadapt v1.8.1 setting minimum-length option to 18, error-rate 0.2 and overlap 5. The resulting FASTQ files averaging 52 million reads per sample were analyzed and quality checked using the FastQC program. The filtered reads were mapped against the human reference genome (Hg19) using the BWA alignment algorithm (version 0.7.9a-r786 with default parameters) (Li and Durbin, 2009) returning an average alignment rate of 98.5%. Enriched regions of the genome were identified using the MACS2 peak caller (version 2.1.1) (Zhang et al., 2008) setting default parameters and reporting only peaks with a FDR cut-off (-q) of 0.05. Differential binding analysis was performed using R (version 3.4.3) and the DiffBind package. Enrichment of DNA motifs within differential peaks was assessed using the findMotifsGenome.pl script from the HOMER package (Heinz et al., 2010) with default settings. Alignments were visualized and interrogated using IGV (Thorvaldsdóttir et al, 2013).

Bioinformatics analysis of RNA-seq data

RiboZero-depleted RNA-seq libraries from 4 biological replicates for each treatment were multiplexed and sequenced on the Illumina NextSeq 500 platform (high output mode) using the stranded, paired end protocol with a read length of 75. Raw data, averaging 22.5 million read pairs per sample were analyzed and quality checked using the FastQC program. Reads were mapped against the human reference genome (Hg19) using the STAR spliced alignment algorithm (Dobin et al., 2013) (version 2.5.3a with default parameters and–chimSegmentMin 20,–quantMode GeneCounts) returning an average unique alignment rate of 91%. Differential expression analysis was evaluated from TMM normalized gene counts using R (version 3.2.3) and edgeR (Robinson et al., 2010) (version 3.3) following protocols as described (Lun et al., 2016) Alignments were visualized and interrogated using the Integrative Genomics Viewer v2.3.80 (Thorvaldsdóttir et al, 2013). Graphical representations of differentially expressed genes were generated

using Glimma (Su et al., 2017). Gene ontology enrichment of differentially expressed candidates was performed using DAVID (Huang da et al., 2009).

QUANTIFICATION AND STATISTICAL ANALYSIS

Student's t test was used to compare the gene expression levels in quantitative PCR analyses (with mean+SD). For plots showing more than 2 groups, one-way ANOVA with Dunnett's Multiple Comparison test was used. All statistical analyses were performed with Prism software version 6 (GraphPad Software).

DATA AND CODE AVAILABILITY

The datasets generated during this study are available at the Gene Expression Omnibus (GEO) database (GEO ID: GSE125931).

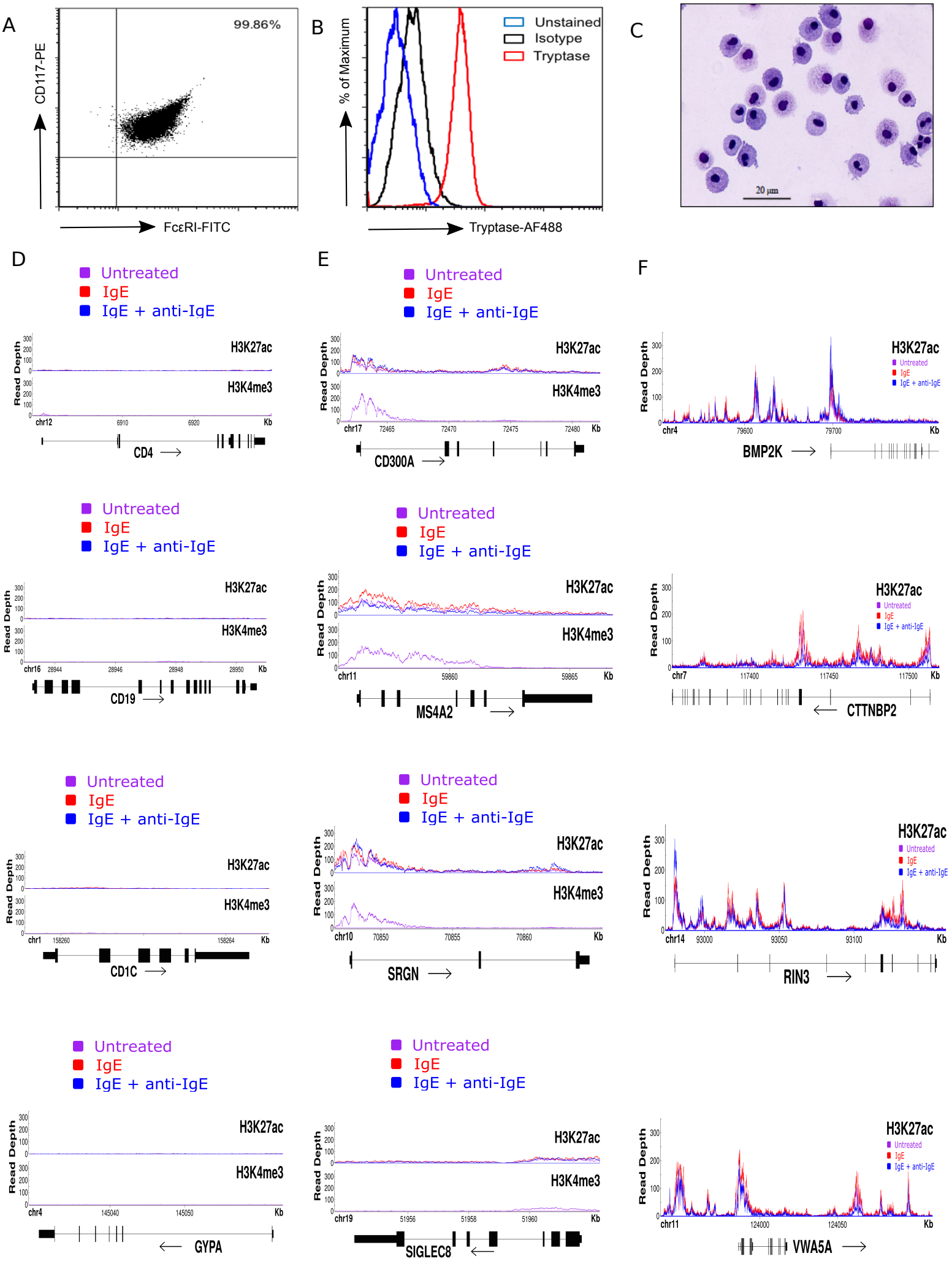
Immunity, Volume *51*

Supplemental Information

Genome-wide Analyses of Chromatin State in Human Mast Cells Reveal Molecular Drivers and Mediators of Allergic and Inflammatory Diseases

Gökhan Cildir, John Toubia, Kwok Ho Yip, Mingyan Zhou, Harshita Pant, Pravin Hissaria, Jingxian Zhang, Wanjin Hong, Nirmal Robinson, Michele A. Grimbaldeston, Angel F. Lopez, and Vinay Tergaonkar

Figure-S1


A
99.86%
CD117-PE
FcεRI-FITC
B
% of Maximum
Unstained
Isotype
Tryptase
Tryptase-AF488
C
20 μm
D
Untreated
IgE
IgE + anti-IgE
H3K27ac
H3K4me3
Read Depth
CD4
CD19
CD1C
E
CD300A
MS4A2
SRGN
F
BMP2K
CTTNBP2
RIN3
GYPA
SIGLEC8
VWA5A

Supplementary Figure-1: Assesment of the purity of peripheral blood-derived MCs and specificity of H3K27ac and H3K4me3 CHIP-seq datasets. Related to Figure-1.

A-C) Human peripheral blood-derived MC purity was assessed by cell surface staining of CD117 (c-kit) and FcεRI, intracellular tryptase staining, and May-Grünwald Giemsa staining. >98% pure MC population was obtained. Data is representative of 4 independent biological replicates. Scale bars are 20 microns.

D) Sushi plots of H3K27ac and H3K4me3 signals in selected chromatin regions in genes not expressed in MCs (CD4, CD19, GYPA, CD1c), showing the specificity of CHIP-seq datasets.

E) Sushi plots of H3K27ac and H3K4me3 signals in selected chromatin regions highly expressed in MCs (CD300A, MS4A2, SRGN, SIGLEC8), showing the specificity of chromatin preparation and CHIP-seq datasets.

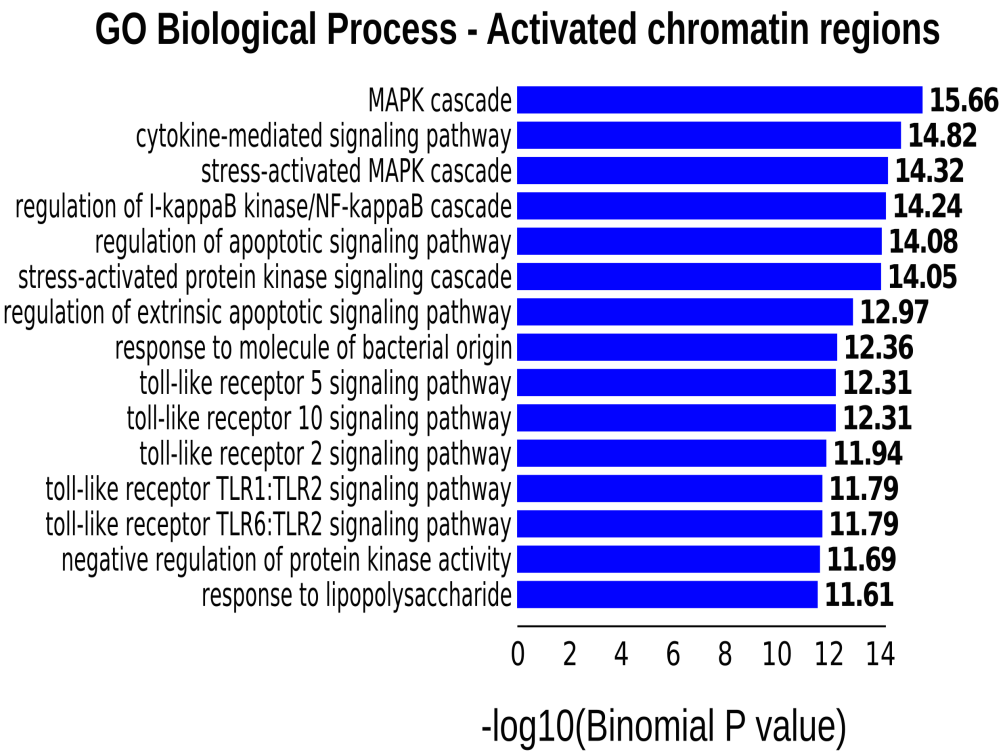
F) Sushi plots of H3K27ac signals in BMP2K, CTTNBP2, RIN3, VWA5A genes harbouring top enhancer regions.

Figure-S2

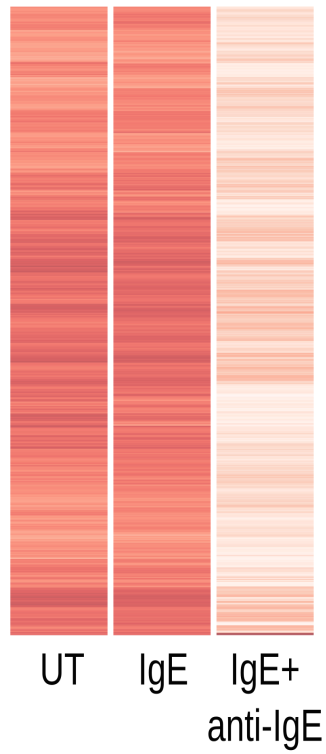
A



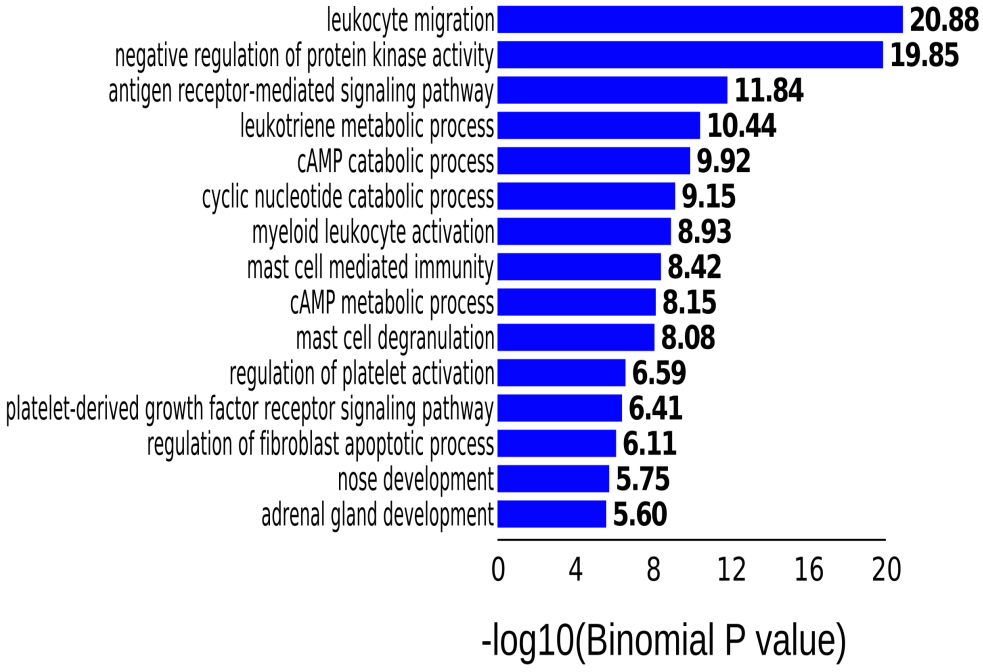
B



C



D



Supplementary Figure-2: Genome-wide remodeling of chromatin regions upon FcεRI crosslinking and GO terms for genes associated with these regions. Related to Figure-1.

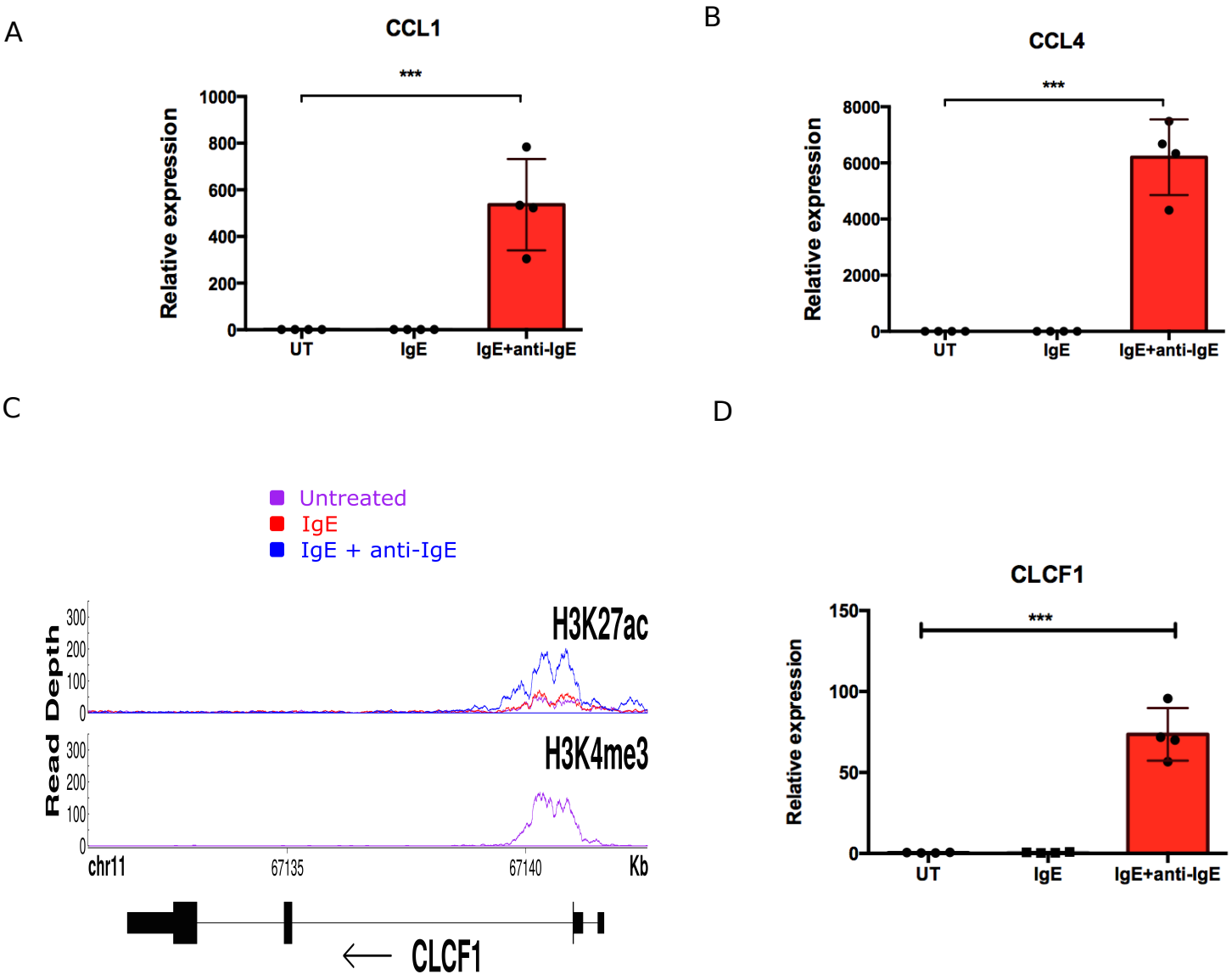
A) Using H3K27ac CHIP-seq datasets, activated chromatin regions were identified upon IgE sensitization alone and upon IgE+anti-IgE treatment compared to untreated MCs. No significant differences were observed upon IgE sensitization alone compared to untreated. Each red line represents a unique activated chromatin region in human MCs. Data are from 2 independent biological replicates.

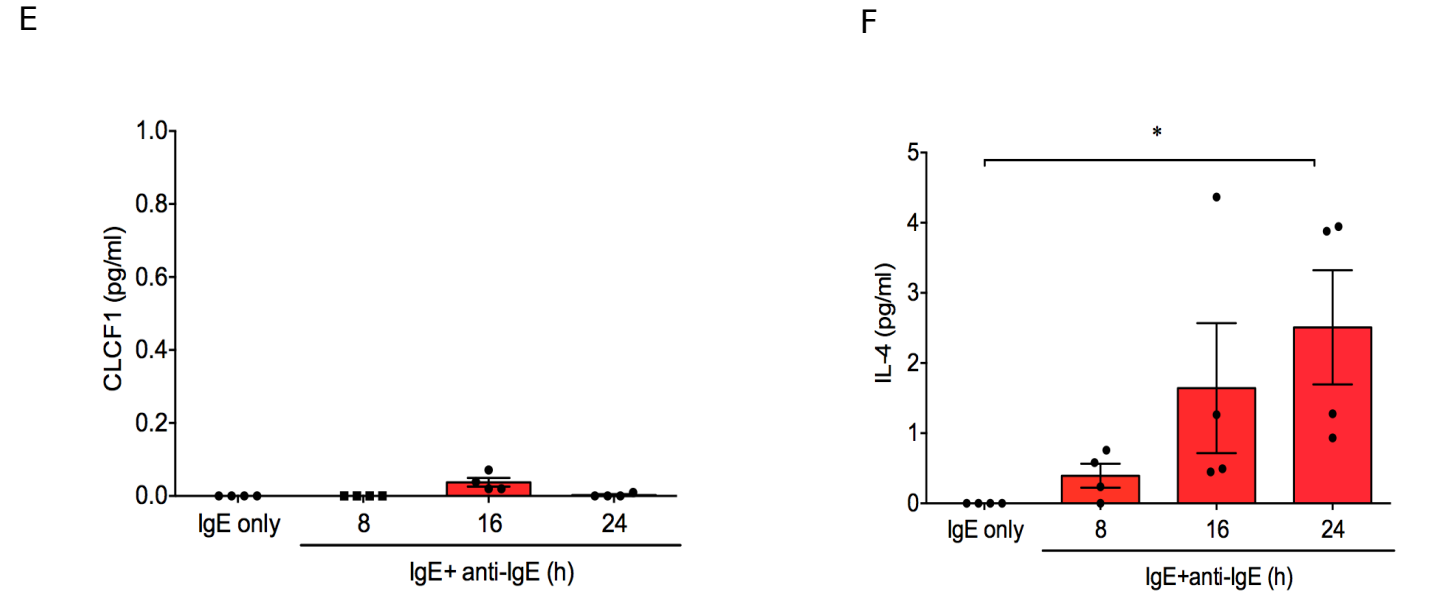
B) Top-15 significantly enriched GO Biological Process terms for genes associated with activated chromatin regions as determined by DAVID. Data are from 2 independent biological replicates.

C) Using H3K27ac CHIP-seq datasets, repressed chromatin regions were identified upon IgE sensitization alone and upon IgE+anti-IgE treatment compared to untreated MCs. No significant differences were observed upon IgE sensitization alone compared to untreated. Each red line represents a unique repressed chromatin region in human MCs. Data are from 2 independent biological replicates.

D) Top-15 significantly enriched GO Biological Process terms for genes associated with repressed chromatin regions as determined by DAVID. Data are from 2 independent biological replicates.

Figure-S3


A
CCL1
***
Relative expression
1000
800
600
400
200
0
UT
IgE
IgE+anti-IgE
B
CCL4
***
Relative expression
8000
6000
4000
2000
0
UT
IgE
IgE+anti-IgE
C
Untreated
IgE
IgE + anti-IgE
Read Depth
H3K27ac
H3K4me3
300
200
100
0
chr11
67135
67140
Kb
CLCF1
D
CLCF1
***
Relative expression
150
100
50
0
UT
IgE
IgE+anti-IgE


E
CLCF1 (pg/ml)
1.0
0.8
0.6
0.4
0.2
0.0
IgE only
8
16
24
IgE+ anti-IgE (h)
F
*
IL-4 (pg/ml)
5
4
3
2
1
0
IgE only
8
16
24
IgE+anti-IgE (h)

Supplementary Figure-3: Analysis of gene expression of CCL1, CCL4 and CLCF1 and secretion of CLCF1 and IL-4. Related to Figure-2.

A) RT-qPCR analysis of CCL1 mRNA levels in untreated, IgE-sensitized and IgE+anti-IgE-treated MCs, n=4 biological replicates, $p<0.001$. Error bars are mean ± SD.

B) RT-qPCR analysis of CCL4 mRNA levels in untreated, IgE-sensitized and IgE+anti-IgE-treated MCs, n=4 biological replicates, $p<0.001$. Error bars are mean ± SD.

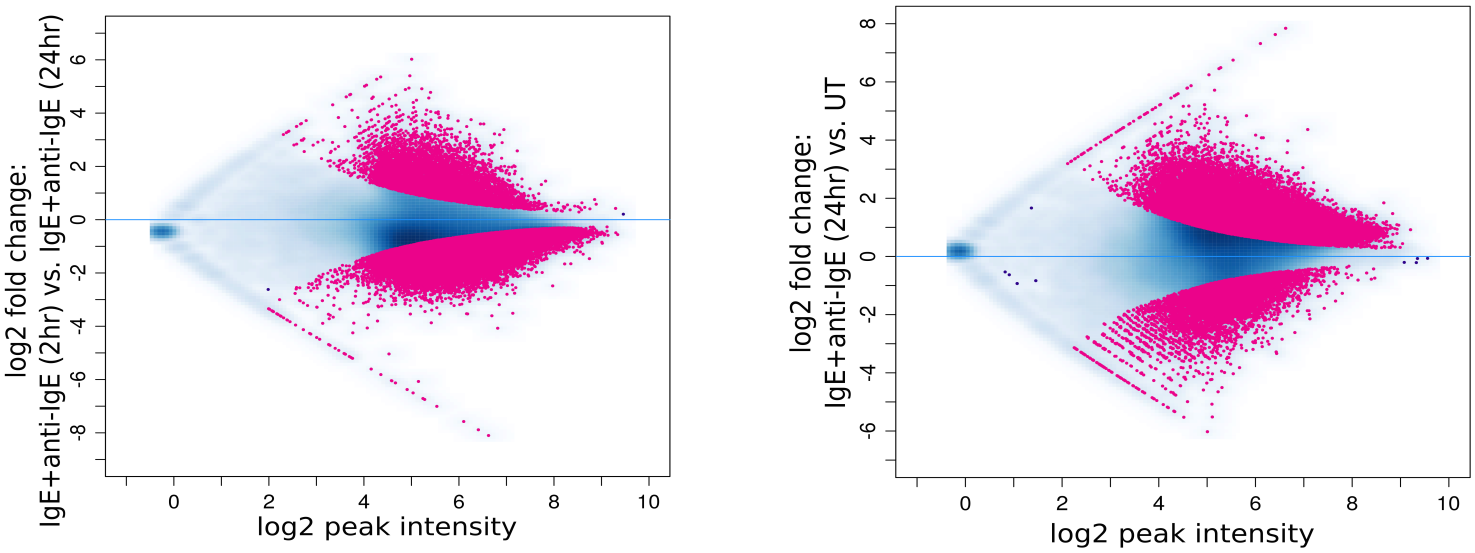
C) IgE+anti-IgE-mediated H3K27ac modifications in CLCF1 locus. H3K4me3 peaks were also indicated in untreated condition.

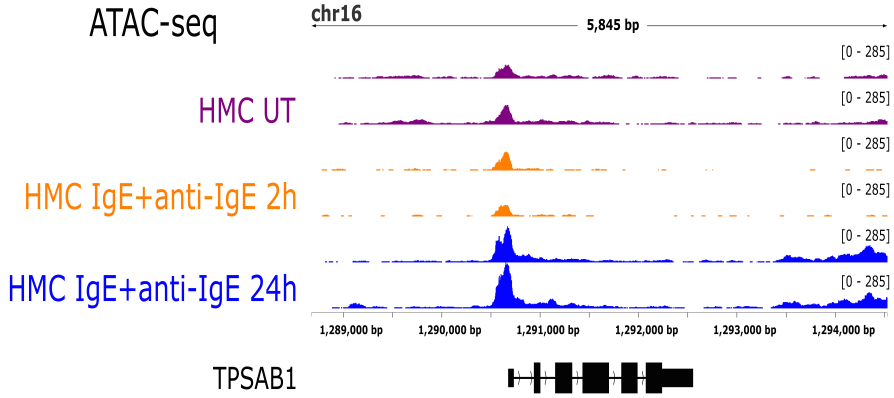
D) RT-qPCR analysis of CLCF1 mRNA levels in untreated, IgE-sensitized and IgE+anti-IgE-treated MCs, n=4 biological replicates, $p<0.001$. Error bars are mean ± SD.

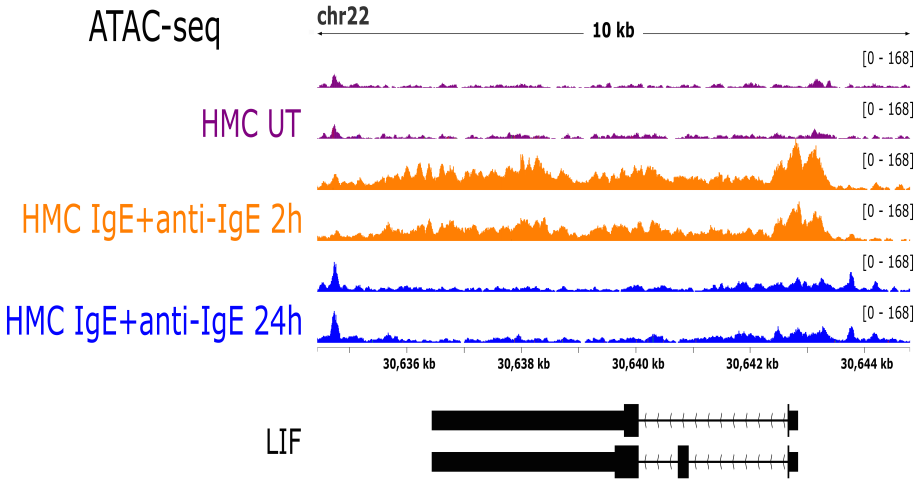
E) CLCF1 ELISA analysis using supernatants of untreated, IgE-sensitized and IgE+anti-IgE-treated MCs in indicated time points. Results are from 4 biological replicates, $p> 0.05$. Error bars are mean ±SD.

F) IL-4 ELISA analysis using supernatants of untreated, IgE-sensitized and IgE+anti-IgE-treated MCs in indicated time points, results are from 4 biological replicates, $p<0.05$. Error bars are mean ±SD.

Figure-S4


log2 fold change:
IgE+anti-IgE (2hr) vs. IgE+anti-IgE (24hr)
log2 peak intensity
log2 fold change:
IgE+anti-IgE (24hr) vs. UT
log2 peak intensity

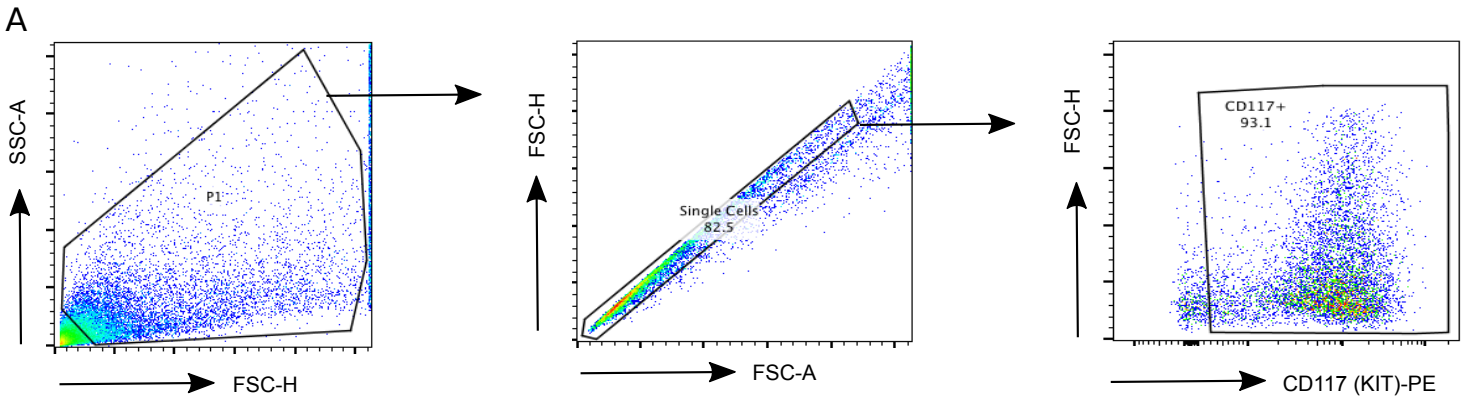

ATAC-seq
chr16
5,845 bp
HMC UT
HMC IgE+anti-IgE 2h
HMC IgE+anti-IgE 24h
[0 - 285]
1,289,000 bp
1,290,000 bp
1,291,000 bp
1,292,000 bp
1,293,000 bp
1,294,000 bp
TPSAB1

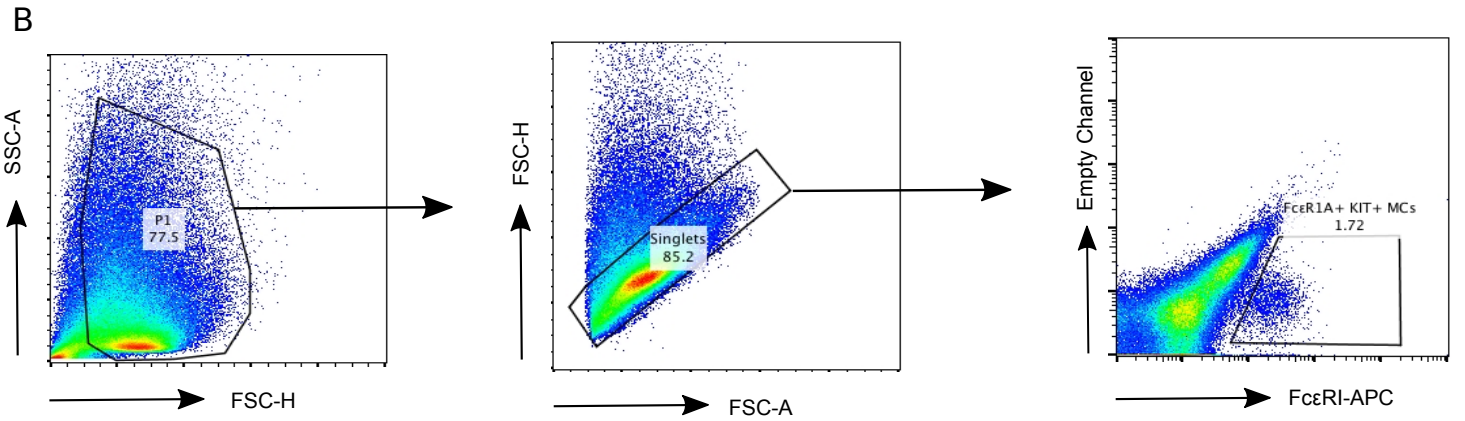

ATAC-seq
chr22
10 kb
HMC UT
HMC IgE+anti-IgE 2h
HMC IgE+anti-IgE 24h
[0 - 168]
30,636 kb
30,638 kb
30,640 kb
30,642 kb
30,644 kb
LIF

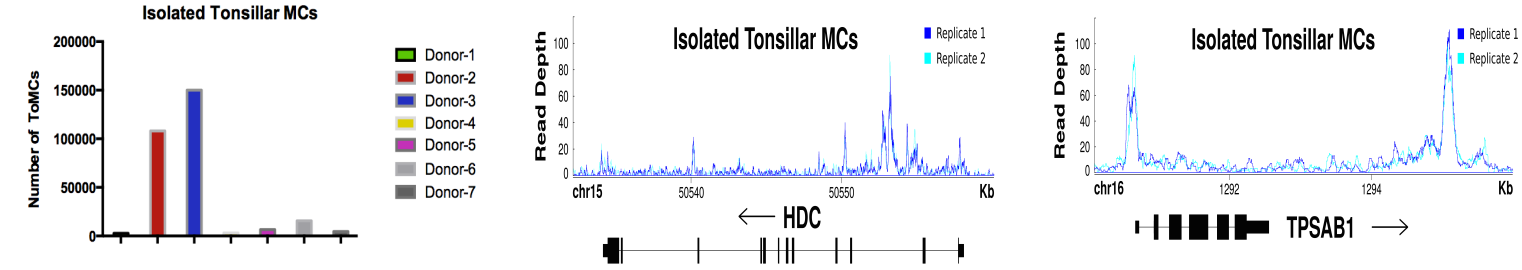
Supplementary Figure-4: Global comparison of Omni-ATAC-seq peaks for UT, 2h anti-IgE and 24h anti-IgE treatment. Related to Figure-4.

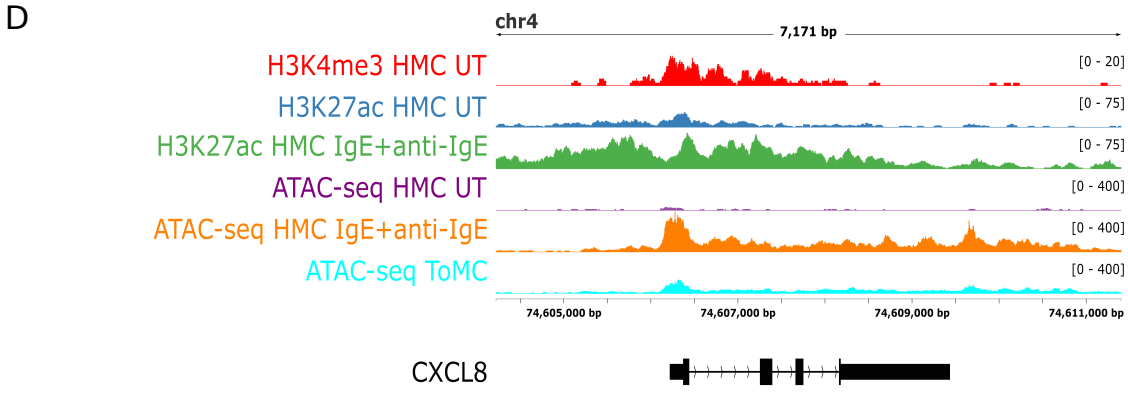
Differential Omni-ATAC-seq peak analysis using UT, 2h anti-IgE treatment and 24h anti-IgE treatment conditions. Omni-ATAC-seq tracks were shown in the loci of TPSAB1 and LIF genes in which dynamic chromatin changes occurred in peripheral blood-derived MCs (HMC).

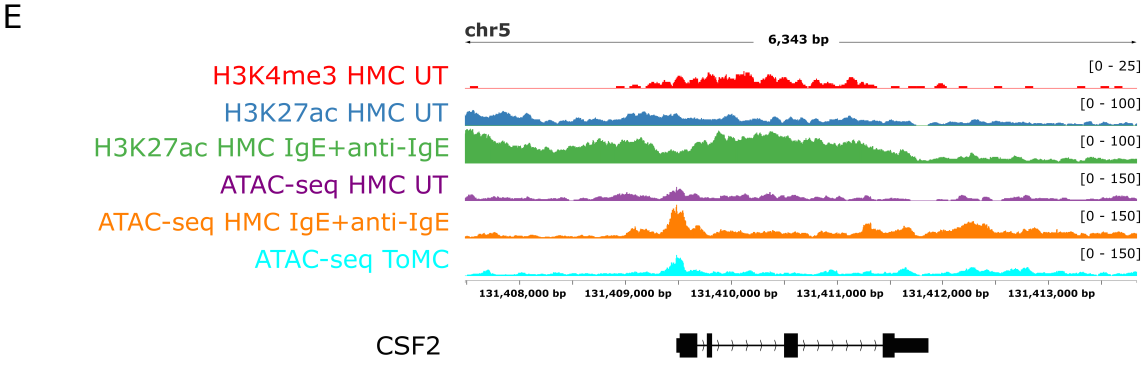
Figure-S5


A
SSC-A
FSC-H
P1
FSC-H
FSC-A
Single Cells
82.5
FSC-H
CD117+
93.1
CD117 (KIT)-PE


B
SSC-A
FSC-H
P1
77.5
FSC-H
FSC-A
Singlets
85.2
Empty Channel
FcεR1A+ KIT+ MCs
1.72
FcεRI-APC


C
Isolated Tonsillar MCs
Number of ToMCs
200000
150000
100000
50000
0
Donor-1
Donor-2
Donor-3
Donor-4
Donor-5
Donor-6
Donor-7
Isolated Tonsillar MCs
Replicate 1
Replicate 2
Read Depth
chr15
50540
50550
Kb
HDC
Isolated Tonsillar MCs
Replicate 1
Replicate 2
Read Depth
chr16
1292
1294
Kb
TPSAB1


D
chr4
7,171 bp
H3K4me3 HMC UT
H3K27ac HMC UT
H3K27ac HMC IgE+anti-IgE
ATAC-seq HMC UT
ATAC-seq HMC IgE+anti-IgE
ATAC-seq ToMC
[0 - 20]
[0 - 75]
[0 - 75]
[0 - 400]
[0 - 400]
[0 - 400]
74,605,000 bp
74,607,000 bp
74,609,000 bp
74,611,000 bp
CXCL8


E
chr5
6,343 bp
H3K4me3 HMC UT
H3K27ac HMC UT
H3K27ac HMC IgE+anti-IgE
ATAC-seq HMC UT
ATAC-seq HMC IgE+anti-IgE
ATAC-seq ToMC
[0 - 25]
[0 - 100]
[0 - 100]
[0 - 150]
[0 - 150]
[0 - 150]
131,408,000 bp
131,409,000 bp
131,410,000 bp
131,411,000 bp
131,412,000 bp
131,413,000 bp
CSF2

Supplementary Figure-5: Isolation of tonsillar MCs and assesment of the specificity of Omni-ATAC-seq peaks from tonsillar MCs. Related to Figure-6.

A) Tonsillar MCs were isolated with a 2-step protocol. Single cells were prepared from tonsillar tissue and $CD117^+$ (c-kit) cells were magnetically isolated with CD117 MicroBead Kit. An aliquot of cells showed that the purity of $CD117^+$ cell isolation was typically >93-94% as determined by flow cytometry.

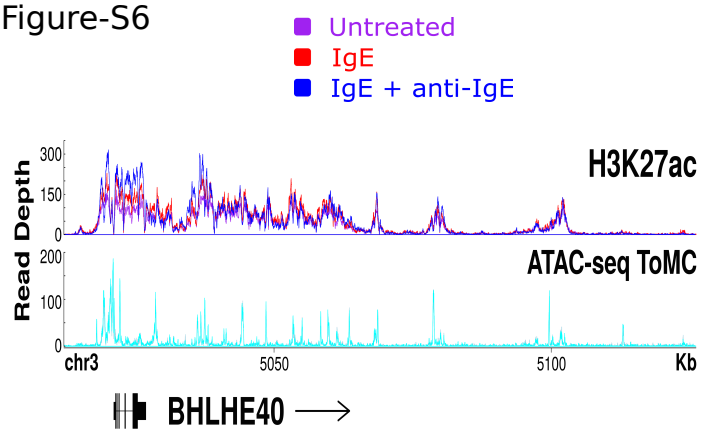
B) Magnetically isolated $CD117^+$ cells were then used for sorting with FcεRI-APC antibody (clone CRA1). Gating strategy was shown. Sorted $CD117^+$ $FcεRI^+$ tonsillar MCs were used for Omni-ATAC-seq.

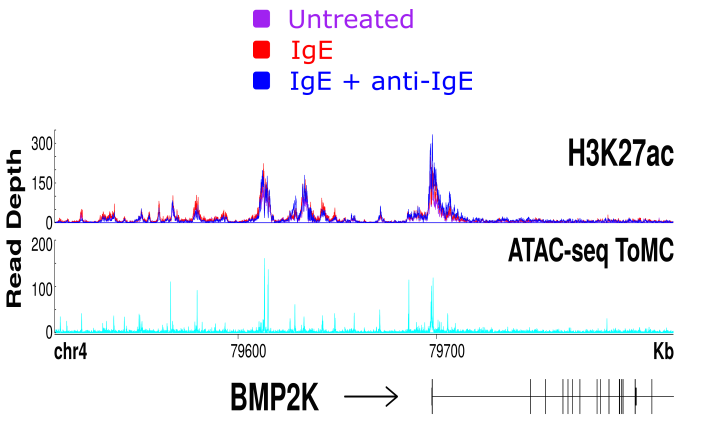
C) The number of isolated tonsillar MCs from each donor was indicated (n=7 donors). Omni-ATAC-seq peaks in TPSAB1 and HDC loci from tonsillar MCs were shown.

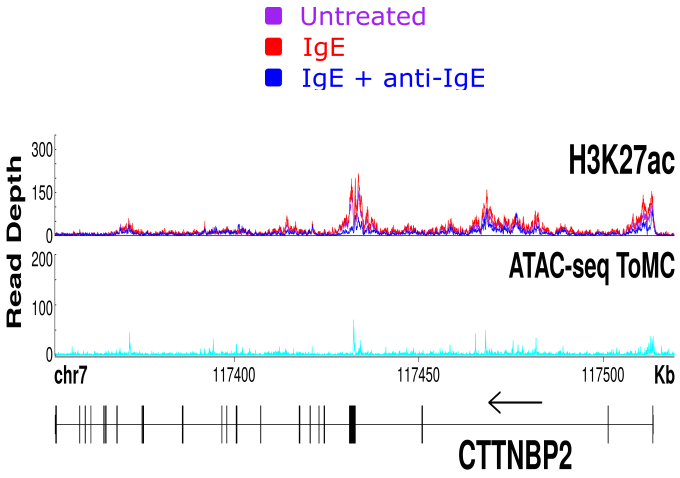
D) IGV tracks of CXCL8 (IL-8) gene loci in untreated and IgE+anti-IgE-treated peripheral blood-derived MCs (HMC) and in isolated tonsillar MCs (ToMC). Data are from 2 independent biological replicates.

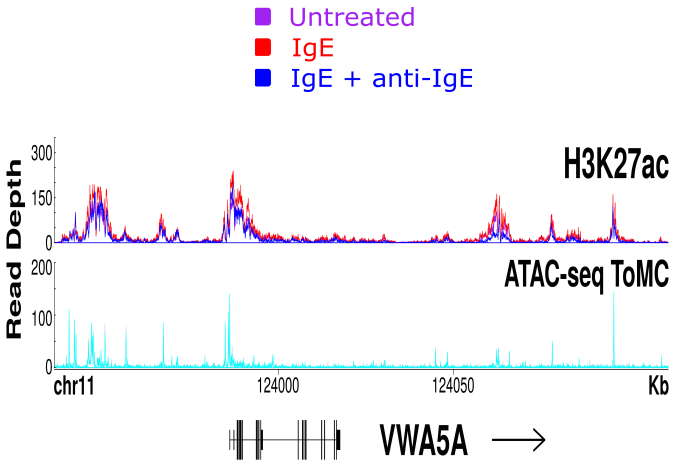
E) IGV tracks of CSF2 gene loci in untreated and IgE+anti-IgE-treated peripheral blood-derived MCs (HMC) and in isolated tonsillar MCs (ToMC). Data are from 2 independent biological replicates.

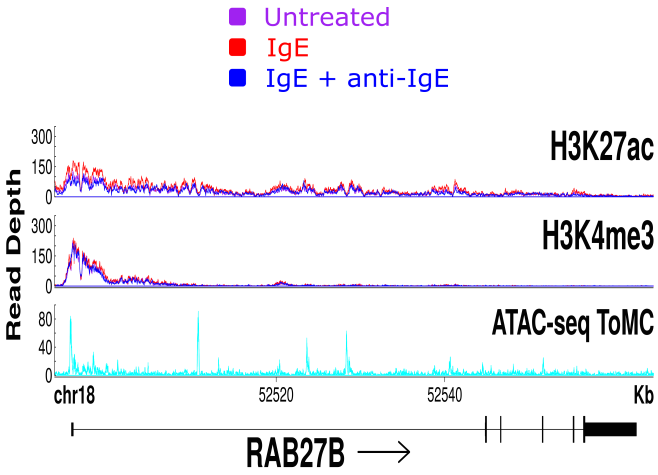
Figure-S6

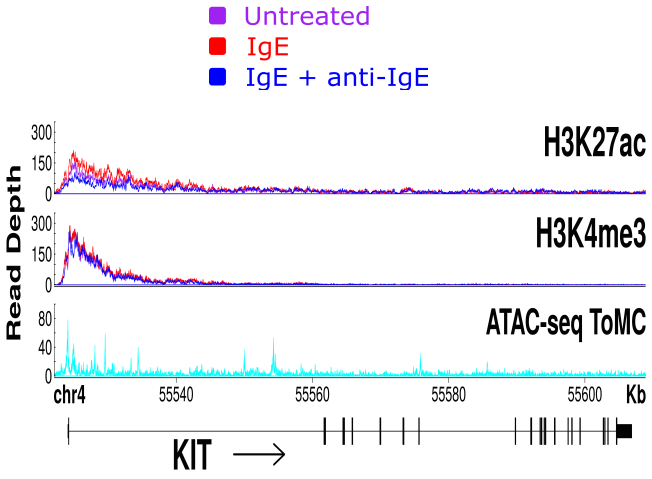

Untreated
IgE
IgE + anti-IgE
H3K27ac
ATAC-seq ToMC
Read Depth
chr3
5050
5100
Kb
BHLHE40

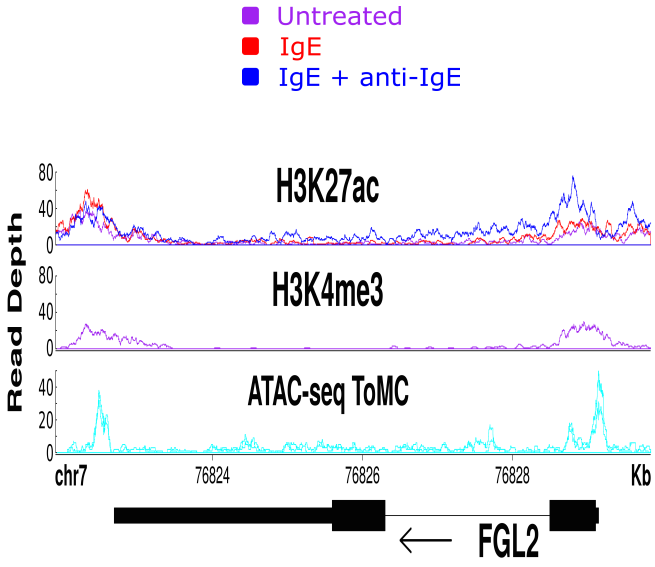

Untreated
IgE
IgE + anti-IgE
H3K27ac
ATAC-seq ToMC
Read Depth
chr4
79600
79700
Kb
BMP2K

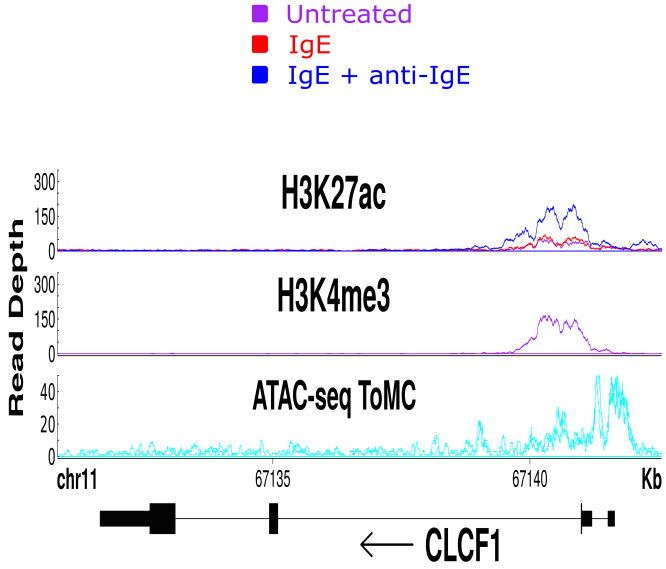

Untreated
IgE
IgE + anti-IgE
H3K27ac
ATAC-seq ToMC
Read Depth
chr7
117400
117450
117500
Kb
CTTNBP2


Untreated
IgE
IgE + anti-IgE
H3K27ac
ATAC-seq ToMC
Read Depth
chr11
124000
124050
Kb
VWA5A


Untreated
IgE
IgE + anti-IgE
H3K27ac
H3K4me3
ATAC-seq ToMC
Read Depth
chr18
52520
52540
Kb
RAB27B


Untreated
IgE
IgE + anti-IgE
H3K27ac
H3K4me3
ATAC-seq ToMC
Read Depth
chr4
55540
55560
55580
55600
Kb
KIT

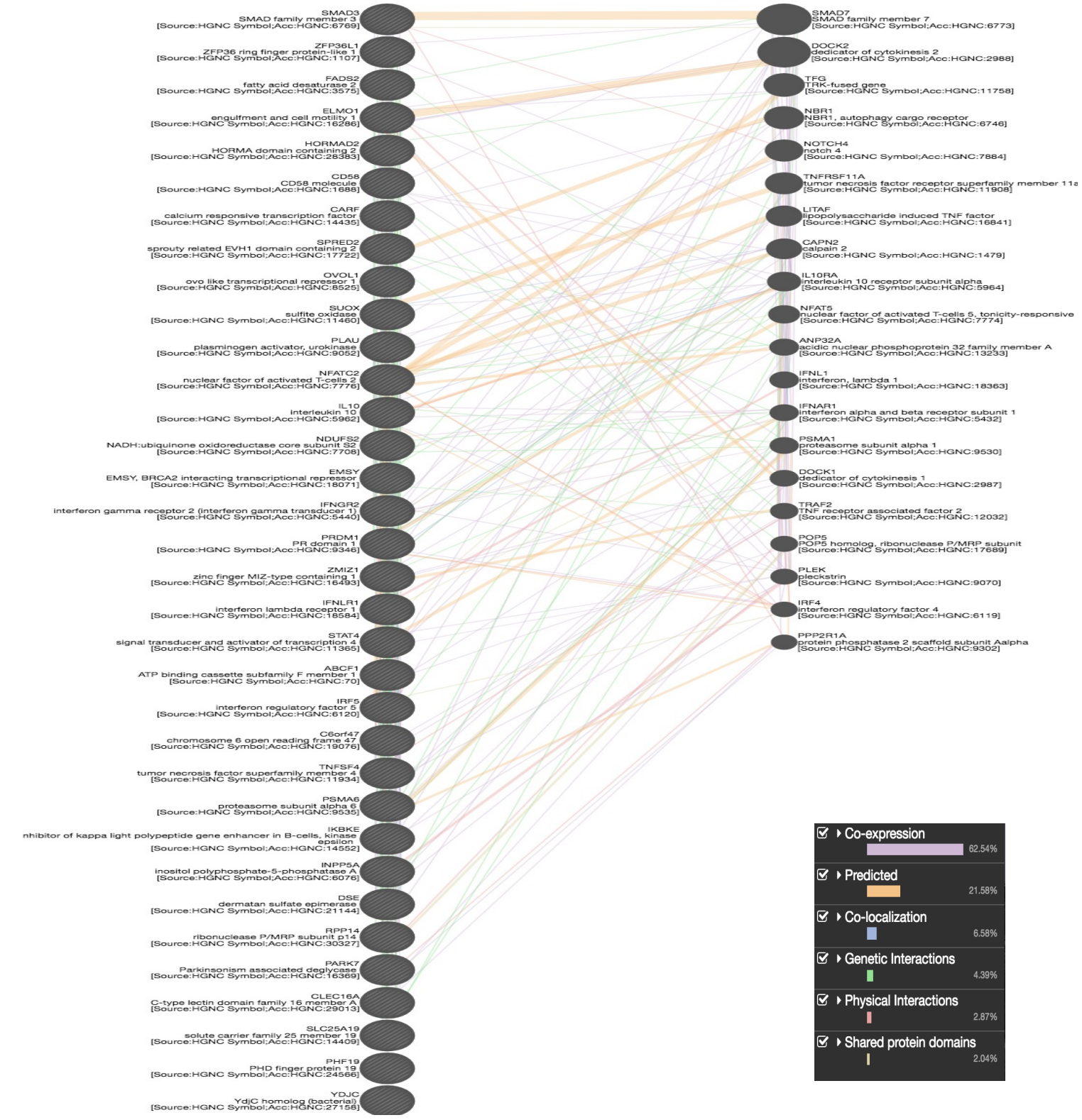

Untreated
IgE
IgE + anti-IgE
H3K27ac
H3K4me3
ATAC-seq ToMC
Read Depth
chr7
76824
76826
76828
Kb
FGL2


Untreated
IgE
IgE + anti-IgE
H3K27ac
H3K4me3
ATAC-seq ToMC
Read Depth
chr11
67135
67140
Kb
CLCF1

Supplementary Figure-6: Comparison of CHIP-seq peaks of peripheral blood-derived MCs with Omni-ATAC-seq peaks of tonsillar MCs. Related to Fig-1.

H3K27ac and H3K4me3 CHIP-seq peaks of peripheral blood-derived MCs were compared with Omni-ATAC-seq peaks of tonsillar MCs in indicated gene regions.

Figure-S7


SMAD3
SMAD family member 3
[Source:HGNC Symbol;Acc:HGNC:6769]
ZFP36L1
ZFP36 ring finger protein-like 1
[Source:HGNC Symbol;Acc:HGNC:1107]
FADS2
fatty acid desaturase 2
[Source:HGNC Symbol;Acc:HGNC:3575]
ELMO1
engulfment and cell motility 1
[Source:HGNC Symbol;Acc:HGNC:16286]
HORMAD2
HORMA domain containing 2
[Source:HGNC Symbol;Acc:HGNC:28393]
CD58
CD58 molecule
[Source:HGNC Symbol;Acc:HGNC:1688]
CARF
calcium responsive transcription factor
[Source:HGNC Symbol;Acc:HGNC:14435]
SPRED2
sprouty related EVH1 domain containing 2
[Source:HGNC Symbol;Acc:HGNC:17722]
OVOL1
ovo like transcriptional repressor 1
[Source:HGNC Symbol;Acc:HGNC:8525]
SUOX
sulfite oxidase
[Source:HGNC Symbol;Acc:HGNC:11460]
PLAU
plasminogen activator, urokinase
[Source:HGNC Symbol;Acc:HGNC:9052]
NFATC2
nuclear factor of activated T-cells 2
[Source:HGNC Symbol;Acc:HGNC:7776]
IL10
interleukin 10
[Source:HGNC Symbol;Acc:HGNC:5962]
NDUFS2
NADH:ubiquinone oxidoreductase core subunit S2
[Source:HGNC Symbol;Acc:HGNC:7708]
EMSY
EMSY, BRCA2 interacting transcriptional repressor
[Source:HGNC Symbol;Acc:HGNC:18071]
IFNGR2
interferon gamma receptor 2 (interferon gamma transducer 1)
[Source:HGNC Symbol;Acc:HGNC:5440]
PRDM1
PR domain 1
[Source:HGNC Symbol;Acc:HGNC:9346]
ZMIZ1
zinc finger MIZ-type containing 1
[Source:HGNC Symbol;Acc:HGNC:16493]
IFNLR1
interferon lambda receptor 1
[Source:HGNC Symbol;Acc:HGNC:18584]
STAT4
signal transducer and activator of transcription 4
[Source:HGNC Symbol;Acc:HGNC:11365]
ABCF1
ATP binding cassette subfamily F member 1
[Source:HGNC Symbol;Acc:HGNC:70]
IRF5
interferon regulatory factor 5
[Source:HGNC Symbol;Acc:HGNC:6120]
C6orf47
chromosome 6 open reading frame 47
[Source:HGNC Symbol;Acc:HGNC:19076]
TNFSF4
tumor necrosis factor superfamily member 4
[Source:HGNC Symbol;Acc:HGNC:11934]
PSMA6
proteasome subunit alpha 6
[Source:HGNC Symbol;Acc:HGNC:9535]
IKBKE
nhibitor of kappa light polypeptide gene enhancer in B-cells, kinase epsilon
[Source:HGNC Symbol;Acc:HGNC:14552]
INPP5A
inositol polyphosphate-5-phosphatase A
[Source:HGNC Symbol;Acc:HGNC:6076]
DSE
dermatan sulfate epimerase
[Source:HGNC Symbol;Acc:HGNC:21144]
RPP14
ribonuclease P/MRP subunit p14
[Source:HGNC Symbol;Acc:HGNC:30327]
PARK7
Parkinsonism associated deglycase
[Source:HGNC Symbol;Acc:HGNC:16369]
CLEC16A
C-type lectin domain family 16 member A
[Source:HGNC Symbol;Acc:HGNC:29013]
SLC25A19
solute carrier family 25 member 19
[Source:HGNC Symbol;Acc:HGNC:14409]
PHF19
PHD finger protein 19
[Source:HGNC Symbol;Acc:HGNC:24566]
YDJC
YdjC homolog (bacterial)
[Source:HGNC Symbol;Acc:HGNC:27158]
SMAD7
SMAD family member 7
[Source:HGNC Symbol;Acc:HGNC:6773]
DOCK2
dedicator of cytokinesis 2
[Source:HGNC Symbol;Acc:HGNC:2988]
TFG
TRK-fused gene
[Source:HGNC Symbol;Acc:HGNC:11758]
NBR1
NBR1, autophagy cargo receptor
[Source:HGNC Symbol;Acc:HGNC:6746]
NOTCH4
notch 4
[Source:HGNC Symbol;Acc:HGNC:7884]
TNFRSF11A
tumor necrosis factor receptor superfamily member 11a
[Source:HGNC Symbol;Acc:HGNC:11908]
LITAF
lipopolysaccharide induced TNF factor
[Source:HGNC Symbol;Acc:HGNC:16841]
CAPN2
calpain 2
[Source:HGNC Symbol;Acc:HGNC:1479]
IL10RA
interleukin 10 receptor subunit alpha
[Source:HGNC Symbol;Acc:HGNC:5964]
NFAT5
nuclear factor of activated T-cells 5, tonicity-responsive
[Source:HGNC Symbol;Acc:HGNC:7774]
ANP32A
acidic nuclear phosphoprotein 32 family member A
[Source:HGNC Symbol;Acc:HGNC:13233]
IFNL1
interferon, lambda 1
[Source:HGNC Symbol;Acc:HGNC:18363]
IFNAR1
interferon alpha and beta receptor subunit 1
[Source:HGNC Symbol;Acc:HGNC:5432]
PSMA1
proteasome subunit alpha 1
[Source:HGNC Symbol;Acc:HGNC:9530]
DOCK1
dedicator of cytokinesis 1
[Source:HGNC Symbol;Acc:HGNC:2987]
TRAF2
TNF receptor associated factor 2
[Source:HGNC Symbol;Acc:HGNC:12032]
POP5
POP5 homolog, ribonuclease P/MRP subunit
[Source:HGNC Symbol;Acc:HGNC:17689]
PLEK
pleckstrin
[Source:HGNC Symbol;Acc:HGNC:9070]
IRF4
interferon regulatory factor 4
[Source:HGNC Symbol;Acc:HGNC:6119]
PPP2R1A
protein phosphatase 2 scaffold subunit Aalpha
[Source:HGNC Symbol;Acc:HGNC:9302]
Co-expression
62.54%
Predicted
21.58%
Co-localization
6.58%
Genetic Interactions
4.39%
Physical Interactions
2.87%
Shared protein domains
2.04%

Supplementary Figure-7: Network analysis of genes harbouring disease-associated SNPs located in Omni-ATAC-seq peaks of tonsillar MCs. Related to Fig-7.

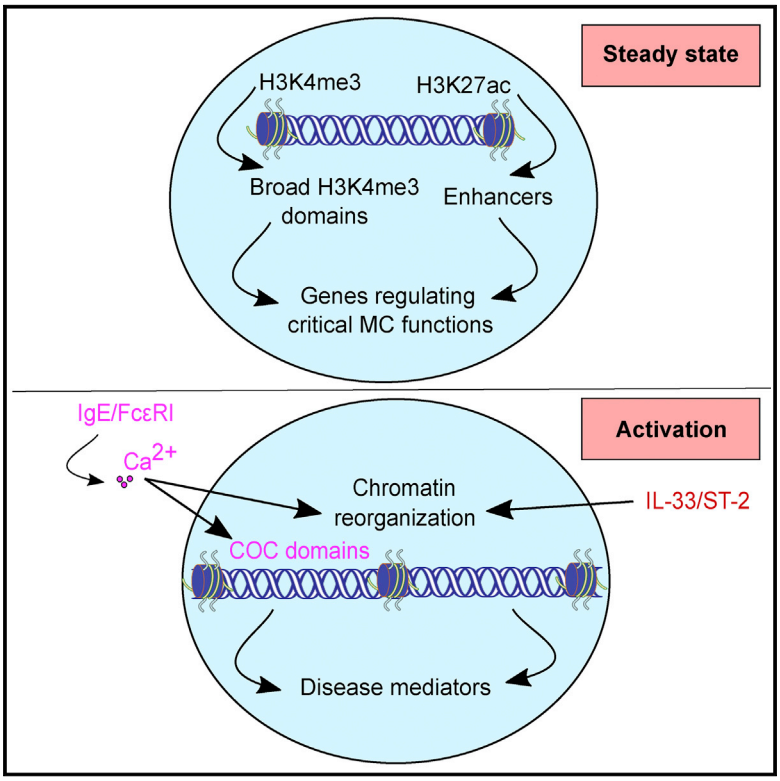
Network analysis of genes harbouring SNPs located in Omni-ATAC-seq peaks of tonsillar MCs using GeneMANIA tool. This analysis showed whether the indicated proteins are co-expressed, have predicted interactions, take part in same biological pathways, have shared protein domains, are colocalized or have known physical interactions.

Resource

Immunity

Genome-wide Analyses of Chromatin State in Human Mast Cells Reveal Molecular Drivers and Mediators of Allergic and Inflammatory Diseases

Graphical Abstract



Authors

Gökhan Cildir, John Toubia, Kwok Ho Yip, ..., Michele A. Grimbaldeston, Angel F. Lopez, Vinay Tergaonkar

Correspondence

vinayt@imcb.a-star.edu.sg

In Brief

Cildir et al. map the genomic and transcriptomic changes in human mast cells upon diverse stimuli, defining chromatin changes associated with activation and Ca^{2+} flux and revealing potential effectors of mast cell function. Disease-associated SNPs mapped onto *cis*-regulatory regions of mast cells suggest that mast cell function may impact a broad range of pathologies.

Highlights

- Enhancers and broad H3K4me3 domains are enriched in genes regulating MC functions
- Intracellular calcium levels govern the chromatin landscape upon FcεRI crosslinking
- Disease-associated SNPs are enriched in regulatory chromatin regions of human MCs

Cildir et al., 2019, Immunity *51*, 949–965
November 19, 2019 © 2019 Elsevier Inc.
https://doi.org/10.1016/j.immuni.2019.09.021

CellPress

Immunity
Resource

Genome-wide Analyses of Chromatin State in Human Mast Cells Reveal Molecular Drivers and Mediators of Allergic and Inflammatory Diseases

Gökhan Cildir,[1,2] John Toubia,[1,3] Kwok Ho Yip,[1] Mingyan Zhou,[1] Harshita Pant,[5] Pravin Hissaria,[6] Jingxian Zhang,[4] Wanjin Hong,[4] Nirmal Robinson,[1] Michele A. Grimbaldeston,[7] Angel F. Lopez,[1] and Vinay Tergaonkar[1,2,8,9,*]
[1]Centre for Cancer Biology, University of South Australia and SA Pathology, Adelaide, SA 5000, Australia
[2]Laboratory of NF-κB Signaling, Institute of Molecular and Cell Biology (IMCB), 61 Biopolis Drive, Proteos, Singapore 138673, Singapore
[3]ACRF Cancer Genomics Facility, Centre for Cancer Biology, University of South Australia and SA Pathology, Adelaide, SA 5000, Australia
[4]Institute of Molecular and Cell Biology (IMCB), 61 Biopolis Drive, Proteos, Singapore 138673, Singapore
[5]School of Medicine, University of Adelaide, Adelaide, SA, Australia
[6]Royal Adelaide Hospital, Adelaide, SA 5000, Australia
[7]OMNI-Biomarker Development, Genentech Inc, South San Francisco, CA 94080, USA
[8]Department of Pathology, Yong Loo Lin School of Medicine, National University of Singapore, Singapore 119074, Singapore
[9]Lead Contact
*Correspondence: vinayt@imcb.a-star.edu.sg
https://doi.org/10.1016/j.immuni.2019.09.021

SUMMARY

Mast cells (MCs) are versatile immune cells capable of rapidly responding to a diverse range of extracellular cues. Here, we mapped the genomic and transcriptomic changes in human MCs upon diverse stimuli. Our analyses revealed broad H3K4me3 domains and enhancers associated with activation. Notably, the rise of intracellular calcium concentration upon immunoglobulin E (IgE)-mediated crosslinking of the high-affinity IgE receptor (FcεRI) resulted in genome-wide reorganization of the chromatin landscape and was associated with a specific chromatin signature, which we term Ca^{2+}-dependent open chromatin (COC) domains. Examination of differentially expressed genes revealed potential effectors of MC function, and we provide evidence for fibrinogen-like protein 2 (FGL2) as an MC mediator with potential relevance in chronic spontaneous urticaria. Disease-associated single-nucleotide polymorphisms mapped onto *cis*-regulatory regions of human MCs suggest that MC function may impact a broad range of pathologies. The datasets presented here constitute a resource for the further study of MC function.

INTRODUCTION

Allergic diseases such as asthma, allergic rhinitis (hay fever), atopic dermatitis (eczema), and food allergies afflict millions of individuals worldwide, and a large number of immunomodulatory molecules are causally linked to allergic symptoms in the skin, lung, and gastrointestinal tract (de Kleer et al., 2016; Lyons and Milner, 2018; Tordesillas et al., 2017). In these diseases, *in situ* recognition of allergens, processing of allergic peptides by antigen-presenting cells, generation of a predominant T helper 2 (Th2)-type cell response, and production of allergen-specific immunoglobulin E (IgE) by class-switched B cells represent the chain of events in an allergen-specific immune response (Platts-Mills and Woodfolk, 2011). IgE binding to the high-affinity IgE receptor (FcεRI) on target cells such as mast cells (MCs) and basophils sensitizes these cells to subsequent exposure to specific antigens that crosslink FcεRI molecules in the membrane (Galli and Tsai, 2012).

MCs are tissue-resident immune cells with important roles in innate and adaptive immune responses. MCs contain cytoplasmic granules that store bioactive molecules including, but not limited to, proteases, cytokines, and biologically active amines (Cildir et al., 2017). Diverse stimuli trigger MC activation through IgE-dependent or -independent mechanisms in different pathologies (McNeil et al., 2015; Redegeld et al., 2018; St John and Abraham, 2013). IgE-mediated FcεRI crosslinking is the most common initiator of MC activation during allergic responses. In certain individuals, anaphylactic responses resulting from the crosslinking of FcεRIs turn fatal due to uncontrolled release of MC mediators. In addition, cytokines such as interleukin (IL)-33 also regulate MC functions (Cayrol and Girard, 2018).

Organization of the chromatin landscape is an important mechanism in controlling cell-type-specific functions in the immune system (Beyaz et al., 2017; Bunting et al., 2016; Johnson et al., 2018). Enhancers are important *cis*-regulatory elements typically located far away from transcriptional start sites (TSSs) and characterized by the presence of specific post-translational modifications of histones and nucleosome-depleted regions. Enhancers positively regulate gene expression by long-range interactions with the gene promoters (Long et al., 2016) and play central roles in cellular differentiation and function. Lineage-specific or signal-activated transcription factors (TFs) bind to enhancers and regulate the recruitment of other co-factors and the general transcriptional

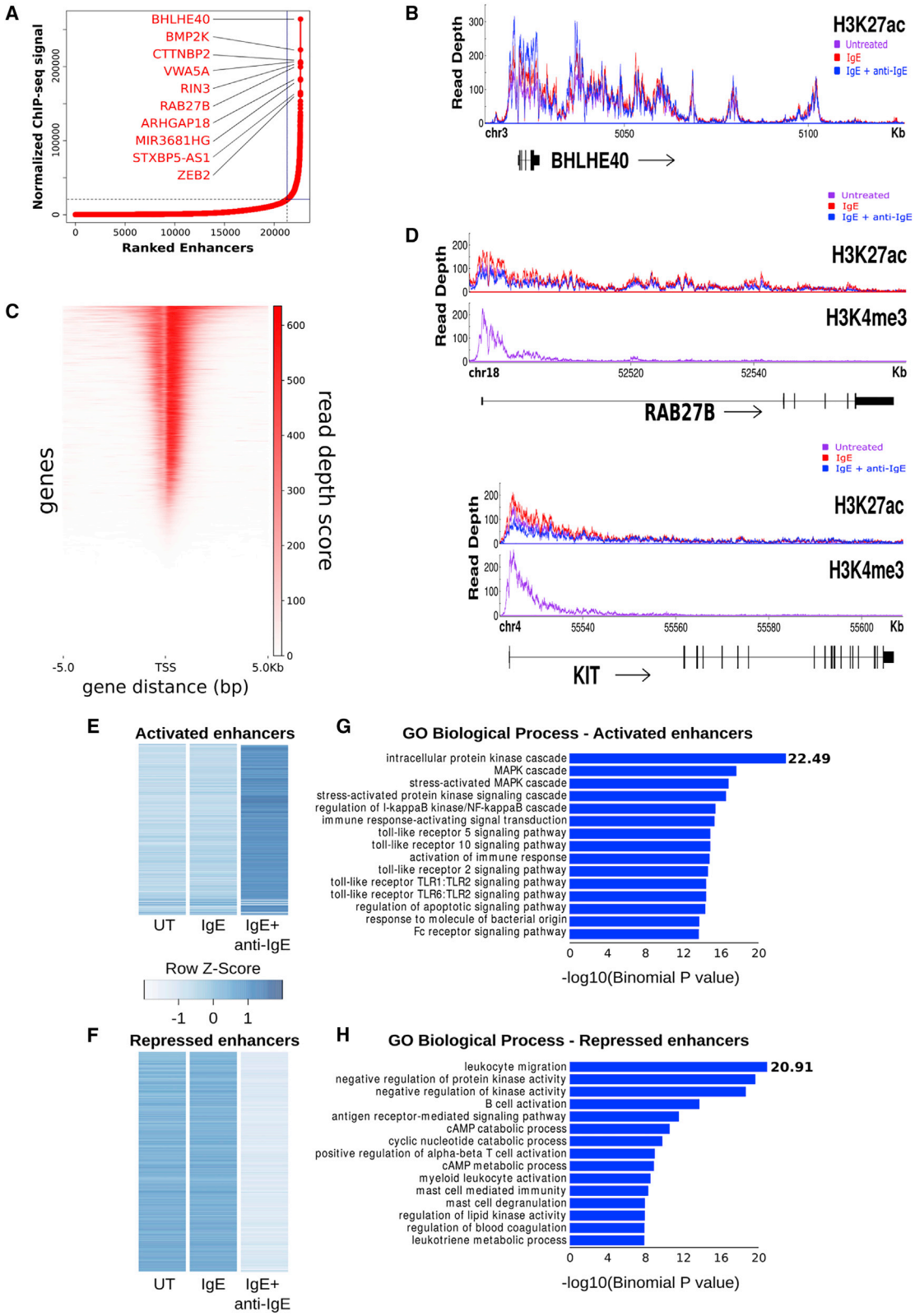


Figure 1. Epigenomic Profiling of Human Peripheral-Blood-Derived MCs

(A) ROSE was used to identify top enhancers based on normalized H3K27ac ChIP-seq signals. Genes harboring top-10 enhancer regions were indicated. Data are from two independent biological replicates.

(legend continued on next page)

machinery (Shlyueva et al., 2014). Chromatin immunoprecipitation sequencing (ChIP-seq) analysis of histone acetyltransferase p300 or different combinations of histone marks, such as H3K4me1, H3K4me2, and H3K27Ac or DNase I hypersensitivity assays, can be used to identify various classes of enhancers (Calo and Wysocka, 2013). The activation of enhancers is cell-type and stimulus specific, and alterations in enhancer activation are associated with disease progression in various settings (Rickels and Shilatifard, 2018). Therefore, characterization of cell-type-specific epigenome, including enhancers and other *cis*-regulatory elements, is an active area of investigation (Davis et al., 2017; Kundaje et al., 2015; Stunnenberg et al., 2016). Similar to enhancers, broad H3K4me3 domains, extending from a TSS to a gene body to achieve transcriptional consistency, are also linked to the cell-type identity and cell-type-enriched functions (Benayoun et al., 2014). In line with this, broad H3K4me3 domains play important roles in developmental programs and disease progression (Chen et al., 2015; Dahl et al., 2016; Dhar et al., 2018).

Chromatin profiling is a powerful tool in identifying the molecular drivers of disease and studying the roles of disease-associated variants in the immune system. Given the critical roles of MCs in allergic and inflammatory diseases, profiling the human MC chromatin landscape holds potential in gaining crucial insights into the roles of these cells in health and disease. Here, we examined the chromatin landscape of resting and activated human MCs from peripheral blood and defined enhancer regions and broad H3K4me3 domains. Changes in intracellular calcium levels upon crosslinking of FcεRI, unlike activation of IL-33 receptor ST2 (IL1RL1), were central to the genome-wide reorganization of the enhancer landscape. Chromatin accessibility analyses defined Ca^{2+}-dependent open chromatin (COC) domains induced upon FcεRI crosslinking in human MCs. These genome-wide changes were also observed in tonsillar MCs isolated from patients with tonsilitis. Using these epigenomic and transcriptomic analyses, we further identified FGL2 as a human-MC-derived soluble mediator and showed that expression of FGL2 is increased in urticaria skin samples. We mapped disease-associated single-nucleotide polymorphisms (SNPs) from 30 inflammatory and autoimmune diseases to regulatory regions in human MCs. These comprehensive epigenomic analyses provide a resource for the identification of regulators of human MC functions and for the further understanding of the impact of MCs in disease.

RESULTS

Characterization of the Enhancer and Broad H3K4me3 Domain Repertoire of Human MCs

To interrogate the enhancer repertoire of human MCs, we first used peripheral-blood-derived MCs, performed H3K27ac ChIP-seq, and ranked enhancers with H3K27ac mark as previously described (Whyte et al., 2013). We consistently obtained highly purified MCs (>98%), very similar biological replicates in terms of H3K27ac reads, and high-quality ChIP-seq datasets with negative and positive control regions (Figures S1A–S1E; Table S1). Using Rank Ordering of Super Enhancers (ROSE), we identified top enhancer regions in human MCs (Figure 1A; Table S1). When genes nearest to these enhancers were further investigated, genes with known functions in MCs, such as RIN3 (Janson et al., 2012), RAB27B (Mizuno et al., 2007), and ZEB2 (Barbu et al., 2012), as well as numerous genes with as-yet-unknown functions in MCs, were identified (Table S1). A snapshot of the top enhancer in BHLHE40 locus, whose function is unknown in human MCs, is shown in Figure 1B, and the other top 4 enhancers are shown in Figure S1F.

To further identify broad H3K4me3 domains of human MCs, we performed H3K4me3 ChIP-seq and ranked genome-wide H3K4me3 signals that were highly enriched in TSS regions (Figure 1C). Typical H3K4me3 signals were around 2 kb, whereas genes with important functions in MCs, such as RAB27B and KIT, showed up to 20 kb H3K4me3 signals (Figure 1D; Table S1). Many genes harboring top enhancer regions were also found to possess broad H3K4me3 domains (Table S1), suggesting cooperation between different chromatin entities to regulate higher-order chromatin structure in human MCs.

FcεRI Crosslinking Governs Specific Enhancer Dynamics in Human MCs

To gain further insights into chromatin reorganization and possible enhancer remodeling in response to FcεRI crosslinking (IgE+anti-IgE treatment), we used H3K27ac as an active enhancer mark (Creyghton et al., 2010). We observed a genome-wide activation and repression of specific chromatin regions upon FcεRI crosslinking, but not upon IgE-sensitization alone (Figure S2; Table S1). We then specifically focused on typical enhancers as previously annotated (Farh et al., 2015) and identifed FcεRI-crosslinking-mediated activated and repressed distal enhancers (Figures 1E and 1F). To further explore these remodeled enhancers, differential H3K27ac

(B) Sushi plot of top enhancer in BHLHE40 gene in untreated, IgE-sensitized, and IgE+anti-IgE-treated conditions. Data are from two independent biological replicates.

(C) Using heatmap analysis, genome-wide H3K4me3 signals were ranked in TSS regions with 5 kb window size. Each red line represents a unique H3K4me3 peak. Data are from two independent biological replicates.

(D) Sushi plot of H3K4me3 and H3K27ac signals in RAB27B and KIT genes in untreated, IgE-sensitized, and IgE+anti-IgE-treated conditions. Data are from two independent biological replicates.

(E) Using H3K27ac ChIP-seq datasets, activated enhancer regions upon IgE+anti-IgE treatment compared to untreated MCs were identified. Each blue line represents a unique activated enhancer region. Data are from two independent biological replicates.

(F) Using H3K27ac ChIP-seq datasets, repressed enhancer regions upon IgE+anti-IgE treatment compared to untreated MCs were identified. Each blue line represents a unique repressed enhancer region. Data are from two independent biological replicates.

(G) Top 15 significantly enriched Gene Ontology (GO) biological process terms for activated enhancers as determined by the Database for Annotation, Visualization, and Integrated Discovery (DAVID) software. Data are from two independent biological replicates.

(H) Top 15 significantly enriched GO biological process terms for repressed enhancers as determined by the DAVID software. Data are from two independent biological replicates.

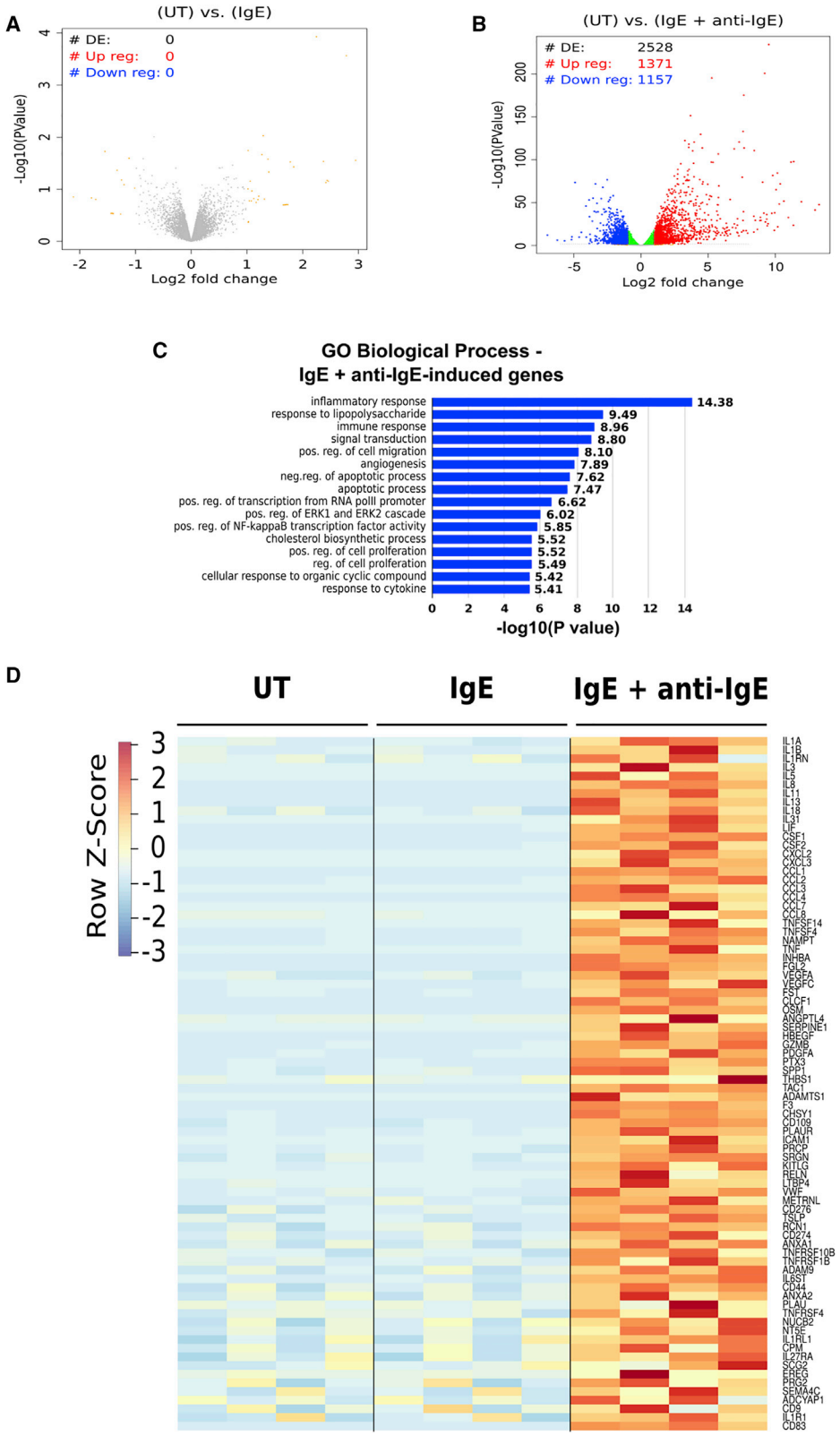


Figure 2. Characterization of Human MC Transcriptome upon FcεRI Crosslinking

(A) Volcano plot showing the differentially expressed genes in IgE-sensitized versus untreated human MCs using paired-end RNA-seq results with four independent biological replicates. Log_2 fold change:1, FDR: 0.05, p = 0.05.

(legend continued on next page)

ChIP-seq peaks were assigned to their nearest genes. Gene Ontology (GO) analysis for the activated enhancers identified significantly enriched biological processes, such as mitogen-activated protein kinase (MAPK) and nuclear factor κB (NF-κB) signaling pathway, regulation of apoptotic signaling pathway, and activation of immune response (Figure 1G). Similarly, repressed enhancers were also associated with distinct GO terms such as negative regulation of protein kinase activity, antigen-receptor-mediated signaling pathway, and MC-mediated immunity (Figure 1H).

Identification of Fibrinogen-like Protein 2 (FGL2) as an MC Mediator

Coupled to the chromatin analysis, we also interrogated the human MC transcriptome with paired-end RNA sequencing (RNA-seq) with 4 independent biological replicates. Similar to H3K27ac ChIP-seq results (Figures S2A and S2C), IgE-sensitization alone did not lead to significant changes in gene expression (Figure 2A). On the other hand, anti-IgE stimulation of IgE-sensitized cells altered the expression of >2,500 RNAs (log_2 fold change: 1; false discovery rate [FDR]: 0.05, p: 0.05) (Figure 2B; Table S2). GO analysis indicated that genes induced upon FcεRI crosslinking were involved in processes such as inflammatory response, apoptotic response, and angiogenesis, among others (Figure 2C). We further validated RNA-seq results by performing RT-qPCR on selected genes such as chemokine (C-C motif), ligand 1 (CCL1), and CCL4, whose expression was highly increased upon FcεRI crosslinking (Figures S3A and S3B).

MCs release a diverse array of soluble mediators via degranulation and conventional exocytosis (Blank et al., 2014). To gain insights into human MC mediators, we limited our RNA-seq analysis only to genes coding for secretory proteins after FcεRI crosslinking. To this end, we first filtered differentially expressed protein-coding transcripts (with mean counts per million [CPM] value >10) using the Human Protein Atlas database (Thul et al., 2017) for "predicted secreted proteins" and cell surface proteins with known extracellular soluble forms. Then, we scoured the published literature to identify bona fide secretory proteins. Using this approach, we identified 80 secretory mediators, including proteins known to be involved in allergic inflammation, such as IL-31, Pentraxin 3 (PTX3), and Oncostatin M (OSM) (Figure 2D). We also identified fibrinogen-like protein 2 (FGL2) and cardiotrophin-like cytokine factor 1 (CLCF1) as candidate soluble mediators produced by human MCs. FGL2 is implicated in several human diseases such as glioma, renal carcinoma, and inflammatory bowel disease (IBD) (Dong et al., 2014; Tang et al., 2017; Yan et al., 2015) and exists in two different forms: membrane-bound and secreted. Regulatory T cells (Tregs) secrete FGL2 (Hu et al., 2016), and FGL2 plays a critical role in some settings, such as in T cell immunoreceptor with Ig and ITIM domains (TIGIT)-induced Treg-mediated suppression of Th1 and Th17, but not in Th2 cell responses (Joller et al., 2014). FGL2 is also associated with cellular damage in cell types such as sinusoidal endothelial cells (Selzner et al., 2012). CLCF1 is a member of the IL-6 family of cytokines involved in cold-induced sweating syndrome (Rousseau et al., 2006).

We confirmed in our H3K27ac ChIP-seq datasets that FGL2 loci were modified upon FcεRI crosslinking (Figure 3A). In line with this, FGL2 mRNA expression was highly increased upon FcεRI crosslinking as determined by RT-qPCR (Figure 3B). To understand whether human MC-derived FGL2 is a secretory mediator, we performed FGL2 enzyme-linked immunosorbent assay (ELISA) in culture supernatants and found that MCs secrete high levels of FGL2 upon FcεRI crosslinking (>3 ng/mL FGL2 per 2 × 10^5 human MCs) (Figure 3C). On the other hand, although CLCF1 loci were also identified to be modified in H3K27ac ChIP-seq datasets (Figure S3C) and CLCF1 mRNA levels were also highly increased upon FcεRI crosslinking (Figure S3D), we could not detect measurable amounts of secreted CLCF1 (<0.1 pg/mL CLCF1/2 × 10^5 human MCs) upon FcεRI crosslinking using two different commercially available ELISA kits (Figure S3E). This highlights the notion that CLCF1 is unable to be efficiently secreted on its own and may require additional factors for secretion (Sims, 2015). As a positive control for the secretory mediators of activated human MCs, we detected IL-4 in the same supernatants (Figure S3F).

To further investigate whether our findings on FGL2 using peripheral-blood-derived human MCs have clinical relevance in the context of allergic diseases where MCs are involved, we focused on chronic spontaneous urticaria (CSU) patients. CSU, also known as itchy hives, is an inflammatory skin condition involving IgE-mediated MC activation (Siebenhaar et al., 2018). After a reported acute allergic reaction in a cohort of CSU patients, biopsy samples from lesional and non-lesional skin were collected and processed to check whether FGL2 could be detected in skin-resident human MCs. To this end, we performed confocal microscopy analysis co-staining for MC tryptase and FGL2. FGL2 foci colocalizing with MCs were significantly increased in lesional CSU skin samples compared to non-lesional samples (Figures 3D–3F) in line with our findings using IgE-activated peripheral-blood-derived human MCs.

Identification of COC Domains upon FcεRI Crosslinking in Human MCs

FcεRI crosslinking triggers the increase of intracellular calcium levels in MCs, which is critical for the fusion of cytoplasmic granules with the plasma membrane upon MC activation (Nishida et al., 2005). Given the epigenomic changes that we observed upon FcεRI crosslinking, we asked whether intracellular calcium levels modulate the chromatin landscape. To investigate the role of intracellular calcium in chromatin reorganization after FcεRI crosslinking, we used BAPTA-AM, a highly selective and cell-

(B) Volcano plot showing the differentially expressed genes in IgE+anti-IgE-treated versus untreated human MCs using paired-end RNA-seq results with four independent biological replicates. Log_2 fold change: 1, FDR: 0.05, p = 0.05.

(C) Top 16 significantly enriched GO biological process terms for the genes with increased expression in IgE+anti-IgE-treated versus untreated human MCs as determined by the DAVID software. Data are from four independent biological replicates.

(D) Heatmap analysis of 80 genes with significantly increased expression (with >10 counts per million [CPM] cutoff values as determined by EdgeR normalization) upon IgE+anti-IgE stimulation and coding for secretory proteins using RNA-seq results with four independent biological replicates. Log_2 fold change: 1, FDR: 0.05, p = 0.05.

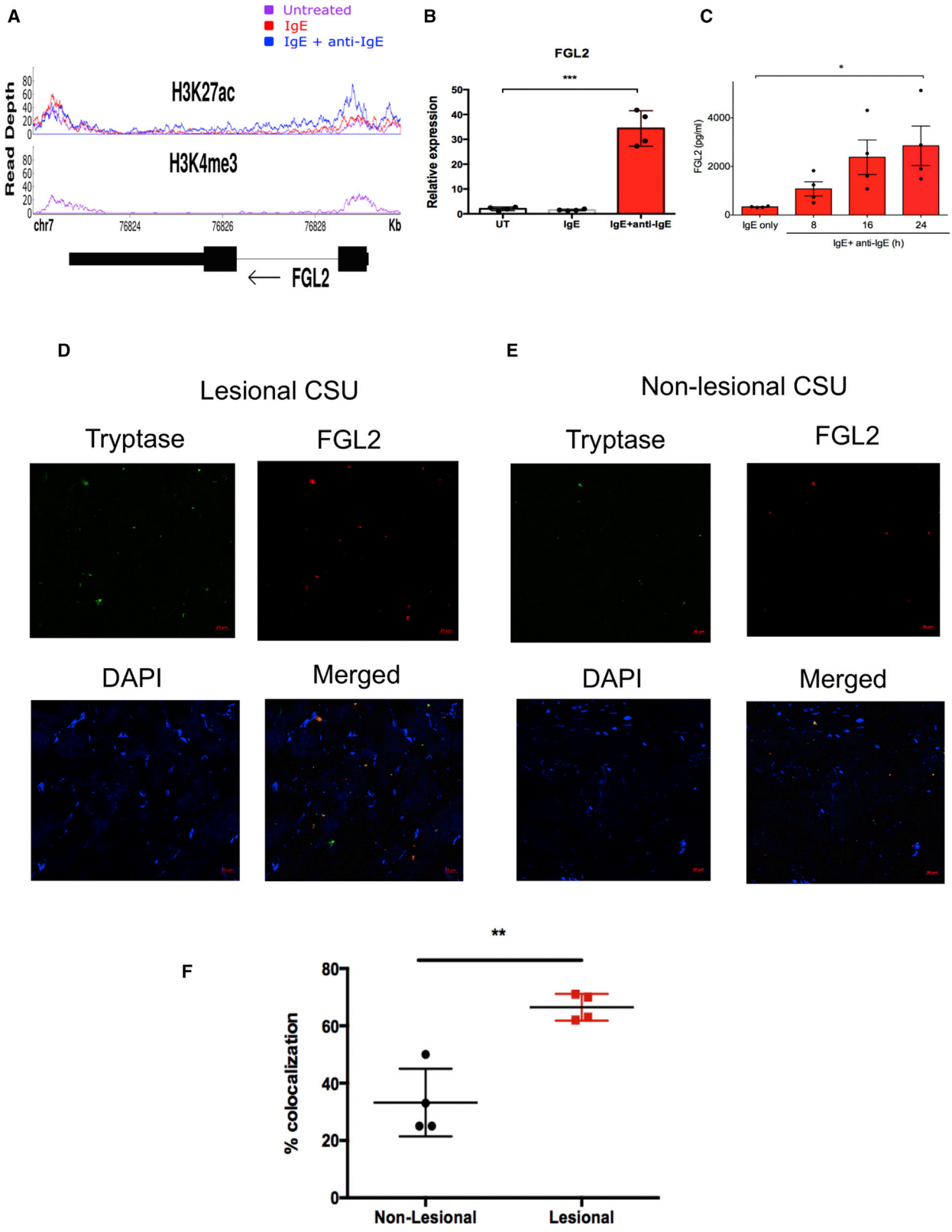


Figure 3. FGL2 is a Human MC-Derived Mediator

(A) Sushi plot of H3K27ac signals of human FGL2 loci in untreated, IgE-sensitized, and IgE+anti-IgE-treated conditions and H3K4me3 signals in untreated condition. Data are from two independent biological replicates.

(legend continued on next page)

permeant calcium chelator. IgE-sensitized human peripheral-blood-derived MCs were pretreated with BAPTA-AM (30 min, 20 μM) or DMSO control before anti-IgE treatment. As expected, BAPTA-AM almost completely blocked anti-IgE-mediated intracellular calcium increase as determined by time-lapse imaging of calcium indicator Fluo-3 AM-loaded human MCs (Figures 4A and 4B). To find out the effects of calcium depletion in chromatin reorganization, we performed Omni-ATAC-seq, an improved version of ATAC-seq that substantially eliminates reads from the mitochondrial genome (Corces et al., 2017). Principal-component analysis (PCA) (Figure 4C) and cluster analysis (Figure 4D) suggested a very high correlation of biological replicates in each treatment condition. Differential Omni-ATAC-seq peak analysis suggested that 2 h treatment with anti-IgE resulted in the opening of chromatin regions in thousands of genomic loci (Figure 4E; Table S3). Moreover, 24 h treatment with anti-IgE led to further reorganization of thousands of new loci, suggesting a dynamic nature of chromatin response (Figure S4, Table S4). A large proportion of Omni-ATAC-seq peaks (92%) was significantly dampened by BAPTA-AM treatment compared to DMSO control (Figure 4F), suggesting an essential role of intracellular calcium for chromatin opening in human MCs. We defined this chromatin signature as Ca^{2+}-dependent COC domains. The majority of Omni-ATAC-seq peaks were located in intronic and intergenic chromatin regions together with promoters (Figure 4G). Similarly, COC domains were also highly enriched in intronic and intergenic regions in human MCs (Figure 4H). TF motif analysis in COC domains indicated binding sites for several TFs such as ATF3, BATF, and AP-1 complex (Figure 5A), all of which are implicated in regulating allergic inflammation (Gilchrist et al., 2010; Lee et al., 2004; Übel et al., 2014). Peak affinities for these binding sites were significantly decreased upon BAPTA-AM treatment (Figure 5B). Thus, the elevation of cytoplasmic calcium levels mediated through endoplasmic reticulum calcium channels and store-operated calcium entry (SOCE) (Suzuki et al., 2012) not only regulates the fusion of granules with the membrane, but also determines a distinct chromatin signature in human MCs.

IL-33 Stimulation Reveals Conserved and Distinct Features of Chromatin Reorganization upon FcεRI Crosslinking

IL-33 is an IL-1 family member nuclear cytokine, and IL-33 receptor (also known as ST2 or IL1RL1) is highly expressed in MCs. Extracellular IL-33 is critically involved in allergic inflammation and has context-dependent functions (Cayrol and Girard, 2018). For instance, IL-33 pre-treatment increases the magnitude of IgE-mediated MC degranulation and chemokine synthesis (Joulia et al., 2017). However, IL-33 treatment alone does not induce calcium mobilization, degranulation, or NFAT pathway activation in MCs, unlike IgE-mediated activation (Andrade et al., 2011; Ball et al., 2018; Joulia et al., 2017). Therefore, the impact of IL-33 on MC chromatin reorganization is also largely unknown. We used Omni-ATAC-seq to investigate IL-33-mediated genome-wide chromatin remodeling and compared this signature with MC activation upon FcεRI crosslinking. IL-33 treatment for 2 h resulted in genome-wide chromatin opening in thousands of genomic locations (Figure 5C; Table S4). TF motif analysis in IL-33-induced Omni-ATAC-seq peaks identified significantly enriched sites for ATF3, BATF, and AP-1 complex (Figure 5D). We then compared these Omni-ATAC-seq peaks with peaks identified upon FcεRI crosslinking and observed both conserved and distinct chromatin regions (Figure 5E; Table S4). When the conserved peaks identified upon both FcεRI crosslinking and IL-33 treatment were compared with COC domains, we observed that 9,805 of 12,071 Omni-ATAC-seq peaks (81.2%) were unique to COC domains (Table S7), suggesting that IL-33 treatment recapitulated the opening of calcium-dependent domains only to a certain extent (Figure 5E). However, the ability of IL-33—which does not increase intracellular calcium levels—to reorganize certain COC domains suggested the existence of chromatin regions in human MCs that were equally responsive to different stimuli. Given the capacity of MCs to recognize a wide range of danger signals, these chromatin regions might provide important clues to the evolutionary adaptations of MC functions.

Peripheral-Blood-Derived Human MCs Recapitulate Unique Features of Human Tissue-Resident MCs

MCs are tissue-resident immune cells that show transcriptomic and phenotypic plasticity depending on the developmental origin and tissue location (Dwyer et al., 2016; Gentek et al., 2018; Li et al., 2018). To investigate whether genomic and transcriptomic signatures observed in human peripheral-blood-derived MCs is relevant to human tissue-resident MCs, we first reanalyzed published cap analysis of gene expression (CAGE) data on human skin-derived MCs (Motakis et al., 2014). Although the comparison is limited by the different methods used for transcriptomics (CAGE versus RNA-seq), we examined the expression of genes harboring top-100 enhancers and broad H3K4me3 domains identified in our datasets. Almost all genes harboring top-100 enhancers (98 of 100) (Figure 6A) and broad H3K4me3 domains (97 of 100) (Figure 6B) were highly expressed in both peripheral-blood-derived and skin-derived human MCs (CPM > 20 in both datasets), suggesting a positive correlation between two different MC types (Table S5). In addition, when genes expressed in common were analyzed (CPM > 1 in both datasets), we still observed a high level of overlap (90%) (Figure 6C; Table S5). To further investigate the utility of our datasets obtained in peripheral-blood-derived human MCs, we next performed Omni-ATAC-seq using human tonsillar MCs isolated with

(B) FGL2 mRNA expression analysis in untreated, IgE-sensitized, and IgE+anti-IgE-treated MCs using RT-qPCR. Results are from four independent biological replicates; $p < 0.001$. Error bars are mean ± SD.

(C) FGL2 ELISA analysis using supernatants of untreated, IgE-sensitized, and IgE+anti-IgE-treated MCs. Results are from four biological replicates; $p < 0.05$. Error bars are mean ± SD.

(D) Representative confocal microscopy images of FGL2 and tryptase foci in lesional CSU skin biopsy samples. Scale bars are 20 microns.

(E) Representative confocal microscopy images of FGL2 and tryptase foci in non-lesional CSU skin biopsy samples. Scale bars are 20 μm.

(F) Quantification of percentage of MCs colocalizing with FGL2 foci in lesional and non-lesional CSU skin biopsies; n = 4 independent patient samples, $p < 0.01$. Error bars are mean ± SD.

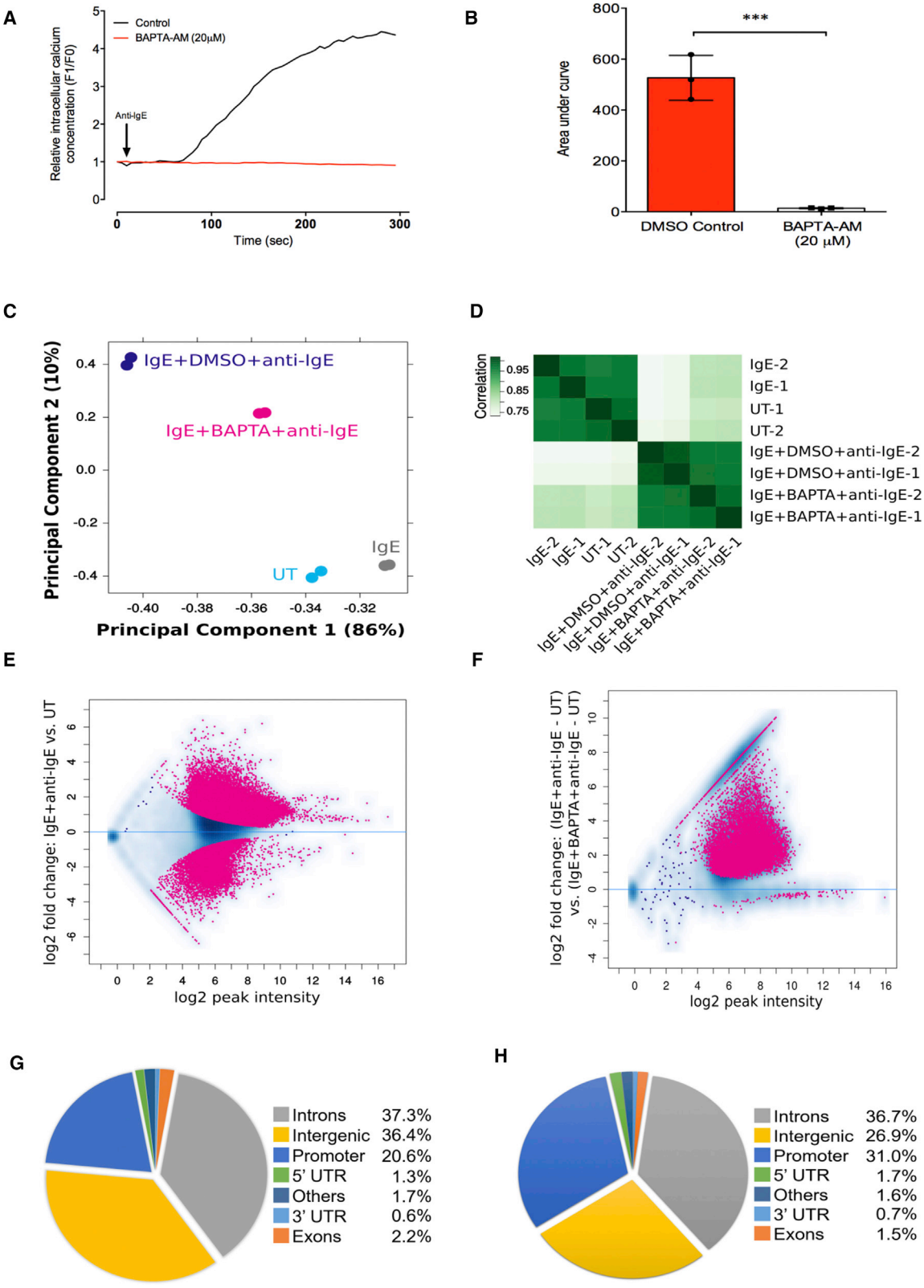


Figure 4. Identification of Ca^{2+}-Dependent Open Chromatin (COC) Domains Induced upon FcεRI Crosslinking

(A) Measurement of intracellular calcium levels using Fluo-3 AM in IgE+DMSO+anti-IgE- versus IgE+BAPTA-AM+anti-IgE-treated MCs. Data are from a representative experiment from three biological replicates.

(legend continued on next page)

CD117 (C-kit) magnetic beads and FcεRI-antibody-mediated sorting (Figures S5A and S5B). Tonsillar MC abundance was highly variable in each donor (Figure S5C). However, we managed to obtain enough MCs from two donors to perform Omni-ATAC-seq. Because the FcεRI antibody clone used for sorting (clone CRA1) also activates human MCs (Motakis et al., 2014), we immediately performed Omni-ATAC-seq on sorted cells. In both biological replicates, we identified Omni-ATAC-seq peaks in histidine decarboxylase (HDC) and tryptase (TPSAB1) gene loci critical for MCs (Figure S5C). We observed a large degree of overlap in Omni-ATAC-seq peaks (95,336 of 113,446) (84%) between IgE+anti-IgE-activated peripheral-blood-derived MCs and isolated tonsillar MCs (Figure 6D). Selected loci in IL1RL1 and SIGLEC6 genes, which are highly expressed in MCs (Figures 6E and 6F), and in CXCL8 (IL8) and CSF2 genes, which display increased expression upon MC activation, are shown for comparison (Figures S5D and S5E). We also investigated the genomic regions of top human MC enhancers and genomic regions of FGL2 and CLCF1 and observed largely coherent Omni-ATAC-seq peaks in tonsillar MCs (Figure S6).

Mapping Disease-Associated SNPs onto Human MC Chromatin Regions

There is extensive genetic variation (84.7 million SNPs) in the human genome as determined by the 1,000 Genomes Project (Auton et al., 2015). Thousands of SNPs are causally associated with the disease heterogeneity or disease prognosis (Lee et al., 2013, 2017). SNPs are also crucial in allergic diseases, which are notoriously heterogeneous in the population (Ferreira et al., 2017). However, despite the critical functions of MCs in allergic, inflammatory, and autoimmune diseases, the locations of disease-associated SNPs in human MC chromatin are largely uncharacterized. Therefore, to gain insights into the association of human MC chromatin and disease-associated SNPs, we extracted 2,049 non-human leukocyte antigen (HLA) SNPs with genome-wide significance ($p \leq 5.0 \times 10^{-8}$) from 30 autoimmune, inflammatory, and allergic disease traits using the National Human Genome Research Institute-European Bioinformatics Institute (NHGRI-EBI) catalog of published genome-wide association studies (GWASs) (MacArthur et al., 2017) (Figures 7A and 7B) and overlaid these SNPs on to our Omni-ATAC-seq, H3K27ac ChIP-seq, and H3K4me3 ChIP-seq datasets (Table S6). We next identified SNPs located precisely in Omni-ATAC-seq peaks of tonsillar MCs (Figure 7C). High-dimensional network analysis suggested that genes harboring these disease-associated SNPs located in Omni-ATAC-seq peaks of tonsillar MCs cooperate with each other in several biological processes (Figure S7). For further analysis, we also included flanking regions of these Omni-ATAC-seq peaks (500 bp upstream and 500 bp downstream) due to the fact that peak boundaries may not be well defined or vary among individuals (Finucane et al., 2015). We observed that each disease trait has a different percentage of SNPs located in Omni-ATAC-seq peaks and in flanking regions of these peaks (Figure 7D). For instance, certain diseases such as allergic rhinitis, ulcerative colitis, and IBD have higher percentages of SNPs in open chromatin regions of human tonsillar MCs (Figure 7D), suggesting a more active involvement of these SNPs in regulating MC functions in these diseases. On the other hand, disorders such as stroke or restless leg sydnrome had the lowest percentage of SNPs in the same Omni-ATAC-seq peaks (Figure 7D). Furthermore, we also identified disease-associated SNPs precisely located in COC domains (Table S6), which could provide important clues about intracellular calcium levels and regulation of gene expression in different diseases. Certain SNPs are located in regulatory chromatin regions of both peripheral-blood-derived and tonsillar MCs. For instance, rs17293632 is an intronic variant in SMAD3 gene loci and is associated with many diseases including asthma, IBD, Crohn's disease, and ulcerative colitis (de Lange et al., 2017; Demenais et al., 2018). rs17293632 is located both in H3K27ac ChIP-seq peaks and Omni-ATAC-seq peaks of peripheral-blood-derived and tonsillar MCs (Figure 7E), suggesting an active involvement of rs17293632 to regulate MC functions. It is important to further investigate the role of this and other SNPs located in regulatory regions of human MCs. Overall, it is conceivable that in a disease state, SNPs could be involved in complex alterations in chromatin landscape to fine-tune gene expression (Smemo et al., 2014).

DISCUSSION

MCs are located in close proximity to blood vessels and nerves in many tissues and express a diverse array of receptors to rapidly respond to extracellular cues (Cildir et al., 2017). The current understanding of the roles of MCs in different disease

(B) Area under the curve (AUC) analysis of intracellular calcium levels in (A). Data are from three independent biological replicates; $p < 0.001$. Error bars are mean ± SD.

(C) Principal-component analysis (PCA) of Omni-ATAC-seq peaks using biological replicates in each condition. The closer the replicates, the stronger the similarity between them. Data are from two independent biological replicates.

(D) Clustering and correlation analysis of biological replicates in Omni-ATAC-seq datasets. The stronger chromatin similarity between different conditions is associated with darker green color in chart. Data are from two independent biological replicates.

(E) Differential Omni-ATAC-seq peaks were identified in untreated versus IgE+anti-IgE-treated human MCs using $\log_2$ peak-intensity (x axis) versus $\log_2$ fold-change (y axis) analyses. Unique Omni-ATAC-seq peaks differentially opening upon IgE+anti-IgE treatment were indicated in pink color. Data are from two independent biological replicates.

(F) Differential Omni-ATAC-seq peaks were identified in IgE+DMSO+anti-IgE-treated versus IgE+BAPTA-AM+anti-IgE-treated human MCs using log peak-intensity (x axis) versus log fold-change (y-xis) analyses. Unique Omni-ATAC-seq peaks differentially opening in these two conditions were indicated in pink color. Data are from two independent biological replicates.

(G) Pie chart showing the genomic locations of differential Omni-ATAC-seq peaks in untreated versus IgE+anti-IgE-treated human MCs. Data are from two independent biological replicates.

(H) Pie chart showing the genomic locations of differential Omni-ATAC-seq peaks in IgE+DMSO+anti-IgE-treated versus IgE+BAPTA-AM+anti-IgE-treated human MCs. Data are from two independent biological replicates.

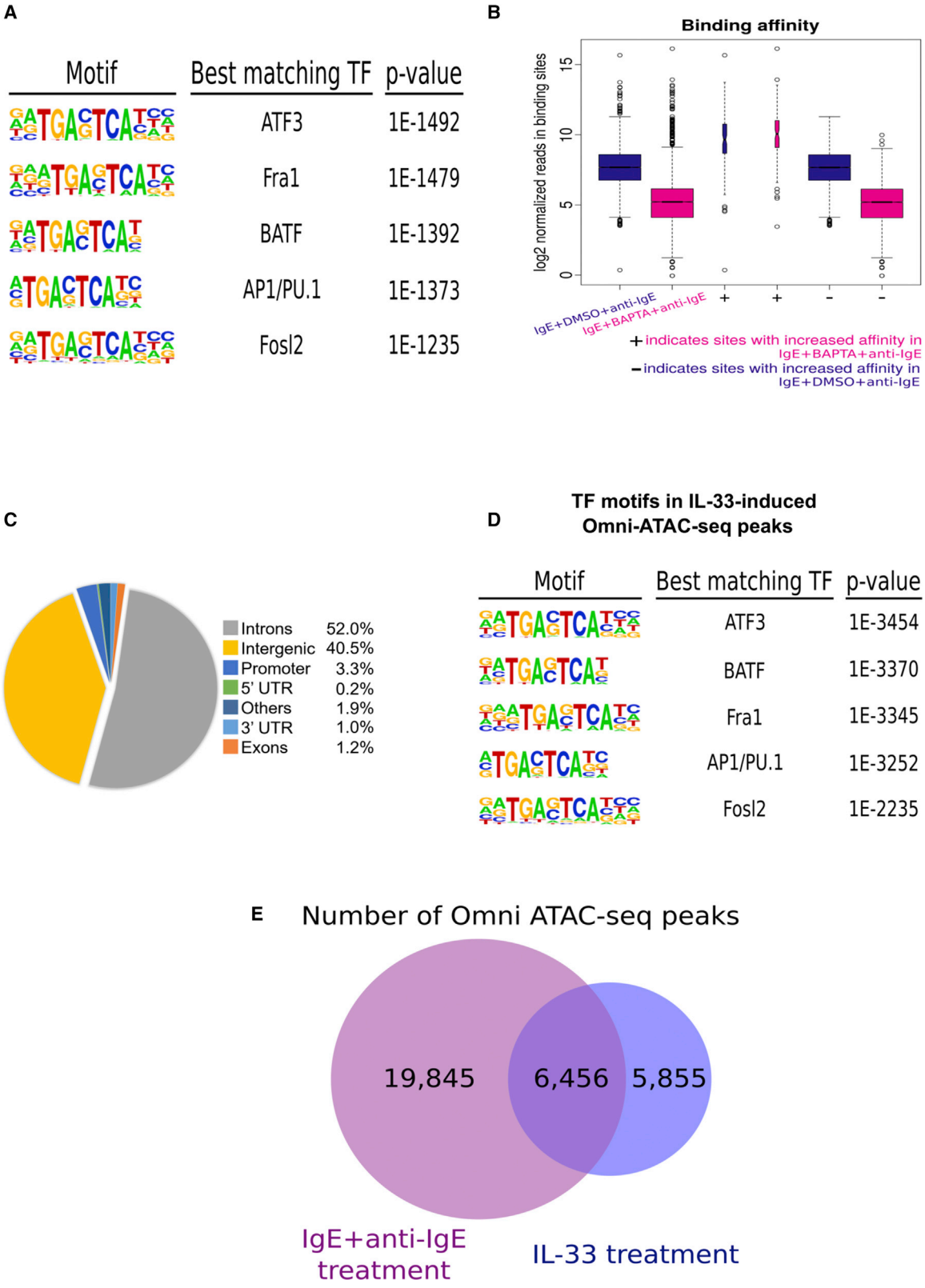


Figure 5. Comparison of the Chromatin Remodeling upon FcεRI Crosslinking and IL-33 Stimulation

(A) TF motif analysis by Hypergeometric Optimization of Motif EnRichment (HOMER) to identify significantly enriched TF motifs in COC domains of human MCs upon FcεRI crosslinking. Data are from two independent biological replicates.

(legend continued on next page)

contexts is largely based on studies in mouse models. The study of human MCs is difficult due to challenges associated with the isolation of sufficient numbers of highly pure and functional MCs from clinical samples. In addition, MC isolation methods based on mechanical tissue dissociation, enzymatic digestion, magnetic cell separation, and sorting impair the functional capacity of MCs (Lorentz et al., 2015). Here, we characterized the chromatin landscape of peripheral-blood-derived primary human MCs, observed genome-wide chromatin remodeling upon FcεRI crosslinking or IL-33 stimulation, and identified broad H3K4me3 domains and enhancers associated with MC activation. Analyses of CAGE data from human skin-derived MCs and Omni-ATAC-seq from *de novo* isolated tonsillar MCs suggest that the genomic changes observed in peripheral-blood-derived MCs upon activation reflect those occurring in tissue-resident MCs. Thus, these datasets present a resource for the identification of regulators of MC function in health and disease. We provide evidence for one such mediator, FGL2. FGL2 secretion was significantly increased upon FcεRI crosslinking in human MCs, and its expression was also increased in lesional skin samples of CSU patients.

Expression profiling of MCs from different mouse tissues provides important insights into the plasticity and diversity of the MC transcriptome (Dwyer et al., 2016). Mouse MCs in different organs share a conserved transcriptional signature, as well as a tissue-specific transcriptional profile likely dictated by the local tissue microenvironment (Dwyer et al., 2016). For instance, mouse MCs from esophagus, tongue, and trachea show a similar transcriptional profile, which is distinct from the peritoneal MCs. Skin and peritoneal MCs are the most distinct subtypes compared with the other constitutive MCs (Dwyer et al., 2016). However, the regulation of tissue-specific transcriptional changes remains elusive. It is also unclear whether different tissue-resident MCs respond differently to the same activating stimuli such as IgE or IL-33. Because data on external stimulation and chromatin reorganization of MCs are not reported in the study by Dwyer et al. (2016), we were unable to compare our results with them. Transcriptional profiling of human skin-derived MCs also provides critical insights into MC activation (Motakis et al., 2014). MCs are distinct from all the other immune cells, and upon expansion in culture and activation with FcεRI crosslinking, human skin-derived MCs show a differential transcriptional response (Motakis et al., 2014). We observed that genes associated with top enhancers and broad H3K4me3 domains in peripheral-blood-derived MCs also have high expression levels in skin-derived MCs. Because data on activation-induced genome-wide chromatin reorganization are not reported in the study by Motakis et al. (2014), we were unable to compare chromatin reorganization between skin-derived human MCs and peripheral-blood-derived MCs. However, our comparison of the chromatin state of peripheral-blood-derived MCs upon FcεRI crosslinking with *de novo* isolated tonsillar MCs showed a high degree of correlation in open chromatin regions. It is likely that the already existing inflammation in tonsils, mechanical dissociation and enzymatic digestion of tonsillar tissue, and isolation of MCs with magnetic beads and FcεRI-based sorting each contributed to an activated state of chromatin in tonsillar MCs.

Immune cells reorganize specific chromatin regions upon different danger signals. Human macrophages, for example, employ a complex interferon (IFN)-γ-mediated enhancer reorganization involving repression, activation, and differential TF binding (Kang et al., 2017). Similarly, stimulation of mouse bone-marrow-derived macrophages with lipopolysaccharide (LPS) leads to remodeling of distinct classes of enhancers (Ostuni et al., 2013). However, involvement of calcium in genome-wide enhancer reorganization in these contexts is unclear. One of the important findings from this study was the regulation of chromatin landscape after FcεRI crosslinking by intracellular calcium levels in human MCs. Intracellular calcium levels are tightly controlled and could be elevated in certain cell types upon stimulation. In T cells, for instance, T cell receptor (TCR) activation triggers a calcium response mediated by store-operated calcium channels, crucial for antigen-dependent T cell proliferation (Vaeth et al., 2017). In MCs, although increased intracellular calcium levels are not critical for microtubule dynamics, they are required for granule exocytosis upon FcεRI crosslinking (Nishida et al., 2005). In addition, calcium is critical for the activation of NFAT and NF-κB pathways (Cildir et al., 2017), but the role of intracellular calcium in genome-wide chromatin reorganization of human MCs is unexplored. Our identification of COC domains suggested that increased levels of calcium are crucial not only for orchestrating the release of the preformed granules, but also for defining the landscape of the chromatin upon FcεRI crosslinking. Notably, we observed that nearly 20% of COC domains are also shared with IL-33 stimulation. Because different extracellular stimuli have secondary biological effects after stimulation, which happens in minutes to hours and could be common for many stimuli, these secondary events are possibly the major contributors to these 20% common regions.

Recent fate-mapping studies in mice suggest that MCs have dual developmental origin (Gentek et al., 2018) and show preferences for different tissue locations depending on their origin (Li et al., 2018). Mucosal MCs (MMCs), such as certain populations of MCs located in the gut, are derived from the fetal HSC-derived cells and are renewed by the bone marrow. In contrast, adult connective-tissue MCs (CTMCs), such as skin-resident MCs, are mainly derived from yolk-sac late-erythro-myeloid progenitors (EMPs) and are self-maintained independently of HSCs (Li et al., 2018). Further studies in the human system are needed to better understand the developmental origin of different tissue-resident human MCs (Grootens et al., 2018).

(B) Peak analysis by HOMER for identified TF binding sites in (A). Data are from two independent biological replicates.
(C) Pie chart showing the genomic locations of Omni-ATAC-seq peaks differentially regulated upon IL-33 treatment. Data are from two independent biological replicates.
(D) TF motif analysis by HOMER to identify significantly enriched TF motifs in Omni-ATAC-seq peaks differentially open upon IL-33 treatment. Data are from two independent biological replicates.
(E) Venn-diagram comparison of Omni-ATAC-seq peaks upon IL-33 stimulaion for 2 h or IgE+anti-IgE stimulation for 2 h (Omni-ATAC-seq peaks in untreated samples were used as background). Data are from two independent biological replicates.

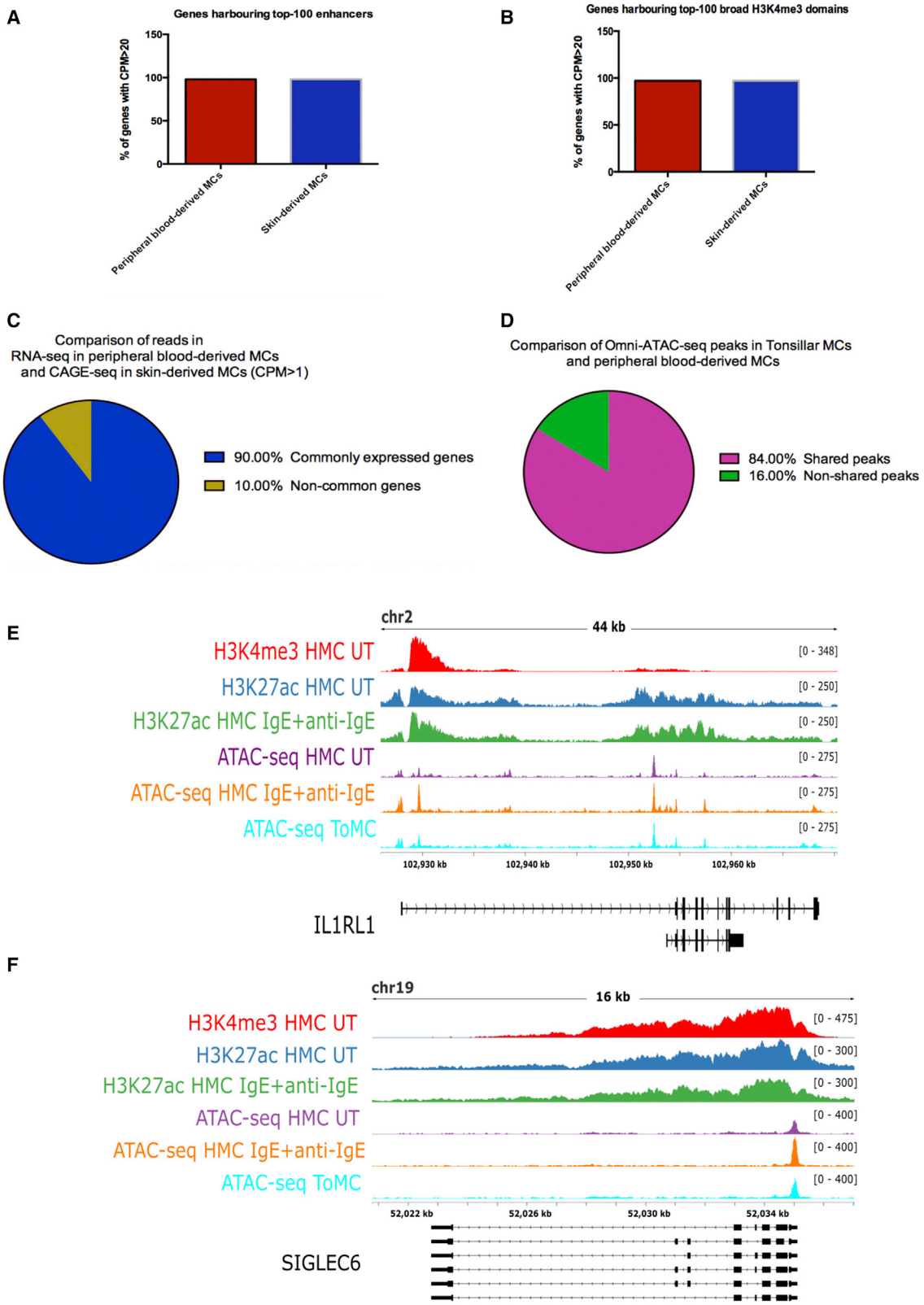


Figure 6. Epigenomic and Transcriptomic Comparison of Peripheral-Blood-Derived Human MCs with Skin-Derived and Tonsillar MCs

(A) Comparison of the expression of genes harboring top-100 enhancers (CPM > 20) in both peripheral-blood-derived and skin-derived MCs (CAGE data were extracted from public databases).

(legend continued on next page)

In our study, we used human MCs derived from the blood progenitors and tonsils to characterize the genome-wide chromatin landscape, and therefore, we note that our findings may be limited to human MCs derived from the bone marrow progenitors. Whether the chromatin response of CTMCs and MMCs to external stimuli could significantly differ remains to be explored.

The relationship between disease-associated variants and regulatory chromatin regions of immune cells is being increasingly appreciated (Farh et al., 2015). GWAS variants are linked to the immune cells where their effects are most pronounced (Schmiedel et al., 2018). Our GWAS analyses of 30 different inflammatory and autoimmune disease traits identified numerous SNPs located in H3K27ac+ chromatin regions and Omni-ATAC-seq peaks in human MCs, suggesting active involvement of these SNPs in regulating epigenome and transcriptome. As expected, a high percentage of SNPs associated with the allergic rhinitis and the trait of ''shared asthma, hay fever, and eczema'' are located in *cis*-regulatory regions of MCs. The roles of MCs in these allergic diseases are well accepted. Our data also suggest the involvement of MCs in other inflammatory and autoimmune diseases (Brown and Hatfield, 2012; Siebenhaar et al., 2018). Further investigation of MCs on disease settings such as Behcet's disease, tuberculosis, ulcerative colitis, and systemic lupus will be required to validate previous reports (Brown and Hatfield, 2012; Garcia-Rodriguez et al., 2017; Hamilton et al., 2014; Lichtig et al., 1981).

Our chromatin-profiling-based approach identified several candidate genes that could be further studied. For instance, we identified the BHLHE40 enhancer region as one of the top candidates in human MCs. BHLHE40 is a repressor of IL-10 production during *Mycobacterium tuberculosis* infection (Huynh et al., 2018) and also regulates cytokine production in T cells in autoimmune diseases (Lin et al., 2014). Therefore, the roles of BHLHE40 in human MCs should be further deciphered in the context of inflammatory diseases. Similarly, further research on genes associated with top enhancers such as BMP2 Inducible Kinase (BMP2K) or Rho GTPase Activating Protein 18 (ARHGAP18) is required. To investigate some of the identified candidate genes, we focused on FGL2. MCs release numerous soluble mediators, including proteases, growth factors, cytokines, and chemokines (Shubin et al., 2017). Our screen identified FGL2, which in its soluble form is mainly linked to Tregs and has suppressor activities against Th1 and Th17 cells, but not against Th2 cells (Joller et al., 2014). Given the well-established role of the Th2-high microenvironment in allergic diseases, it is tempting to speculate that FGL2 plays an important role in the context of allergic diseases.

Overall, chromatin regions reorganized upon activation and associated with disease variants, genes interacting with human MC enhancers, and broad H3K4me3 domains provide crucial links between MC biology and common diseases. Therefore, our study provides an important framework for understanding the role of chromatin reorganization in human MCs and serves as a useful resource to further explore the roles of MCs in human physiology and disease.

STAR★METHODS

Detailed methods are provided in the online version of this paper and include the following:

- KEY RESOURCES TABLE
- LEAD CONTACT AND MATERIALS AVAILABILITY
- EXPERIMENTAL MODEL AND SUBJECT DETAILS
- METHOD DETAILS
  - Peripheral blood-derived MCs
  - Isolation of tonsillar MCs
  - Flow cytometric analysis
  - ELISA
  - CSU skin biopsy samples and confocal microscopy
  - Calcium mobilization study
  - CHIP and CHIP-seq
  - Omni-ATAC-seq
  - RNA isolation and RNA-seq
  - GWAS analysis
  - Bioinformatics analysis of CHIP-seq data
  - Bioinformatics analysis of Omni-ATAC-seq data
  - Bioinformatics analysis of RNA-seq data
- QUANTIFICATION AND STATISTICAL ANALYSIS
- DATA AND CODE AVAILABILITY

SUPPLEMENTAL INFORMATION

Supplemental Information can be found online at https://doi.org/10.1016/j.immuni.2019.09.021.

ACKNOWLEDGMENTS

We thank Tim Hercus and Frank Stomski for assistance and Zbigniew Adam Opala for the cover art. We gratefully acknowledge funding provided by the Agency for Science, Technology, and Research (A*STAR) of Singapore through Institute of Molecular and Cell Biology (IMCB) core fund NFR-CRP17-2017-02; the National Health and Medical Research Council (NHMRC) of Australia through program grant 105253; and the Premier's Research and Industry Fund grant provided by the South Australian Government Department of State Development.

AUTHOR CONTRIBUTIONS

G.C. performed all ChIP-seq, RNA-seq, Omni-ATAC-seq, and confocal microscopy experiments and wrote the manuscript. J.T. and J.Z. performed all bioinformatics analyses. K.H.Y. generated human peripheral-blood-derived MCs

(B) Comparison of the expression of top-100 broad H3K4me3 domain-harboring genes (CPM > 20) in both peripheral-blood-derived and skin-derived MCs.
(C) Pie chart for the comparison of the overlap of expressed genes (CPM > 1) in both peripheral-blood-derived and skin-derived MCs.
(D) Pie chart for the comparison of the overlap of Omni-ATAC-seq peaks in peripheral-blood-derived and tonsillar MCs. Data are from two independent biological replicates.
(E) Integrative Genomics Viewer (IGV) tracks of H3K4me3 and H3K27ac ChIP-seq, Omni-ATAC-seq datasets from peripheral-blood-derived MCs, and Omni-ATAC-seq datasets from tonsillar MCs in human IL1RL1 gene loci. Data are from two independent biological replicates.
(F) IGV tracks of H3K4me3 and H3K27ac ChIP-seq, Omni-ATAC-seq datasets from peripheral-blood-derived MCs, and Omni-ATAC-seq datasets from tonsillar MCs in human SIGLEC6 gene loci. Data are from two independent biological replicates.

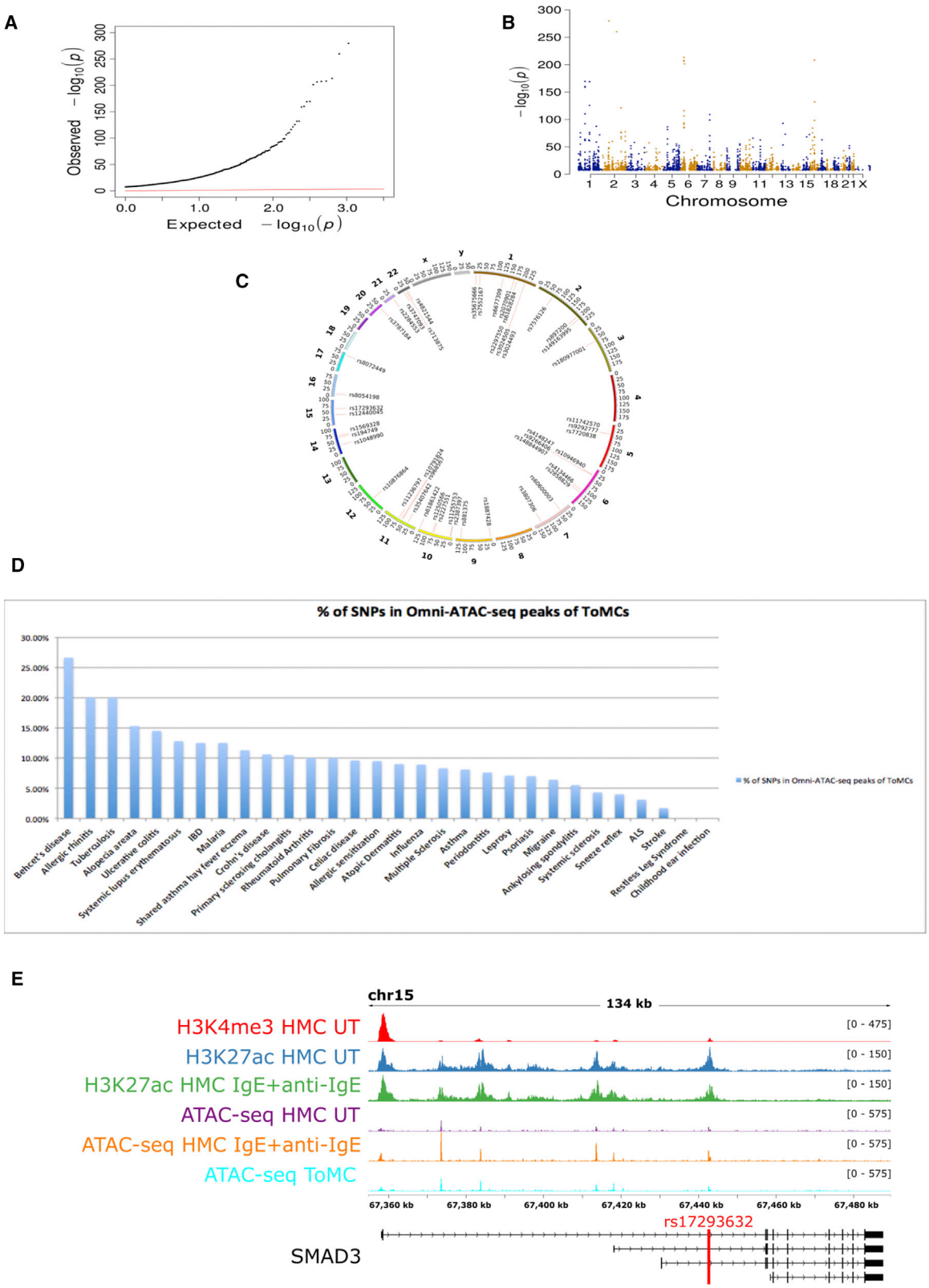


Figure 7. Analysis of Disease-Associated SNPs Located in Regulatory Regions of Human MCs

(A) Q-Q plot analysis of "expected" and "observed" distribution of p values from 2,049 disease-associated non-HLA SNPs with genome-wide significance ($p \leq 5.0 \times 10^{-8}$) extracted from NHGRI-EBI GWAS catalog. The x axis shows expected $-\log_{10}$ (p value) of all SNPs in this study, and the y axis shows the

(legend continued on next page)

for ChIP-seq experiments and performed calcium measurement experiments. M.Z. prepared CSU skin biopsy samples. H.P. provided tonsil samples. P.H. provided CSU skin biopsy samples. N.R., M.A.G., A.F.L., and W.H. provided intellectual input. V.T. supervised the project.

DECLARATION OF INTERESTS

The authors declare no competing interests.

Received: February 28, 2018
Revised: February 18, 2019
Accepted: September 25, 2019
Published: October 22, 2019

REFERENCES

Andrade, M.V., Iwaki, S., Ropert, C., Gazzinelli, R.T., Cunha-Melo, J.R., and Beaven, M.A. (2011). Amplification of cytokine production through synergistic activation of NFAT and AP-1 following stimulation of mast cells with antigen and IL-33. Eur. J. Immunol. *41*, 760–772.

Auton, A., Brooks, L.D., Durbin, R.M., Garrison, E.P., Kang, H.M., Korbel, J.O., Marchini, J.L., McCarthy, S., McVean, G.A., and Abecasis, G.R.; 1000 Genomes Project Consortium (2015). A global reference for human genetic variation. Nature *526*, 68–74.

Ball, D.H., Al-Riyami, L., Harnett, W., and Harnett, M.M. (2018). IL-33/ST2 signalling and crosstalk with FcεRI and TLR4 is targeted by the parasitic worm product, ES-62. Sci. Rep. *8*, 4497.

Barbu, E.A., Zhang, J., Berenstein, E.H., Groves, J.R., Parks, L.M., and Siraganian, R.P. (2012). The transcription factor Zeb2 regulates signaling in mast cells. J. Immunol. *188*, 6278–6286.

Benayoun, B.A., Pollina, E.A., Ucar, D., Mahmoudi, S., Karra, K., Wong, E.D., Devarajan, K., Daugherty, A.C., Kundaje, A.B., Mancini, E., et al. (2014). H3K4me3 breadth is linked to cell identity and transcriptional consistency. Cell *158*, 673–688.

Beyaz, S., Kim, J.H., Pinello, L., Xifaras, M.E., Hu, Y., Huang, J., Kerenyi, M.A., Das, P.P., Barnitz, R.A., Herault, A., et al. (2017). The histone demethylase UTX regulates the lineage-specific epigenetic program of invariant natural killer T cells. Nat. Immunol. *18*, 184–195.

Blank, U., Madera-Salcedo, I.K., Danelli, L., Claver, J., Tiwari, N., Sánchez-Miranda, E., Vázquez-Victorio, G., Ramírez-Valadez, K.A., Macias-Silva, M., and González-Espinosa, C. (2014). Vesicular trafficking and signaling for cytokine and chemokine secretion in mast cells. Front. Immunol. *5*, 453.

Brown, M.A., and Hatfield, J.K. (2012). Mast Cells are Important Modifiers of Autoimmune Disease: With so Much Evidence, Why is There Still Controversy? Front. Immunol. *3*, 147.

Bunting, K.L., Soong, T.D., Singh, R., Jiang, Y., Béguelin, W., Poloway, D.W., Swed, B.L., Hatzi, K., Reisacher, W., Teater, M., et al. (2016). Multi-tiered Reorganization of the Genome during B Cell Affinity Maturation Anchored by a Germinal Center-Specific Locus Control Region. Immunity *45*, 497–512.

Calo, E., and Wysocka, J. (2013). Modification of enhancer chromatin: what, how, and why? Mol. Cell *49*, 825–837.

Cayrol, C., and Girard, J.P. (2018). Interleukin-33 (IL-33): A nuclear cytokine from the IL-1 family. Immunol. Rev. *281*, 154–168.

Chen, K., Chen, Z., Wu, D., Zhang, L., Lin, X., Su, J., Rodriguez, B., Xi, Y., Xia, Z., Chen, X., et al. (2015). Broad H3K4me3 is associated with increased transcription elongation and enhancer activity at tumor-suppressor genes. Nat. Genet. *47*, 1149–1157.

Cildir, G., Pant, H., Lopez, A.F., and Tergaonkar, V. (2017). The transcriptional program, functional heterogeneity, and clinical targeting of mast cells. J. Exp. Med. *214*, 2491–2506.

Corces, M.R., Trevino, A.E., Hamilton, E.G., Greenside, P.G., Sinnott-Armstrong, N.A., Vesuna, S., Satpathy, A.T., Rubin, A.J., Montine, K.S., Wu, B., et al. (2017). An improved ATAC-seq protocol reduces background and enables interrogation of frozen tissues. Nat. Methods *14*, 959–962.

Creyghton, M.P., Cheng, A.W., Welstead, G.G., Kooistra, T., Carey, B.W., Steine, E.J., Hanna, J., Lodato, M.A., Frampton, G.M., Sharp, P.A., et al. (2010). Histone H3K27ac separates active from poised enhancers and predicts developmental state. Proc. Natl. Acad. Sci. USA *107*, 21931–21936.

Dahl, J.A., Jung, I., Aanes, H., Greggains, G.D., Manaf, A., Lerdrup, M., Li, G., Kuan, S., Li, B., Lee, A.Y., et al. (2016). Broad histone H3K4me3 domains in mouse oocytes modulate maternal-to-zygotic transition. Nature *537*, 548–552.

Davis, C.A., Hitz, B.C., Sloan, C.A., Chan, E.T., Davidson, J.M., Gabdank, I., Hilton, J.A., Jain, K., Baymuradov, U.K., Narayanan, A.K., et al. (2017). The Encyclopedia of DNA elements (ENCODE): data portal update (Nucleic Acids Res).

de Kleer, I.M., Kool, M., de Bruijn, M.J., Willart, M., van Moorleghem, J., Schuijs, M.J., Plantinga, M., Beyaert, R., Hams, E., Fallon, P.G., et al. (2016). Perinatal Activation of the Interleukin-33 Pathway Promotes Type 2 Immunity in the Developing Lung. Immunity *45*, 1285–1298.

de Lange, K.M., Moutsianas, L., Lee, J.C., Lamb, C.A., Luo, Y., Kennedy, N.A., Jostins, L., Rice, D.L., Gutierrez-Achury, J., Ji, S.G., et al. (2017). Genome-wide association study implicates immune activation of multiple integrin genes in inflammatory bowel disease. Nat. Genet. *49*, 256–261.

Demenais, F., Margaritte-Jeannin, P., Barnes, K.C., Cookson, W.O.C., Altmüller, J., Ang, W., Barr, R.G., Beaty, T.H., Becker, A.B., Beilby, J., et al.; Australian Asthma Genetics Consortium (AAGC) collaborators (2018). Multiancestry association study identifies new asthma risk loci that colocalize with immune-cell enhancer marks. Nat. Genet. *50*, 42–53.

Dhar, S.S., Zhao, D., Lin, T., Gu, B., Pal, K., Wu, S.J., Alam, H., Lv, J., Yun, K., Gopalakrishnan, V., et al. (2018). MLL4 Is Required to Maintain Broad H3K4me3 Peaks and Super-Enhancers at Tumor Suppressor Genes. Mol. Cell *70*, 825–841.

Dobin, A., Davis, C.A., Schlesinger, F., Drenkow, J., Zaleski, C., Jha, S., Batut, P., Chaisson, M., and Gingeras, T.R. (2013). STAR: ultrafast universal RNA-seq aligner. Bioinformatics *29*, 15–21.

Dong, X., Ye, X., Chen, X., Chen, T., Xie, S., Li, Q., Lin, X., and Huang, Z. (2014). Intestinal and peripheral fibrinogen-like protein 2 expression in inflammatory bowel disease. Dig. Dis. Sci. *59*, 769–777.

Dwyer, D.F., Barrett, N.A., and Austen, K.F.; Immunological Genome Project Consortium (2016). Expression profiling of constitutive mast cells reveals a unique identity within the immune system. Nat. Immunol. *17*, 878–887.

Farh, K.K., Marson, A., Zhu, J., Kleinewietfeld, M., Housley, W.J., Beik, S., Shoresh, N., Whitton, H., Ryan, R.J., Shishkin, A.A., et al. (2015). Genetic and epigenetic fine mapping of causal autoimmune disease variants. Nature *518*, 337–343.

observed $-\log_{10}$ (p value) of all SNPs in this study. Deviation from x = y line (red line) indicates a highly significant genome-wide association for SNPs, and each black point indicates a unique SNP deviating from x = y line.

(B) Manhattan plot showing the chromosomal distribution of all SNPs used in this study. The x axis shows the chromosome numbers, and the y axis shows $-\log_{10}$ (p value) of all SNPs in this study. Each blue and yellow point represents a unique SNP.

(C) CIRCOS plot representation of SNPs with genome-wide significance ($p \leq 5.0 \times 10^{-8}$) located in Omni-ATAC-seq peaks of tonsillar MCs. SNP locations were indicated in each chromosome.

(D) Percentages of disease-associated SNPs with genome-wide significance ($p \leq 5.0 \times 10^{-8}$) located in Omni-ATAC-seq peaks and in flanking regions (±500 bp of Omni-ATAC-seq peaks) of human tonsillar MCs were indicated in 30 different disease traits.

(E) IGV tracks of H3K4me3 and H3K27ac ChIP-seq, Omni-ATAC-seq datasets from peripheral blood-derived MCs, and Omni-ATAC-seq datasets from tonsillar MCs in human SMAD3 genomic loci harboring SNP rs17293632.

Ferreira, M.A., Vonk, J.M., Baurecht, H., Marenholz, I., Tian, C., Hoffman, J.D., Helmer, Q., Tillander, A., Ullemar, V., van Dongen, J., et al.; 23andMe Research Team; AAGC collaborators; BIOS consortium; LifeLines Cohort Study (2017). Shared genetic origin of asthma, hay fever and eczema elucidates allergic disease biology. Nat. Genet. *49*, 1752–1757.

Finucane, H.K., Bulik-Sullivan, B., Gusev, A., Trynka, G., Reshef, Y., Loh, P.R., Anttila, V., Xu, H., Zang, C., Farh, K., et al.; ReproGen Consortium; Schizophrenia Working Group of the Psychiatric Genomics Consortium; RACI Consortium (2015). Partitioning heritability by functional annotation using genome-wide association summary statistics. Nat. Genet. *47*, 1228–1235.

Galli, S.J., and Tsai, M. (2012). IgE and mast cells in allergic disease. Nat. Med. *18*, 693–704.

Garcia-Rodriguez, K.M., Goenka, A., Alonso-Rasgado, M.T., Hernández-Pando, R., and Bulfone-Paus, S. (2017). The Role of Mast Cells in Tuberculosis: Orchestrating Innate Immune Crosstalk? Front. Immunol. *8*, 1290.

Gentek, R., Ghigo, C., Hoeffel, G., Bulle, M.J., Msallam, R., Gautier, G., Launay, P., Chen, J., Ginhoux, F., and Bajénoff, M. (2018). Hemogenic Endothelial Fate Mapping Reveals Dual Developmental Origin of Mast Cells. Immunity *48*, 1160–1171.

Gilchrist, M., Henderson, W.R., Jr., Morotti, A., Johnson, C.D., Nachman, A., Schmitz, F., Smith, K.D., and Aderem, A. (2010). A key role for ATF3 in regulating mast cell survival and mediator release. Blood *115*, 4734–4741.

Grootens, J., Ungerstedt, J.S., Nilsson, G., and Dahlin, J.S. (2018). Deciphering the differentiation trajectory from hematopoietic stem cells to mast cells. Blood Adv. *2*, 2273–2281.

Hamilton, M.J., Frei, S.M., and Stevens, R.L. (2014). The multifaceted mast cell in inflammatory bowel disease. Inflamm. Bowel Dis. *20*, 2364–2378.

Heinz, S., Benner, C., Spann, N., Bertolino, E., Lin, Y.C., Laslo, P., Cheng, J.X., Murre, C., Singh, H., and Glass, C.K. (2010). Simple combinations of lineage-determining transcription factors prime cis-regulatory elements required for macrophage and B cell identities. Mol. Cell *38*, 576–589.

Hu, J., Yan, J., Rao, G., Latha, K., Overwijk, W.W., Heimberger, A.B., and Li, S. (2016). The Duality of Fgl2 - Secreted Immune Checkpoint Regulator Versus Membrane-Associated Procoagulant: Therapeutic Potential and Implications. Int. Rev. Immunol. *35*, 325–339.

Huang da, W., Sherman, B.T., and Lempicki, R.A. (2009). Bioinformatics enrichment tools: paths toward the comprehensive functional analysis of large gene lists. Nucleic Acids Res. *37*, 1–13.

Huynh, J.P., Lin, C.C., Kimmey, J.M., Jarjour, N.N., Schwarzkopf, E.A., Bradstreet, T.R., Shchukina, I., Shpynov, O., Weaver, C.T., Taneja, R., et al. (2018). Bhlhe40 is an essential repressor of IL-10 during *Mycobacterium tuberculosis* infection. J. Exp. Med. *215*, 1823–1838.

Janson, C., Kasahara, N., Prendergast, G.C., and Colicelli, J. (2012). RIN3 is a negative regulator of mast cell responses to SCF. PLoS ONE *7*, e49615.

Johnson, J.L., Georgakilas, G., Petrovic, J., Kurachi, M., Cai, S., Harly, C., Pear, W.S., Bhandoola, A., Wherry, E.J., and Vahedi, G. (2018). Lineage-Determining Transcription Factor TCF-1 Initiates the Epigenetic Identity of T Cells. Immunity *48*, 243–257.

Joller, N., Lozano, E., Burkett, P.R., Patel, B., Xiao, S., Zhu, C., Xia, J., Tan, T.G., Sefik, E., Yajnik, V., et al. (2014). Treg cells expressing the coinhibitory molecule TIGIT selectively inhibit proinflammatory Th1 and Th17 cell responses. Immunity *40*, 569–581.

Joulia, R., L'Faqihi, F.E., Valitutti, S., and Espinosa, E. (2017). IL-33 fine tunes mast cell degranulation and chemokine production at the single-cell level. J. Allergy Clin. Immunol. *140*, 497–509.

Jung, M.Y., Smrž, D., Desai, A., Bandara, G., Ito, T., Iwaki, S., Kang, J.H., Andrade, M.V., Hilderbrand, S.C., Brown, J.M., et al. (2013). IL-33 induces a hyporesponsive phenotype in human and mouse mast cells. J. Immunol. *190*, 531–538.

Kang, K., Park, S.H., Chen, J., Qiao, Y., Giannopoulou, E., Berg, K., Hanidu, A., Li, J., Nabozny, G., Kang, K., et al. (2017). Interferon-γ Represses M2 Gene Expression in Human Macrophages by Disassembling Enhancers Bound by the Transcription Factor MAF. Immunity *47*, 235–250.

Kundaje, A., Meuleman, W., Ernst, J., Bilenky, M., Yen, A., Heravi-Moussavi, A., Kheradpour, P., Zhang, Z., Wang, J., Ziller, M.J., et al.; Roadmap Epigenomics Consortium (2015). Integrative analysis of 111 reference human epigenomes. Nature *518*, 317–330.

Langmead, B., Trapnell, C., Pop, M., and Salzberg, S.L. (2009). Ultrafast and memory-efficient alignment of short DNA sequences to the human genome. Genome Biol. *10*, R25.

Lee, Y.N., Tuckerman, J., Nechushtan, H., Schutz, G., Razin, E., and Angel, P. (2004). c-Fos as a regulator of degranulation and cytokine production in FcepsilonRI-activated mast cells. J. Immunol. *173*, 2571–2577.

Lee, J.C., Espéli, M., Anderson, C.A., Linterman, M.A., Pocock, J.M., Williams, N.J., Roberts, R., Viatte, S., Fu, B., Peshu, N., et al.; UK IBD Genetics Consortium (2013). Human SNP links differential outcomes in inflammatory and infectious disease to a FOXO3-regulated pathway. Cell *155*, 57–69.

Lee, J.C., Biasci, D., Roberts, R., Gearry, R.B., Mansfield, J.C., Ahmad, T., Prescott, N.J., Satsangi, J., Wilson, D.C., Jostins, L., et al.; UK IBD Genetics Consortium (2017). Genome-wide association study identifies distinct genetic contributions to prognosis and susceptibility in Crohn's disease. Nat. Genet. *49*, 262–268.

Li, H., and Durbin, R. (2009). Fast and accurate short read alignment with Burrows-Wheeler transform. Bioinformatics *25*, 1754–1760.

Li, Z., Liu, S., Xu, J., Zhang, X., Han, D., Liu, J., Xia, M., Yi, L., Shen, Q., Xu, S., et al. (2018). Adult Connective Tissue-Resident Mast Cells Originate from Late Erythro-Myeloid Progenitors. Immunity *49*, 640–653.

Lichtig, C., Haim, S., Gilhar, A., Hammel, I., and Ludatscher, R. (1981). Mast cells in Behçet's disease: ultrastructural and histamine content studies. Dermatologica *162*, 167–174.

Lin, C.C., Bradstreet, T.R., Schwarzkopf, E.A., Sim, J., Carrero, J.A., Chou, C., Cook, L.E., Egawa, T., Taneja, R., Murphy, T.L., et al. (2014). Bhlhe40 controls cytokine production by T cells and is essential for pathogenicity in autoimmune neuroinflammation. Nat. Commun. *5*, 3551.

Long, H.K., Prescott, S.L., and Wysocka, J. (2016). Ever-Changing Landscapes: Transcriptional Enhancers in Development and Evolution. Cell *167*, 1170–1187.

Lorentz, A., Sellge, G., and Bischoff, S.C. (2015). Isolation and characterization of human intestinal mast cells. Methods Mol. Biol. *1220*, 163–177.

Lun, A.T., Chen, Y., and Smyth, G.K. (2016). It's DE-licious: A Recipe for Differential Expression Analyses of RNA-seq Experiments Using Quasi-Likelihood Methods in edgeR. Methods Mol. Biol. *1418*, 391–416.

Lyons, J.J., and Milner, J.D. (2018). Primary atopic disorders. J. Exp. Med. *215*, 1009–1022.

MacArthur, J., Bowler, E., Cerezo, M., Gil, L., Hall, P., Hastings, E., Junkins, H., McMahon, A., Milano, A., Morales, J., et al. (2017). The new NHGRI-EBI Catalog of published genome-wide association studies (GWAS Catalog). Nucleic Acids Res. *45* (D1), D896–D901.

McLean, C.Y., Bristor, D., Hiller, M., Clarke, S.L., Schaar, B.T., Lowe, C.B., Wenger, A.M., and Bejerano, G. (2010). GREAT improves functional interpretation of cis-regulatory regions. Nat. Biotechnol. *28*, 495–501.

McNeil, B.D., Pundir, P., Meeker, S., Han, L., Undem, B.J., Kulka, M., and Dong, X. (2015). Identification of a mast-cell-specific receptor crucial for pseudo-allergic drug reactions. Nature *519*, 237–241.

Mizuno, K., Tolmachova, T., Ushakov, D.S., Romao, M., Abrink, M., Ferenczi, M.A., Raposo, G., and Seabra, M.C. (2007). Rab27b regulates mast cell granule dynamics and secretion. Traffic *8*, 883–892.

Motakis, E., Guhl, S., Ishizu, Y., Itoh, M., Kawaji, H., de Hoon, M., Lassmann, T., Carninci, P., Hayashizaki, Y., Zuberbier, T., et al.; FANTOM consortium (2014). Redefinition of the human mast cell transcriptome by deep-CAGE sequencing. Blood *123*, e58–e67.

Nishida, K., Yamasaki, S., Ito, Y., Kabu, K., Hattori, K., Tezuka, T., Nishizumi, H., Kitamura, D., Goitsuka, R., Geha, R.S., et al. (2005). FcepsilonRI-mediated mast cell degranulation requires calcium-independent microtubule-dependent translocation of granules to the plasma membrane. J. Cell Biol. *170*, 115–126.

Ostuni, R., Piccolo, V., Barozzi, I., Polletti, S., Termanini, A., Bonifacio, S., Curina, A., Prosperini, E., Ghisletti, S., and Natoli, G. (2013). Latent enhancers activated by stimulation in differentiated cells. Cell *152*, 157–171.

Platts-Mills, T.A., and Woodfolk, J.A. (2011). Allergens and their role in the allergic immune response. Immunol. Rev. *242*, 51–68.

Ramírez, F., Ryan, D.P., Grüning, B., Bhardwaj, V., Kilpert, F., Richter, A.S., Heyne, S., Dündar, F., and Manke, T. (2016). deepTools2: a next generation web server for deep-sequencing data analysis. Nucleic Acids Res. *44* (W1), W160–W165.

Redegeld, F.A., Yu, Y., Kumari, S., Charles, N., and Blank, U. (2018). Non-IgE mediated mast cell activation. Immunol. Rev. *282*, 87–113.

Rickels, R., and Shilatifard, A. (2018). Enhancer Logic and Mechanics in Development and Disease. Trends Cell Biol. *28*, 608–630.

Robinson, M.D., McCarthy, D.J., and Smyth, G.K. (2010). edgeR: a Bioconductor package for differential expression analysis of digital gene expression data. Bioinformatics *26*, 139–140.

Rousseau, F., Gauchat, J.F., McLeod, J.G., Chevalier, S., Guillet, C., Guilhot, F., Cognet, I., Froger, J., Hahn, A.F., Knappskog, P.M., et al. (2006). Inactivation of cardiotrophin-like cytokine, a second ligand for ciliary neurotrophic factor receptor, leads to cold-induced sweating syndrome in a patient. Proc. Natl. Acad. Sci. USA *103*, 10068–10073.

Schmiedel, B.J., Singh, D., Madrigal, A., Valdovino-Gonzalez, A.G., White, B.M., Zapardiel-Gonzalo, J., Ha, B., Altay, G., Greenbaum, J.A., McVicker, G., et al. (2018). Impact of Genetic Polymorphisms on Human Immune Cell Gene Expression. Cell *175*, 1701–1715.

Selzner, N., Liu, H., Boehnert, M.U., Adeyi, O.A., Shalev, I., Bartczak, A.M., Xue-Zhong, M., Manuel, J., Rotstein, O.D., McGilvray, I.D., et al. (2012). FGL2/fibroleukin mediates hepatic reperfusion injury by induction of sinusoidal endothelial cell and hepatocyte apoptosis in mice. J. Hepatol. *56*, 153–159.

Shlyueva, D., Stampfel, G., and Stark, A. (2014). Transcriptional enhancers: from properties to genome-wide predictions. Nat. Rev. Genet. *15*, 272–286.

Shubin, N.J., Glukhova, V.A., Clauson, M., Truong, P., Abrink, M., Pejler, G., White, N.J., Deutsch, G.H., Reeves, S.R., Vaisar, T., et al. (2017). Proteome analysis of mast cell releasates reveals a role for chymase in the regulation of coagulation factor XIIIA levels via proteolytic degradation. J. Allergy Clin. Immunol. *139*, 323–334.

Siebenhaar, F., Redegeld, F.A., Bischoff, S.C., Gibbs, B.F., and Maurer, M. (2018). Mast Cells as Drivers of Disease and Therapeutic Targets. Trends Immunol. *39*, 151–162.

Sims, N.A. (2015). Cardiotrophin-like cytokine factor 1 (CLCF1) and neuropoietin (NP) signalling and their roles in development, adulthood, cancer and degenerative disorders. Cytokine Growth Factor Rev. *26*, 517–522.

Smemo, S., Tena, J.J., Kim, K.H., Gamazon, E.R., Sakabe, N.J., Gómez-Marín, C., Aneas, I., Credidio, F.L., Sobreira, D.R., Wasserman, N.F., et al. (2014). Obesity-associated variants within FTO form long-range functional connections with IRX3. Nature *507*, 371–375.

St John, A.L., and Abraham, S.N. (2013). Innate immunity and its regulation by mast cells. J. Immunol. *190*, 4458–4463.

Stunnenberg, H.G., and Hirst, M.; International Human Epigenome Consortium (2016). The International Human Epigenome Consortium: A Blueprint for Scientific Collaboration and Discovery. Cell *167*, 1145–1149.

Su, S., Law, C.W., Ah-Cann, C., Asselin-Labat, M.L., Blewitt, M.E., and Ritchie, M.E. (2017). Glimma: interactive graphics for gene expression analysis. Bioinformatics *33*, 2050–2052.

Suzuki, Y., Inoue, T., and Ra, C. (2012). Calcium signaling in mast cells: focusing on L-type calcium channels. Adv. Exp. Med. Biol. *740*, 955–977.

Tang, M., Cao, X., Li, P., Zhang, K., Li, Y., Zheng, Q.Y., Li, G.Q., Chen, J., Xu, G.L., and Zhang, K.Q. (2017). Increased expression of Fibrinogen-Like Protein 2 is associated with poor prognosis in patients with clear cell renal cell carcinoma. Sci. Rep. *7*, 12676.

Thorvaldsdóttir, H., Robinson, J.T., and Mesirov, J.P. (2013). Integrative Genomics Viewer (IGV): high-performance genomics data visualization and exploration. Brief. Bioinform. *14*, 178–192.

Thul, P.J., Åkesson, L., Wiking, M., Mahdessian, D., Geladaki, A., Ait Blal, H., Alm, T., Asplund, A., Björk, L., Breckels, L.M., et al. (2017). A subcellular map of the human proteome. Science *356*.

Tordesillas, L., Berin, M.C., and Sampson, H.A. (2017). Immunology of Food Allergy. Immunity *47*, 32–50.

Übel, C., Sopel, N., Graser, A., Hildner, K., Reinhardt, C., Zimmermann, T., Rieker, R.J., Maier, A., Neurath, M.F., Murphy, K.M., et al. (2014). The activating protein 1 transcription factor basic leucine zipper transcription factor, ATF-like (BATF), regulates lymphocyte- and mast cell-driven immune responses in the setting of allergic asthma. J. Allergy Clin. Immunol. *133*, 198–206.

Vaeth, M., Maus, M., Klein-Hessling, S., Freinkman, E., Yang, J., Eckstein, M., Cameron, S., Turvey, S.E., Serfling, E., Berberich-Siebelt, F., et al. (2017). Store-Operated Ca^{2+} Entry Controls Clonal Expansion of T Cells through Metabolic Reprogramming. Immunity *47*, 664–679.

Whyte, W.A., Orlando, D.A., Hnisz, D., Abraham, B.J., Lin, C.Y., Kagey, M.H., Rahl, P.B., Lee, T.I., and Young, R.A. (2013). Master transcription factors and mediator establish super-enhancers at key cell identity genes. Cell *153*, 307–319.

Yan, J., Kong, L.Y., Hu, J., Gabrusiewicz, K., Dibra, D., Xia, X., Heimberger, A.B., and Li, S. (2015). FGL2 as a Multimodality Regulator of Tumor-Mediated Immune Suppression and Therapeutic Target in Gliomas. J. Natl. Cancer Inst. *107*.

Zhang, Y., Liu, T., Meyer, C.A., Eeckhoute, J., Johnson, D.S., Bernstein, B.E., Nusbaum, C., Myers, R.M., Brown, M., Li, W., and Liu, X.S. (2008). Model-based analysis of ChIP-Seq (MACS). Genome Biol. *9*, R137.

STAR★METHODS

KEY RESOURCES TABLE

REAGENT or RESOURCE	SOURCE	IDENTIFIER
Antibodies		
Human IgE, myeloma	Calbiochem	Cat#401152; RRID: AB_2810964
Goat polyclonal anti-human IgE (ε-chain specific)	Sigma-Aldrich	Cat#I6284; RRID: AB_1079106
Mouse monoclonal anti-human FceRIα-FITC (clone CRA1)	Thermo Fisher Scientific	Cat#11-5899-42; RRID: AB_10732835
Mouse monoclonal anti-human FcεRIα-APC (clone CRA1)	Miltenyi Biotec	Cat#130-095-980; RRID: AB_10828234
Mouse monoclonal anti-human CD117-PE (clone YB5.B8)	Thermo Fisher Scientific	Cat#12-1179-41; RRID: AB_1659667
Mouse monoclonal anti-human CD117-APC (clone A3C6E2)	Miltenyi Biotec	Cat#130-098-207; RRID: AB_2660103
Mouse monoclonal IgG2b-FITC (clone eBMG2b)	Thermo Fisher Scientific	Cat#11-4732-42; RRID: AB_10598648
Mouse monoclonal IgG1-PE (clone P3.6.2.8.1)	Thermo Fisher Scientific	Cat#12-4714-41; RRID: AB_1944424
Mouse monoclonal anti-human tryptase (clone G3)	Millipore	Cat#MAB1222; RRID: AB_2206479
Rabbit monoclonal anti-human tryptase (clone EPR8476)	Abcam	Cat#ab134932; RRID: AB_2811029
Mouse monoclonal anti-human FGL2 (clone 6D9)	Abnova	Cat#H00010875-M01; RRID: AB_565732
Goat polyclonal anti-rabbit IgG Secondary Antibody, Alexa Fluor 488	Thermo Fisher Scientific	Cat#A-11008; RRID: AB_143165
Goat anti-Mouse IgG Secondary Antibody, Alexa Fluor 594	Thermo Fisher Scientific	Cat#R37121; RRID: AB_2556549
Rabbit polyclonal anti-human H3K27ac	Abcam	Cat#ab4729; RRID: AB_2118291
Rabbit polyclonal anti-human H3K4me3	Millipore	Cat#07-473; RRID: AB_1977252
Chemicals, Peptides, and Recombinant Proteins		
Lymphoprep	STEMCELL Technologies	Cat#07801
Insulin-Transferrin-Selenium (ITS-G)	GIBCO	Cat#41400045
2-Mercaptoethanol	GIBCO	Cat#21985023
Bovine Serum Albumin (BSA)	Sigma-Aldrich	Cat#A7979
Liberase	Roche	Cat#05401020001
Collagenase, Type I	GIBCO	Cat#17100017
IC Fixation Buffer	eBioscience	Cat#00-8222-49
Permeabilization Buffer	eBioscience	Cat#00-8333-56
Tissue-Tek O.C.T. Compound	Sakura Finetek	Cat#4583
Trypan Blue	GIBCO	Cat#15250061
ProLong Gold Antifade Mountant with DAPI	Molecular Probes	Cat#P36931
BAPTA, AM, cell permeant chelator	Invitrogen	Cat#B6769
Fluo-3, AM, calcium indicator	Invitrogen	Cat#F1242
May-Grünwald Stain	Sigma-Aldrich	Cat#MG500
Giemsa stain	Sigma-Aldrich	Cat#GS500
Formaldehyde solution	Sigma-Aldrich	Cat#F8775
Glycine	Astral Scientific	Cat#BIOGB0235
Protein A - Sepharose 4B	Invitrogen	Cat#101041
Recombinant human SCF	Shenandoah Biotechnology	Cat#100-04
Recombinant human IL-6	Shenandoah Biotechnology	Cat#100-10
Recombinant human IL-3	Shenandoah Biotechnology	Cat#100-80
Recombinant human IL-33	Peprotech	Cat#200-33

(*Continued on next page*)

Continued

REAGENT or RESOURCE	SOURCE	IDENTIFIER
Critical Commercial Assays		
QuantiTect Reverse Transcription kit	QIAGEN	Cat#205311
SYBR Green Master Mix	Bio-Rad	Cat#1725270
CD34 MicroBead Kit, human	Miltenyi Biotec	Cat#130-046-702
CD117 MicroBead Kit, human	Miltenyi Biotec	Cat#130-091-332
Zenon Alexa Fluor 488 Mouse IgG_1 Labeling Kit	Molecular Probes	Cat#Z25002
Human FGL2 ELISA Kit	BioLegend	Cat#436907
Human CLCF1 ELISA Kit	Lifespan Biosciences	Cat#LS-F26804
CLCF1 ELISA Kit	Aviva Systems Biology	Cat#OKEH04677
Human IL-4 ELISA Kit	BioLegend	Cat#430307
QIAquick PCR Purification Kit	QIAGEN	Cat#28104
NEBNext Ultra DNA Library Prep Kit for Illumina	New England Biolabs	Cat#E7370S
Nextera DNA Library Prep Kit	Illumina	Cat#FC-121-1030
TruSeq Stranded Total RNA Library Prep Kit with Ribo-Zero Gold	Illumina	Cat#RS-122-2301
Deposited Data		
Raw and analyzed data	This paper	GEO: GSE125931
CHIP-seq data	This paper	GEO: GSE125886
RNA-seq data	This paper	GEO: GSE125887
Omni-ATAC-seq data	This paper	GEO: GSE125888
Oligonucleotides		
Primer:18 s rRNA F: GCTTAATTTGACTCAAC ACGGGA	This paper	N/A
Primer:18 s rRNA R: AGCTATCAATCTGTCA ATCCTGTC	This paper	N/A
Primer: FGL2 F: CTTGCCAAGACTGCAAGCTG	This paper	N/A
Primer: FGL2 R: CCAGGCGACCATGAAGTACA	This paper	N/A
Primer: CLCF1 F: GCCTGGCGGATGGGATTATT	This paper	N/A
Primer: CLCF1 R: TGCACAGGCACGCTAACATC	This paper	N/A
Primer: CCL1 F: TCCATCTGCTCCAATGAGGG	This paper	N/A
Primer: CCL1 R: GCTGGTAGTTTCGGGGACAG	This paper	N/A
Primer: CCL4 F: GTCTGTGCTGATCCCAGTGA	This paper	N/A
Primer: CCL4 R: GCGGAGAGGAGTCCTGAGTA	This paper	N/A
Software and Algorithms		
FlowJo v.10.0.8	FlowJo, LLC	RRID: SCR_008520
GraphPad Prism 6	GraphPad Software	RRID: SCR_002798
LDMatrix	NIH	RRID: SCR_017391
DAVID 6.8	LHRI	RRID: SCR_001881
HOMER	N/A	RRID: SCR_010881
DiffBind	Bioconductor	RRID: SCR_012918
FastQC	Babraham Bioinformatics	RRID: SCR_014583
edgeR (version 3.3)	Bioconductor	RRID: SCR_012802; (Robinson et al., 2010)
Integrative Genomics Viewer (IGV)	Broad Institute	RRID: SCR_011793; (Thorvaldsdóttir et al., 2013)
Glimma	Bioconductor	RRID: SCR_017389; (Su et al., 2017)
BWA	N/A	RRID: SCR_010910; (Li and Durbin, 2009)
MACS2 (version 2.1.1)	GitHub	RRID: SCR_013291; (Zhang et al., 2008)
Bowtie 0.12.8	N/A	RRID: SCR_005476; (Langmead et al., 2009)
deepTools	GitHub	RRID: SCR_016366; (Ramírez et al, 2016)

(*Continued on next page*)

Continued

REAGENT or RESOURCE	SOURCE	IDENTIFIER
GREAT (2.02)	N/A	RRID: SCR_005807; (McLean et al., 2010)
GeneMania	Cytoscape	RRID: SCR_005709
GWAS catalog	NHGRI-EBI	RRID: SCR_012745
dbSNP	NIH	RRID: SCR_002338
ROSE	Young Lab	RRID: SCR_017390

LEAD CONTACT AND MATERIALS AVAILABILITY

Further information and requests for resources and reagents should be directed to and will be fulfilled by the Lead Contact, Vinay Tergaonkar (vinayt@imcb.a-star.edu.sg). This study did not generate new unique reagents.

EXPERIMENTAL MODEL AND SUBJECT DETAILS

All human studies have been approved by the Human Research Ethics Committee of Central Adelaide Local Health Network (CALHN). Informed consent was obtained from all subjects. Healthy donors provided blood samples for the isolation of $CD34^+$ cells. Patients with chronic spontaneous urticaria (CSU) provided skin biopsy samples. All donors were between 18-60 years old, and samples from both male and female donors were obtained. Subjects were not involved in previous procedures and they were drug or test naive.

METHOD DETAILS

Peripheral blood-derived MCs

Mature human MCs were generated from human peripheral blood-derived $CD34^+$ progenitor cells collected from healthy volunteers (Royal Adelaide Hospital). Briefly, peripheral blood was diluted with sterile phosphate buffered saline (PBS) at a ratio of 1:1, layered gently over Lymphoprep and after centrifugation (600 *g*, 30 min), the interface containing mononuclear cells was harvested and the remaining red blood cells were disrupted with haemolytic solution (155 mM NH_4Cl, 10 mM $KHCO_3$, 0.1 mM EDTA). $CD34^+$ progenitor cells were enriched by positive immunomagnetic selection using CD34 MicroBeads and an autoMACS Pro Separator (Miltenyi Biotec) according to the manufacturer's instructions. The isolated $CD34^+$ cells were then transferred into 12-well plates at a density of 5×10^6 cells/mL in IMDM medium supplemented with 1% insulin-transferrin selenium, 5×10^{-5} M 2-mercaptoethanol, 1% penicillin-streptomycin, 0.1% bovine serum albumin (BSA), 100 ng/mL recombinant human (rh) SCF, 50 ng/mL rhIL-6 and 5 ng/mL rhIL-3, and placed in a CO_2 incubator at 37°C. The cytokine-supplemented medium was replaced weekly and rhIL-3 was omitted from the medium after the first 3 weeks of culture. From week 6 onward, 10% FBS was added to the medium, and MCs were used at 10^{th} week of culture for all experiments. At that time, the populations contained over 98% MCs as determined by May Grünwald-Giemsa staining and by flow cytometric analysis. Human MCs were divided into 3 conditions for further analysis. Cells were either untreated or sensitized with human myeloma IgE (0.5 μg/mL) overnight. Next day, sensitized cells were washed with PBS and either untreated or treated for 2 h or 24 h with anti-human IgE (1 μg/mL) for FcεRI crosslinking. For IL-33-mediated MC activation, cells were incubated with rhIL-33 (10 ng/mL) (Jung et al., 2013) for 2 h.

Isolation of tonsillar MCs

Palatine tonsils were obtained from donors suffering from tonsilitis and undergoing tonsillectomy surgeries. After tonsillectomy, tissues were kept at 4°C in RPMI medium. Tissue was digested into smaller pieces with scissors and incubated with Liberase or Collagenase-1 in RPMI medium for 1 h at 37°C with intermittent shaking. The lysate was then filtered 3 times with 70 μm cell strainer and single cell suspension was washed with PBS containing 2% FBS and 1 mM EDTA. Red blood cells were lysed with haemolytic solution and the remaining cells were then filtered with 40 μm cell strainer. Afterward, $CD117^+$ cells were isolated using CD117 MicroBead Kit and autoMACS Pro Separator according to manufacturer's instructions. $CD117^+$ cells were then incubated with FcεRI-APC antibody (clone CRA1) for 20 min at RT and sorted with MoFlo Astrios EQ Cell Sorter (Beckman Coulter). Sample collection, cell sorting and Omni-ATAC-seq were performed on the same day. Cell viability after sorting was > 95% as determined by trypan blue staining.

Flow cytometric analysis

Peripheral blood-derived MCs were washed with PBS before incubation with human Fc Receptor blocking solution on ice for 15 min. After Fc blocking, MCs were incubated with anti-FcεRI-FITC and anti-CD117 (c-kit)-PE antibodies or isotype control IgG2b-FITC and IgG1-PE antibody for 30 min on ice. Cells were washed and then analyzed on a Beckman Coulter Gallios. For tonsillar MCs, an aliquot of magnetically isolated $CD117^+$ cells were incubated with anti-FcεRI-APC for 20 min at RT. Cells were fixed with 1% PFA for 15 min on ice, washed and then analyzed in flow cytometry. For determination of MC tryptase expression, cells were fixed in IC fixation buffer

(eBioscience) for 20 min at RT and incubated in permeabilization buffer (eBioscience) containing mouse anti-tryptase antibody or isotype control mouse IgG1 antibody that were pre-conjugated with Alexa Flour® 488 using Zenon® Mouse IgG labeling kit. After 30 min, cells were washed and then analyzed in flow cytometry.

ELISA

Supernatants from peripheral blood-derived human MCs were collected after stimulation with IgE+anti-IgE for 8 h, 16 h and 24 h. Cell debris was removed with centrifugation at 11,000 rpm for 10 min and supernatants were stored at −80°C. Supernatants were then used to measure the levels of soluble FGL2, CLCF1 and IL-4 according to the protocols described in ELISA kits.

CSU skin biopsy samples and confocal microscopy

After an acute allergic reaction, skin biopsies (4 mm punch biopsy) were collected from CSU patients attending a research clinic after taking their informed consent. Skin biopsies were immediately embedded in OCT compound and frozen blocks were stored at −80°C till retrieval for performing the assays. Samples were cut (8 μm sections) in cryostat, mounted on slides at −20°C and incubated at RT for 10 min. Subsequently, samples were fixed with 4% formaldehyde in PBS for 10 min at RT, washed 3 times with PBS and blocked with 10% goat serum for 1 h. Primary antibodies anti-FGL2 (mouse monoclonal, 1:75 dilution) and anti-Tryptase (rabbit monoclonal, 1:150 dilution) were incubated with samples overnight. Next day, samples were washed with PBS 3 times and secondary antibodies (AF488-conjugated goat anti-rabbit and AF594-conjugated goat anti-mouse, 1:200 dilution) were incubated with samples for 1 h at RT and slides were washed with PBS 5 times. Finally, slides were mounted with anti-fade mounting medium with DAPI and images were taken using Zeiss LSM 800 confocal microscope.

Calcium mobilization study

MCs were sensitized with myeloma IgE (1 μg/mL) for 16 h and incubated with BAPTA-AM (20 μM, Thermo Fisher) for 30 min before incubation with Fluo-3 AM (5 μM, Life Technologies) in Tyrodes buffer for 30 min at 37°C. Cells were placed in a 15μ-slide Microscopy Chamber (ibidi GmbH). Fluorometric measurements were commenced when > 95% of the cells had settled to the base of the chamber. 5 min after anti-IgE (1 μg/mL) treatment fluorescence intensity was measured at 5 s intervals by a Carl Zeiss LSM 700 Axio Observer. Changes in intracellular $Ca^{2+}[Ca^{2+}]_i$ were expressed as F1/F0 ratios where F1 and F0 were the fluorescence intensity at a specific time and at the initiation of image recording, respectively.

CHIP and CHIP-seq

For each CHIP assay, cells ($2x10^6$) were crosslinked with 1% formaldehyde for 10 min at RT on a rotating platform and formaldehyde was quenched with 125 mM glycine for 5 min. Fixed cells were washed with cold PBS twice and incubated with 5 mL Triton X-100 lysis buffer (0.25% Triton X-100, 10 mM EDTA, 10 mM Tris-HCl (pH:8.1), 100 mM NaCl and protease inhibitors) for 15 min on ice. Subsequently, for chromatin isolation and sonication, cell pellets were dissolved in SDS lysis buffer (1% SDS, 5 mM EDTA, 50 mM Tris-HCl (pH:8.1) and protease inhibitors) and incubated for 1 h at 4°C. Sonication was performed using Bioruptor (Diagenode) with 30 s on/off settings at high mode with 10 min intervals (totally 30 min). Chromatin size between 200-400 bp was considered as optimal for subsequent steps. For immunoprecipitation, sonicated chromatin was diluted 4 times with dilution buffer (1% Triton X-100, 2 mM EDTA, 20 mM Tris-HCl (pH:8.1), 150 mM NaCl and protease inhibitors) and blocked with pre-treated protein-A agarose beads (Dynabeads, Invitrogen) for 2 h on a rotating platform in cold room. Overnight immunoprecipitation was performed using 2.5 μg CHIP grade H3K27ac and H3K4me3 antibodies on a rotating platform in cold room. Next day, 40 μL pre-treated protein A beads were incubated with lysates for 2 h to capture antibody-antigen complexes. Bead-captured complexes were washed with TSE buffer-1 (0.1% NP-40, 1% Triton X-100, 2 mM EDTA, 20 mM Tris-HCl (pH:8.1), 150 mM NaCl), then with TSE buffer-2 (0.1% SDS, 1% Triton X-100, 2 mM EDTA, 20 mM Tris-HCl (pH:8.1), 500 mM NaCl), with Buffer-3 (0.25 M LiCl, 1% NP-40, 1% deoxycholate, 1 mM EDTA, 10 mM Tris-HCl (pH:8.1) and finally with TE-washing buffer (2 mM EDTA, 10 mM Tris-HCl (pH:8.1). DNA was eluted with freshly-prepared elution buffer (1% SDS, 0.1 M $NaHCO_3$) at RT on a rotating platform for 1 h. Samples were incubated at 65°C for reverse-cross-linking, and DNA was isolated with QIAquick PCR Purification Kit (QIAGEN) and quantified using Qubit fluorometer according to the manufacturer's instructions. 10 ng immunoprecipitated DNA was used to generate CHIP-seq libraries using NEB Next Ultra kit. End repair, adaptor ligation, size selection, PCR amplification and cleanup steps were performed according to the instructions in the kit. DNA libraries were sequenced on the Illumina Nextseq 500 at the Genome Institute of Singapore (GIS).

Omni-ATAC-seq

An improved version of ATAC-seq known as Omni-ATAC-seq was peformed as described before (Corces et al., 2017). Briefly, 50,000 MCs were resuspended in 50 μL ATAC-Resuspension-Buffer (RSB) (10 mM Tris-HCl pH:7.4, 10 mM NaCl, 3 mM $MgCl_2$, 0.1% NP-40, 0.1% Tween-20 and 0.01% Digitonin) and incubated 3 min on ice. Lysate was washed with 1 mL ATAC-RSB (with Tween-20 but without NP-40 and Digitonin) and Nextera DNA Library Prep Kit (Illumina, Cat No: FC-121-1030) was used for transposition reaction. Cell pellet was resuspended in 50 μL transposition mixture (25 μL 2X transposition buffer, 2.5 μL transposase, 16.5 μL PBS, 0.5 μL 1% digitonin, 0.5 μL 10% Tween-20, 5 μL H_2O) and incubated for 30 min at 37°C with 1000 RPM mixing. Cleanup was performed using QIAquick PCR Purification Kit and eluted samples (20 μl) were used for PCR amplification reaction (2.5 μL of 25 μM Primer Ad1, 2.5 μL of 25 μM Primer Ad2, 25 μL of 2X NEBNext Master Mix, 20 μL of transposed sample). Cycling conditions were: 72°C for 5 min, 98°C for 30 s, and 5 cycles of: 98°C for 10 s, 63°C 30 s, 72°C 1 min. Reaction was cleaned up with QIAquick PCR Purification Kit and library

size was determined using Agilent 2100 Bioanalyzer. To remove primer dimers and large fragments, double-sided bead purification was performed using Axygen Magnetic beads. Final library quantity was determined with Qubit® (1.0) Fluorometer (Life Technologies, California, USA). Samples with different barcodes were pooled (4 nM, 20 μl) and sequencing was performed on the Illumina NextSeq 500 using 2x75-bp reads at the Australian Cancer Research Foundation (ACRF) Cancer Genomics Facility.

RNA isolation and RNA-seq

Total RNA was isolated with TRIzol Reagent and RNeasy kit (QIAGEN) and analyzed with a Nanodrop. cDNA was synthesized using QuantiTect Reverse Transcription kit (QIAGEN) and RT-qPCR was performed using SYBR Green Master Mix (Bio-Rad). For RNA sequencing, RNA quality and quantity were further determined with Agilent Bioanalyzer. RNA integrity number (RIN) > 8 were considered to be optimal for RNA-seq preparation. Starting with 1 μg total RNA, Illumina Truseq Low Sample (LS) kit was used for generating RNA-seq libraries. Briefly, Ribosomal RNA (rRNA) depletion, 1st strand cDNA synthesis, 2nd strand cDNA synthesis, 3′ adenylation, adaptor ligation, PCR amplification, library validation and pooling were performed according to the protocols in the kit. 18S rRNA was used as housekeeping gene for normalization in all RT-qPCRs.

GWAS analysis

GWAS data were compiled using GWAS catalog (https://www.ebi.ac.uk/gwas/) using 30 different inflammatory and autoimmune disease traits with at least 5 non-HLA SNPs available with genome-wide significance (p value $\leq 5.0 \times 10^{-8}$). SNPs located in HLA regions were removed from the analysis. SNP genomic locations in Genome Assembly GRCh38.p10 was also confirmed using dbSNP database (https://www.ncbi.nlm.nih.gov/SNP/). In the same disease trait, some SNPs have been identified in multiple studies, and only single study was selected. Also, certain SNPs were implicated in multiple disease traits, and those SNPs were not removed from the analysis. R^2 and D' values of Linkage Disequilibrium (LD), as determined by LDmatrix, were included for SNPs located in Tonsillar MCs (Table S6).

Bioinformatics analysis of CHIP-seq data

Raw reads were analyzed and quality checked using the FastQC program. Reads were mapped to the human references genome (Hg19) from University of California Santa Cruz (UCSC) using Bowtie 0.12.8 (Langmead et al., 2009) with default parameters except –m 1 and –segment-mismatches 2. Only reads mapping uniquely to the genome with at most two mismatches were kept. Enriched regions of the genome were identified with the MACS2 (version 2.1.1) (Zhang et al., 2008) peak caller using default parameters and setting a p value cut-off of 1.00e-5. To limit PCR-induced biases duplicate reads were filtered by MACS. For histone marks, peak-calling mode for broad regions was employed and a p value cut-off of 1.00e-5 was again used. Differential binding analysis was performed using R (version 3.4.3) and the DiffBind package. To identify top enhancers, enhancer ranking was performed by the standard parameters of ROSE algorithm using normalized H3K27ac CHIP-seq reads (Whyte et al., 2013). TSS exclusion zone size (to exclude regions contained within ± distance from TSS to account for promoter biases) was chosen as 2500. Maximum distance between two regions that will be stitched together was chosen as 12.5kb. To identify activated and repressed enhancers upon stimulation, typical enhancer regions were annotated by removing ± 2.5kb region from TSS regions as previously described (Farh et al., 2015). Features in the vicinity of peak loci and enrichment of motifs within peaks were determined and analyzed using Homer (Heinz et al., 2010). Clustering of H3K4me3 peaks over TSS regions was carried out using deepTools2 (Ramírez et al, 2016). Heatmaps were generated using R (version 3.2.3). Integrative Genomics Viewer (IGV) (Thorvaldsdóttir et al, 2013) was used for visualizing all alignments. Gene ontology enrichment of genes nearest to peak loci were performed using GREAT (2.02) (McLean et al., 2010).

Bioinformatics analysis of Omni-ATAC-seq data

Raw reads were adaptor trimmed and filtered for short sequences using cutadapt v1.8.1 setting minimum-length option to 18, error-rate 0.2 and overlap 5. The resulting FASTQ files averaging 52 million reads per sample were analyzed and quality checked using the FastQC program. The filtered reads were mapped against the human reference genome (Hg19) using the BWA alignment algorithm (version 0.7.9a-r786 with default parameters) (Li and Durbin, 2009) returning an average alignment rate of 98.5%. Enriched regions of the genome were identified using the MACS2 peak caller (version 2.1.1) (Zhang et al., 2008) setting default parameters and reporting only peaks with a FDR cut-off (-q) of 0.05. Differential binding analysis was performed using R (version 3.4.3) and the DiffBind package. Enrichment of DNA motifs within differential peaks was assessed using the findMotifsGenome.pl script from the HOMER package (Heinz et al., 2010) with default settings. Alignments were visualized and interrogated using IGV (Thorvaldsdóttir et al, 2013).

Bioinformatics analysis of RNA-seq data

RiboZero-depleted RNA-seq libraries from 4 biological replicates for each treatment were multiplexed and sequenced on the Illumina NextSeq 500 platform (high output mode) using the stranded, paired end protocol with a read length of 75. Raw data, averaging 22.5 million read pairs per sample were analyzed and quality checked using the FastQC program. Reads were mapped against the human reference genome (Hg19) using the STAR spliced alignment algorithm (Dobin et al., 2013) (version 2.5.3a with default parameters and–chimSegmentMin 20,–quantMode GeneCounts) returning an average unique alignment rate of 91%. Differential expression analysis was evaluated from TMM normalized gene counts using R (version 3.2.3) and edgeR (Robinson et al., 2010) (version 3.3) following protocols as described (Lun et al., 2016) Alignments were visualized and interrogated using the Integrative Genomics Viewer v2.3.80 (Thorvaldsdóttir et al, 2013). Graphical representations of differentially expressed genes were generated

using Glimma (Su et al., 2017). Gene ontology enrichment of differentially expressed candidates was performed using DAVID (Huang da et al., 2009).

QUANTIFICATION AND STATISTICAL ANALYSIS

Student's t test was used to compare the gene expression levels in quantitative PCR analyses (with mean+SD). For plots showing more than 2 groups, one-way ANOVA with Dunnett's Multiple Comparison test was used. All statistical analyses were performed with Prism software version 6 (GraphPad Software).

DATA AND CODE AVAILABILITY

The datasets generated during this study are available at the Gene Expression Omnibus (GEO) database (GEO ID: GSE125931).

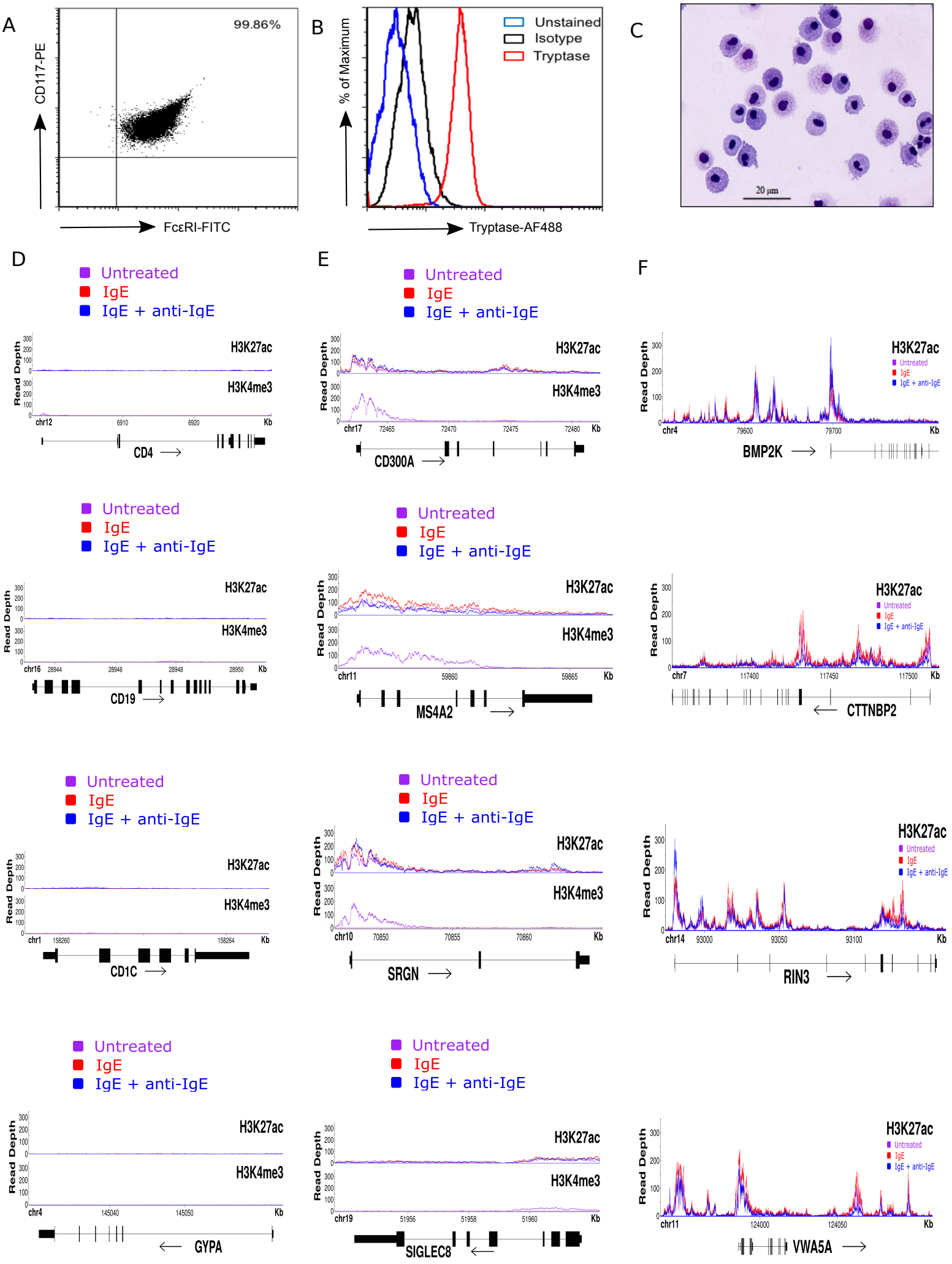
Immunity, Volume *51*

Supplemental Information

Genome-wide Analyses of Chromatin State in Human Mast Cells Reveal Molecular Drivers and Mediators of Allergic and Inflammatory Diseases

Gökhan Cildir, John Toubia, Kwok Ho Yip, Mingyan Zhou, Harshita Pant, Pravin Hissaria, Jingxian Zhang, Wanjin Hong, Nirmal Robinson, Michele A. Grimbaldeston, Angel F. Lopez, and Vinay Tergaonkar

Figure-S1


A
99.86%
CD117-PE
FcεRI-FITC
B
% of Maximum
Unstained
Isotype
Tryptase
Tryptase-AF488
C
20 μm
D
Untreated
IgE
IgE + anti-IgE
H3K27ac
H3K4me3
Read Depth
CD4
CD19
CD1C
E
CD300A
MS4A2
SRGN
F
BMP2K
CTTNBP2
RIN3
GYPA
SIGLEC8
VWA5A

Supplementary Figure-1: Assesment of the purity of peripheral blood-derived MCs and specificity of H3K27ac and H3K4me3 CHIP-seq datasets. Related to Figure-1.

A-C) Human peripheral blood-derived MC purity was assessed by cell surface staining of CD117 (c-kit) and FcεRI, intracellular tryptase staining, and May-Grünwald Giemsa staining. >98% pure MC population was obtained. Data is representative of 4 independent biological replicates. Scale bars are 20 microns.

D) Sushi plots of H3K27ac and H3K4me3 signals in selected chromatin regions in genes not expressed in MCs (CD4, CD19, GYPA, CD1c), showing the specificity of CHIP-seq datasets.

E) Sushi plots of H3K27ac and H3K4me3 signals in selected chromatin regions highly expressed in MCs (CD300A, MS4A2, SRGN, SIGLEC8), showing the specificity of chromatin preparation and CHIP-seq datasets.

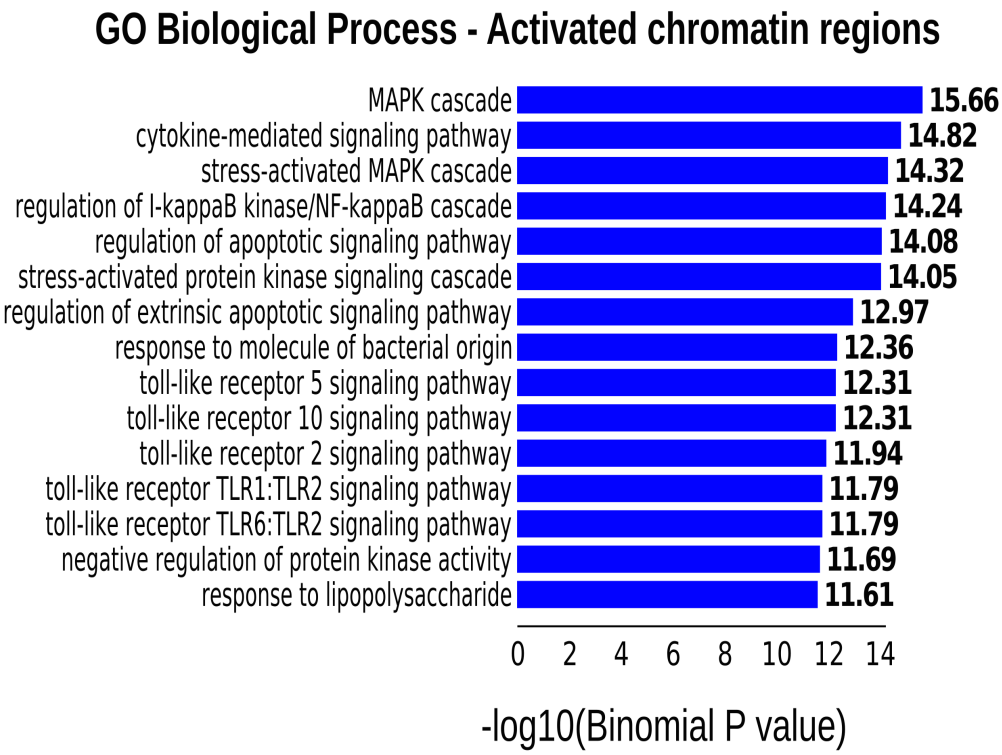
F) Sushi plots of H3K27ac signals in BMP2K, CTTNBP2, RIN3, VWA5A genes harbouring top enhancer regions.

Figure-S2

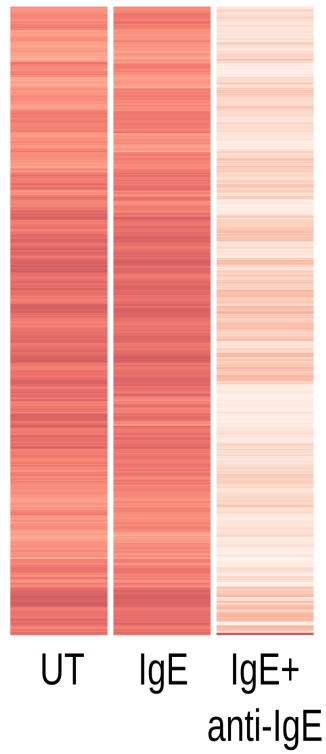
A



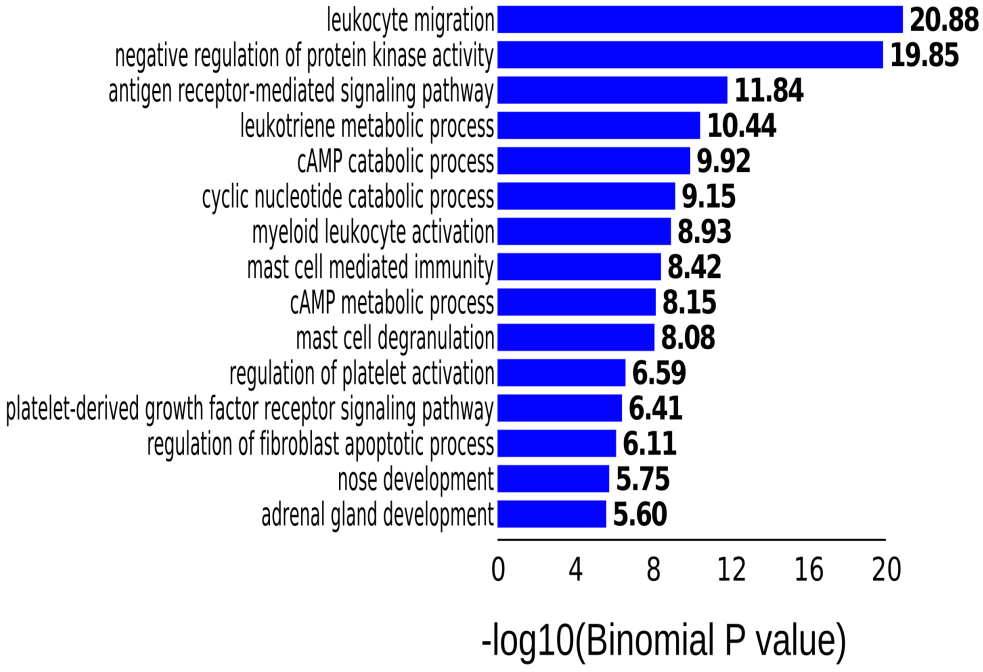
B



C



D



Supplementary Figure-2: Genome-wide remodeling of chromatin regions upon FcεRI crosslinking and GO terms for genes associated with these regions. Related to Figure-1.

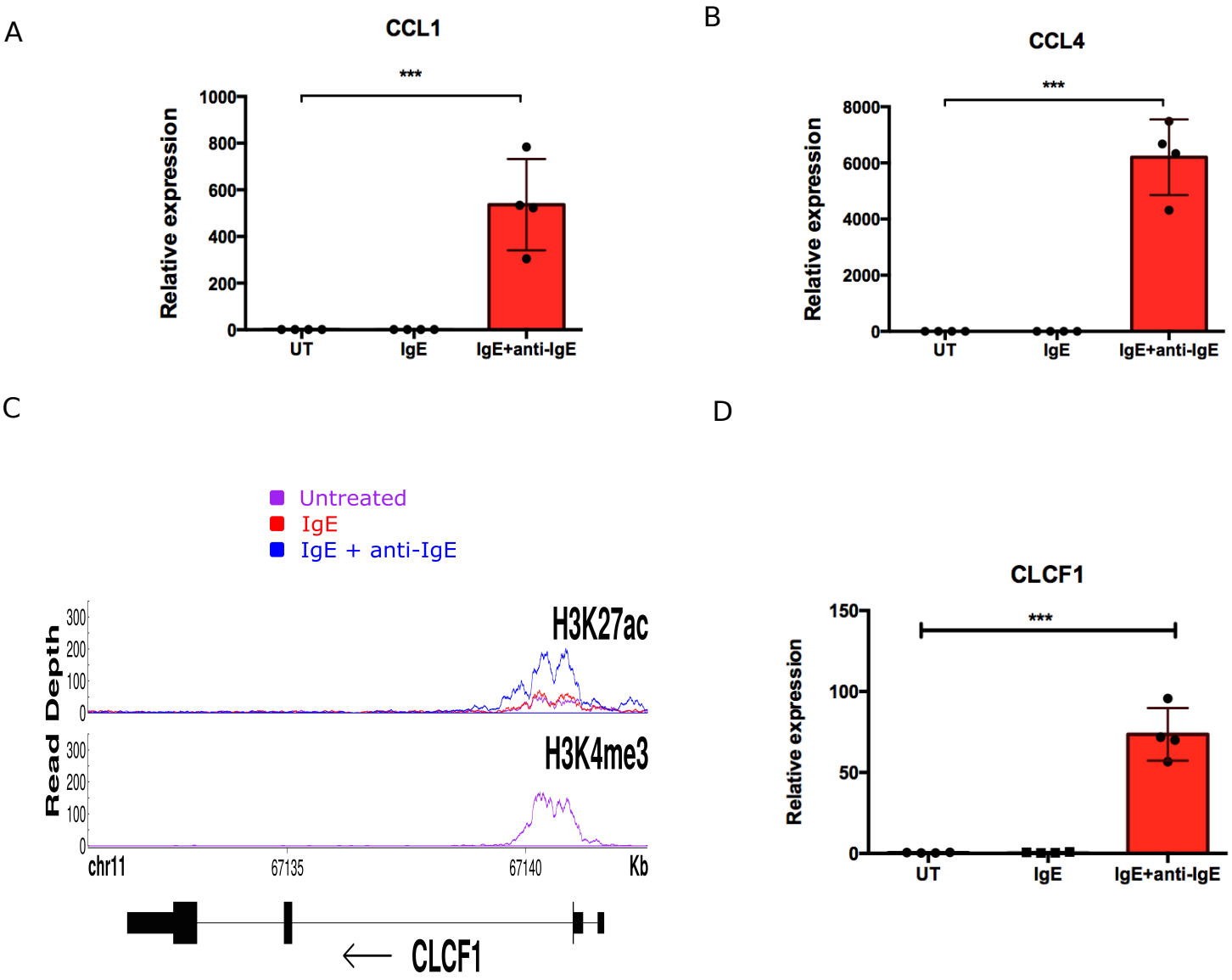
A) Using H3K27ac CHIP-seq datasets, activated chromatin regions were identified upon IgE sensitization alone and upon IgE+anti-IgE treatment compared to untreated MCs. No significant differences were observed upon IgE sensitization alone compared to untreated. Each red line represents a unique activated chromatin region in human MCs. Data are from 2 independent biological replicates.

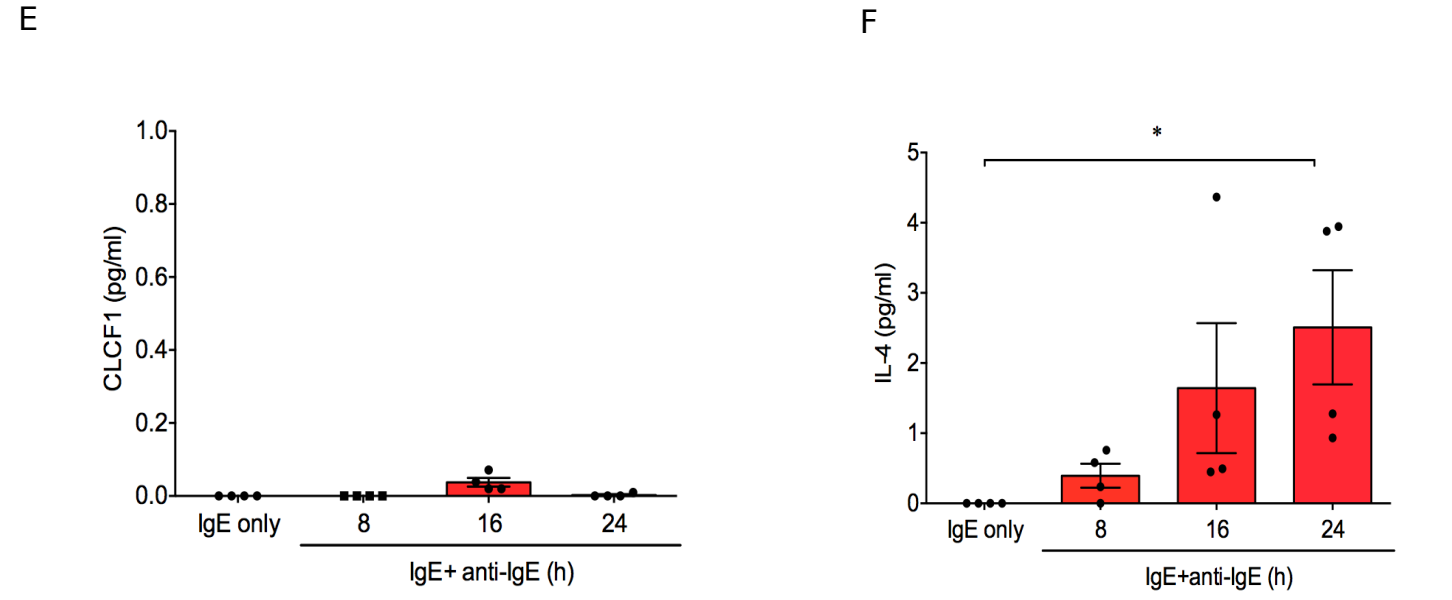
B) Top-15 significantly enriched GO Biological Process terms for genes associated with activated chromatin regions as determined by DAVID. Data are from 2 independent biological replicates.

C) Using H3K27ac CHIP-seq datasets, repressed chromatin regions were identified upon IgE sensitization alone and upon IgE+anti-IgE treatment compared to untreated MCs. No significant differences were observed upon IgE sensitization alone compared to untreated. Each red line represents a unique repressed chromatin region in human MCs. Data are from 2 independent biological replicates.

D) Top-15 significantly enriched GO Biological Process terms for genes associated with repressed chromatin regions as determined by DAVID. Data are from 2 independent biological replicates.

Figure-S3


A
CCL1
***
Relative expression
1000
800
600
400
200
0
UT
IgE
IgE+anti-IgE
B
CCL4
***
Relative expression
8000
6000
4000
2000
0
UT
IgE
IgE+anti-IgE
C
Untreated
IgE
IgE + anti-IgE
Read Depth
H3K27ac
H3K4me3
300
200
100
0
chr11
67135
67140
Kb
CLCF1
D
CLCF1
***
Relative expression
150
100
50
0
UT
IgE
IgE+anti-IgE


E
CLCF1 (pg/ml)
1.0
0.8
0.6
0.4
0.2
0.0
IgE only
8
16
24
IgE+ anti-IgE (h)
F
*
IL-4 (pg/ml)
5
4
3
2
1
0
IgE only
8
16
24
IgE+anti-IgE (h)

Supplementary Figure-3: Analysis of gene expression of CCL1, CCL4 and CLCF1 and secretion of CLCF1 and IL-4. Related to Figure-2.

A) RT-qPCR analysis of CCL1 mRNA levels in untreated, IgE-sensitized and IgE+anti-IgE-treated MCs, n=4 biological replicates, $p<0.001$. Error bars are mean ± SD.

B) RT-qPCR analysis of CCL4 mRNA levels in untreated, IgE-sensitized and IgE+anti-IgE-treated MCs, n=4 biological replicates, $p<0.001$. Error bars are mean ± SD.

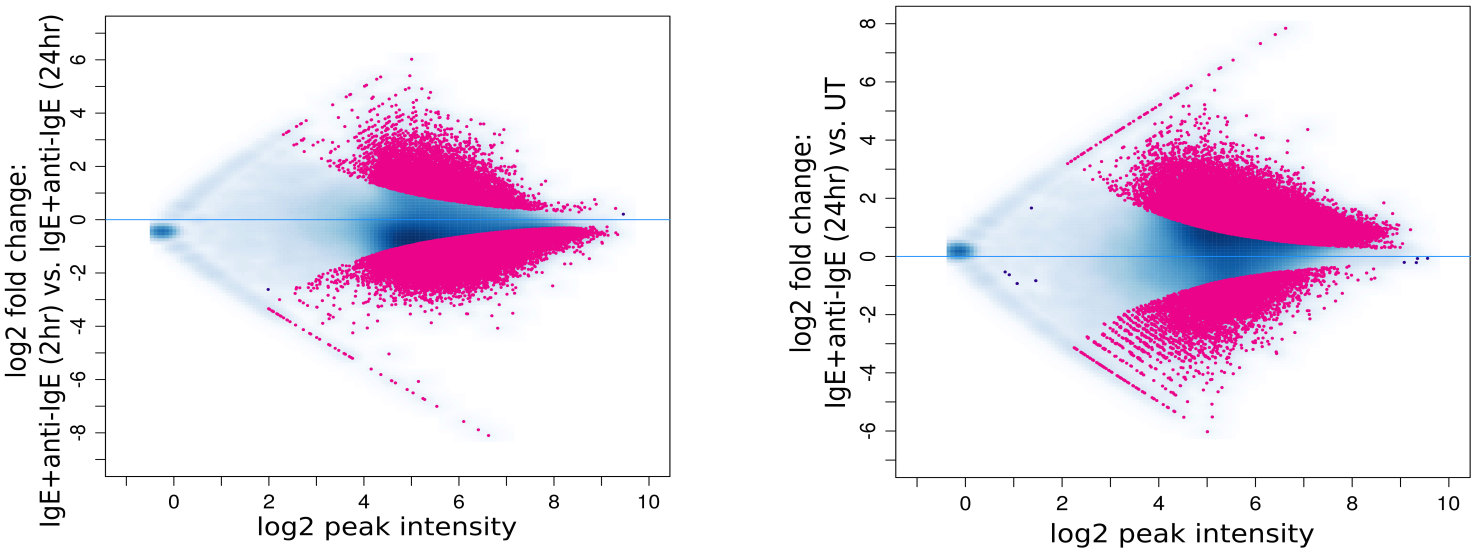
C) IgE+anti-IgE-mediated H3K27ac modifications in CLCF1 locus. H3K4me3 peaks were also indicated in untreated condition.

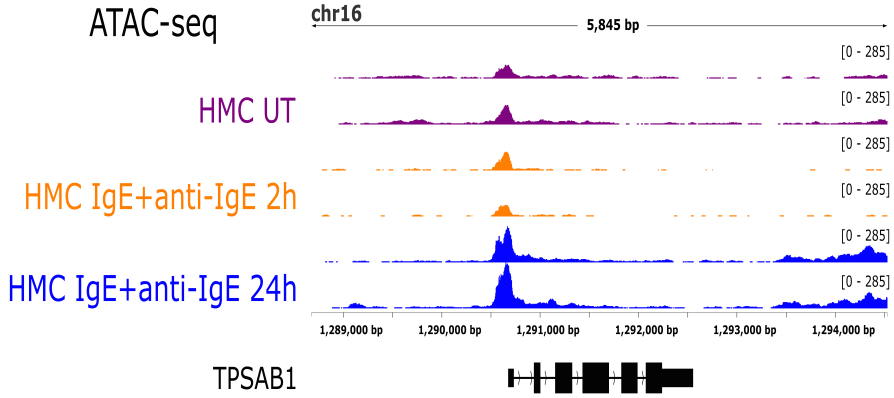
D) RT-qPCR analysis of CLCF1 mRNA levels in untreated, IgE-sensitized and IgE+anti-IgE-treated MCs, n=4 biological replicates, $p<0.001$. Error bars are mean ± SD.

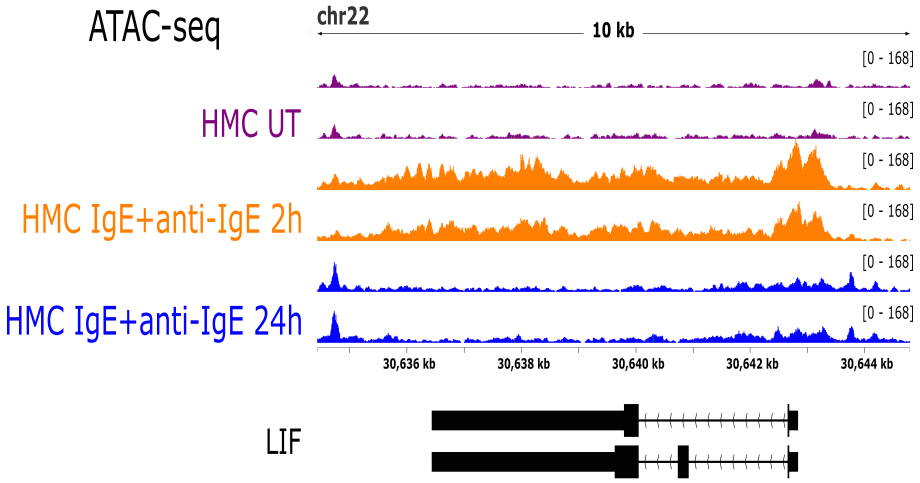
E) CLCF1 ELISA analysis using supernatants of untreated, IgE-sensitized and IgE+anti-IgE-treated MCs in indicated time points. Results are from 4 biological replicates, $p> 0.05$. Error bars are mean ±SD.

F) IL-4 ELISA analysis using supernatants of untreated, IgE-sensitized and IgE+anti-IgE-treated MCs in indicated time points, results are from 4 biological replicates, $p<0.05$. Error bars are mean ±SD.

Figure-S4


log2 fold change:
IgE+anti-IgE (2hr) vs. IgE+anti-IgE (24hr)
log2 peak intensity
log2 fold change:
IgE+anti-IgE (24hr) vs. UT
log2 peak intensity

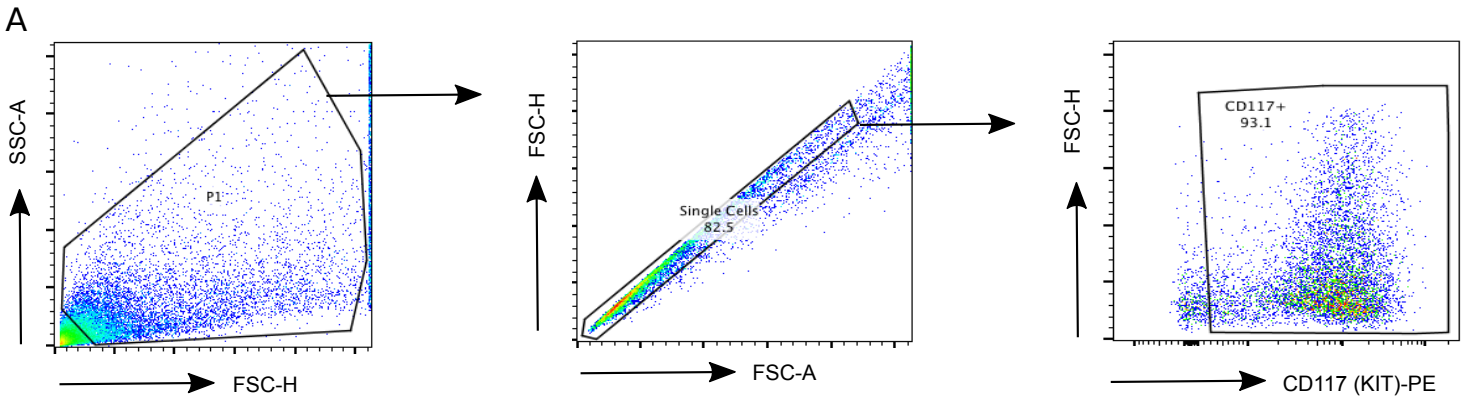

ATAC-seq
chr16
5,845 bp
HMC UT
HMC IgE+anti-IgE 2h
HMC IgE+anti-IgE 24h
[0 - 285]
1,289,000 bp
1,290,000 bp
1,291,000 bp
1,292,000 bp
1,293,000 bp
1,294,000 bp
TPSAB1

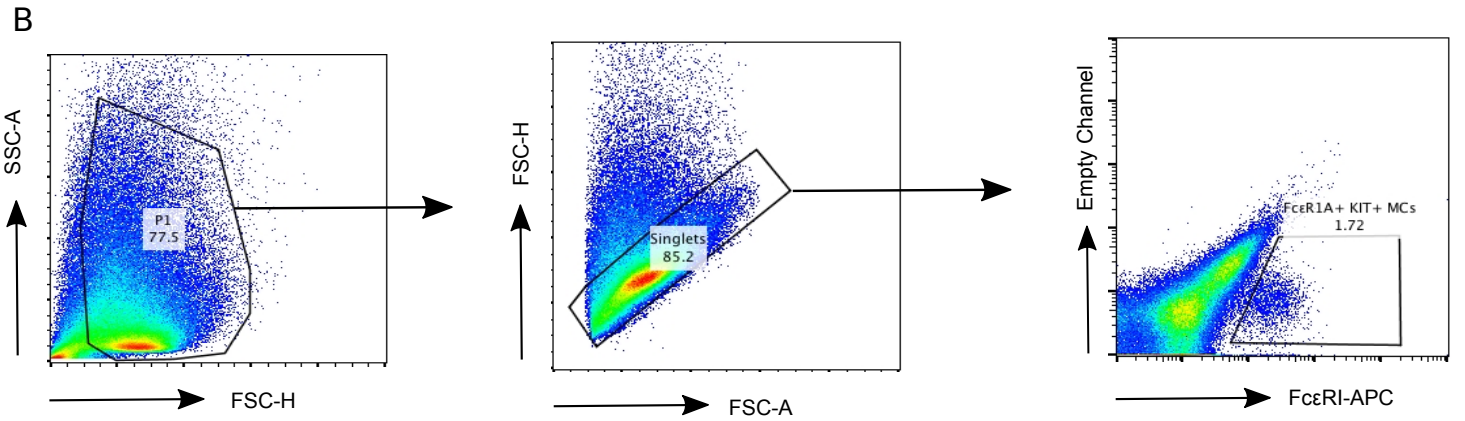

ATAC-seq
chr22
10 kb
HMC UT
HMC IgE+anti-IgE 2h
HMC IgE+anti-IgE 24h
[0 - 168]
30,636 kb
30,638 kb
30,640 kb
30,642 kb
30,644 kb
LIF

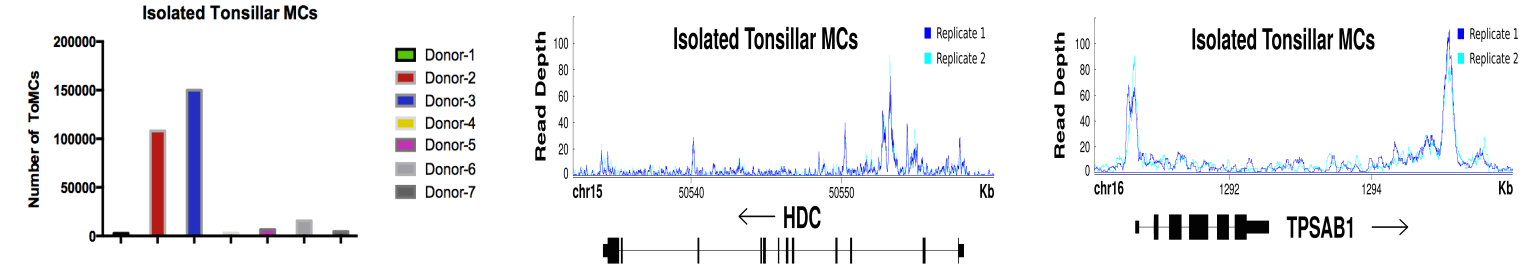
Supplementary Figure-4: Global comparison of Omni-ATAC-seq peaks for UT, 2h anti-IgE and 24h anti-IgE treatment. Related to Figure-4.

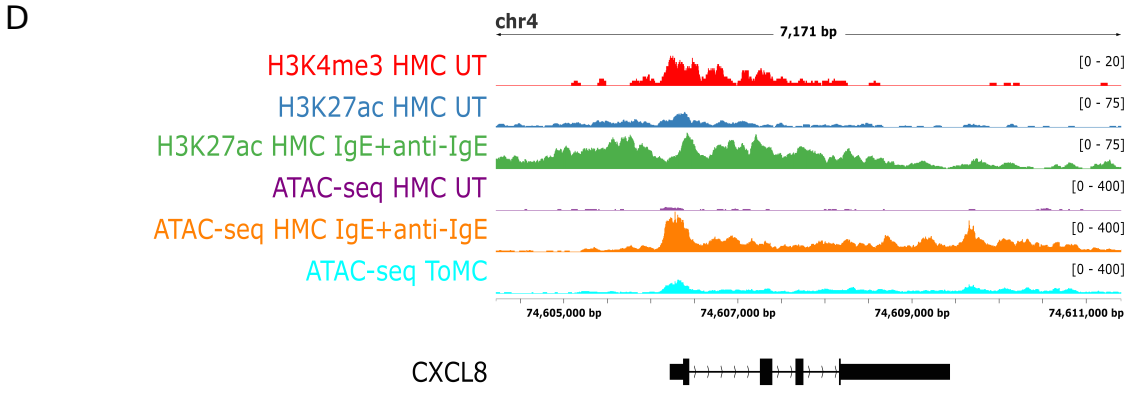
Differential Omni-ATAC-seq peak analysis using UT, 2h anti-IgE treatment and 24h anti-IgE treatment conditions. Omni-ATAC-seq tracks were shown in the loci of TPSAB1 and LIF genes in which dynamic chromatin changes occurred in peripheral blood-derived MCs (HMC).

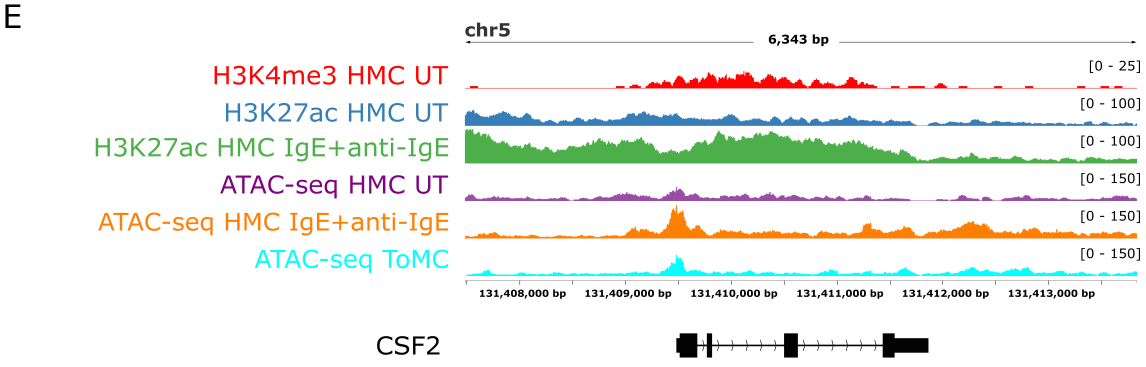
Figure-S5


A
SSC-A
FSC-H
P1
FSC-H
FSC-A
Single Cells
82.5
FSC-H
CD117+
93.1
CD117 (KIT)-PE


B
SSC-A
FSC-H
P1
77.5
FSC-H
FSC-A
Singlets
85.2
Empty Channel
FcεR1A+ KIT+ MCs
1.72
FcεRI-APC


C
Isolated Tonsillar MCs
Number of ToMCs
200000
150000
100000
50000
0
Donor-1
Donor-2
Donor-3
Donor-4
Donor-5
Donor-6
Donor-7
Isolated Tonsillar MCs
Replicate 1
Replicate 2
Read Depth
chr15
50540
50550
Kb
HDC
Isolated Tonsillar MCs
Replicate 1
Replicate 2
Read Depth
chr16
1292
1294
Kb
TPSAB1


D
chr4
7,171 bp
H3K4me3 HMC UT
H3K27ac HMC UT
H3K27ac HMC IgE+anti-IgE
ATAC-seq HMC UT
ATAC-seq HMC IgE+anti-IgE
ATAC-seq ToMC
[0 - 20]
[0 - 75]
[0 - 75]
[0 - 400]
[0 - 400]
[0 - 400]
74,605,000 bp
74,607,000 bp
74,609,000 bp
74,611,000 bp
CXCL8


E
chr5
6,343 bp
H3K4me3 HMC UT
H3K27ac HMC UT
H3K27ac HMC IgE+anti-IgE
ATAC-seq HMC UT
ATAC-seq HMC IgE+anti-IgE
ATAC-seq ToMC
[0 - 25]
[0 - 100]
[0 - 100]
[0 - 150]
[0 - 150]
[0 - 150]
131,408,000 bp
131,409,000 bp
131,410,000 bp
131,411,000 bp
131,412,000 bp
131,413,000 bp
CSF2

Supplementary Figure-5: Isolation of tonsillar MCs and assesment of the specificity of Omni-ATAC-seq peaks from tonsillar MCs. Related to Figure-6.

A) Tonsillar MCs were isolated with a 2-step protocol. Single cells were prepared from tonsillar tissue and $CD117^+$ (c-kit) cells were magnetically isolated with CD117 MicroBead Kit. An aliquot of cells showed that the purity of $CD117^+$ cell isolation was typically >93-94% as determined by flow cytometry.

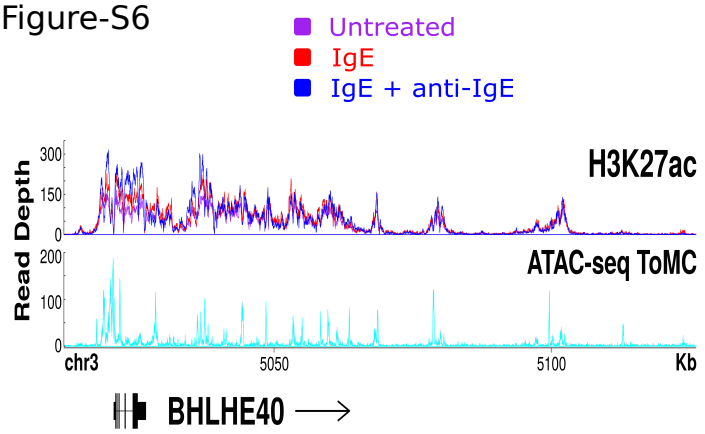
B) Magnetically isolated $CD117^+$ cells were then used for sorting with FcεRI-APC antibody (clone CRA1). Gating strategy was shown. Sorted $CD117^+$ $FcεRI^+$ tonsillar MCs were used for Omni-ATAC-seq.

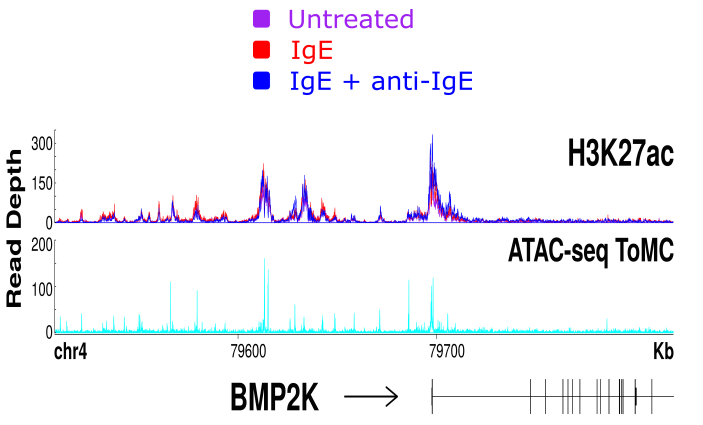
C) The number of isolated tonsillar MCs from each donor was indicated (n=7 donors). Omni-ATAC-seq peaks in TPSAB1 and HDC loci from tonsillar MCs were shown.

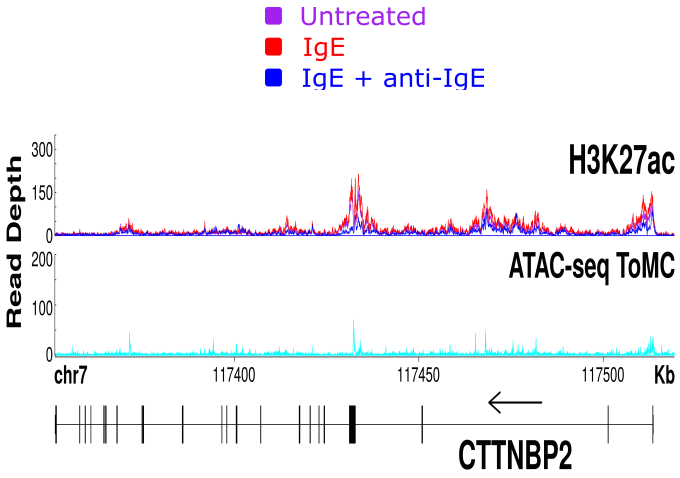
D) IGV tracks of CXCL8 (IL-8) gene loci in untreated and IgE+anti-IgE-treated peripheral blood-derived MCs (HMC) and in isolated tonsillar MCs (ToMC). Data are from 2 independent biological replicates.

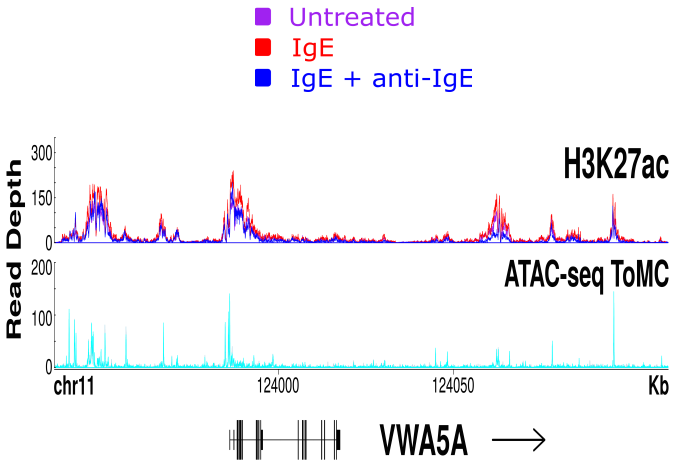
E) IGV tracks of CSF2 gene loci in untreated and IgE+anti-IgE-treated peripheral blood-derived MCs (HMC) and in isolated tonsillar MCs (ToMC). Data are from 2 independent biological replicates.

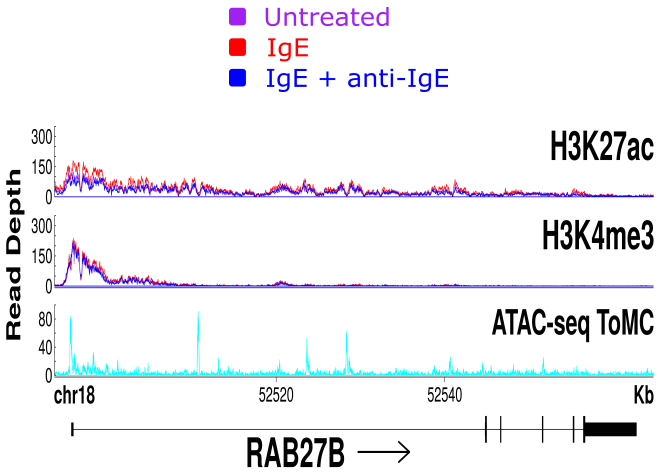
Figure-S6

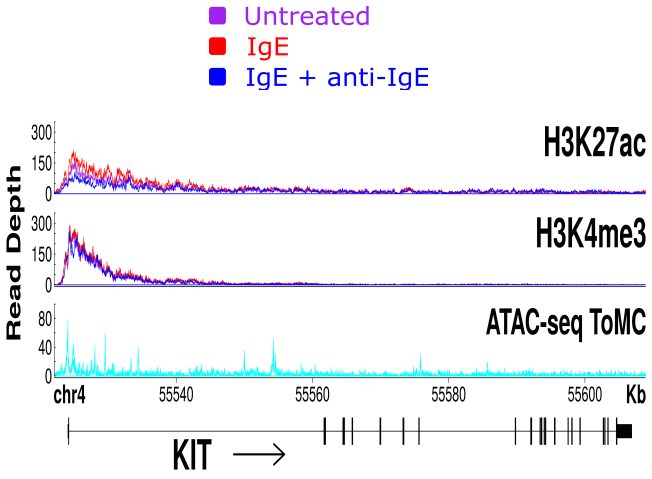

Untreated
IgE
IgE + anti-IgE
H3K27ac
ATAC-seq ToMC
Read Depth
chr3
5050
5100
Kb
BHLHE40

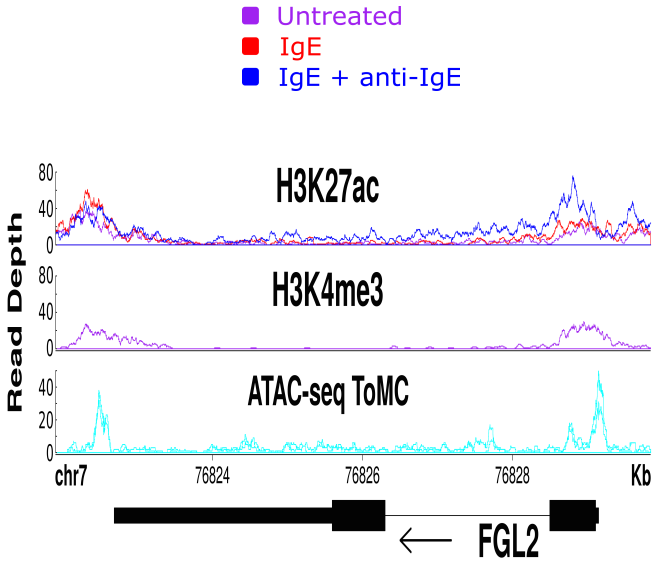

Untreated
IgE
IgE + anti-IgE
H3K27ac
ATAC-seq ToMC
Read Depth
chr4
79600
79700
Kb
BMP2K

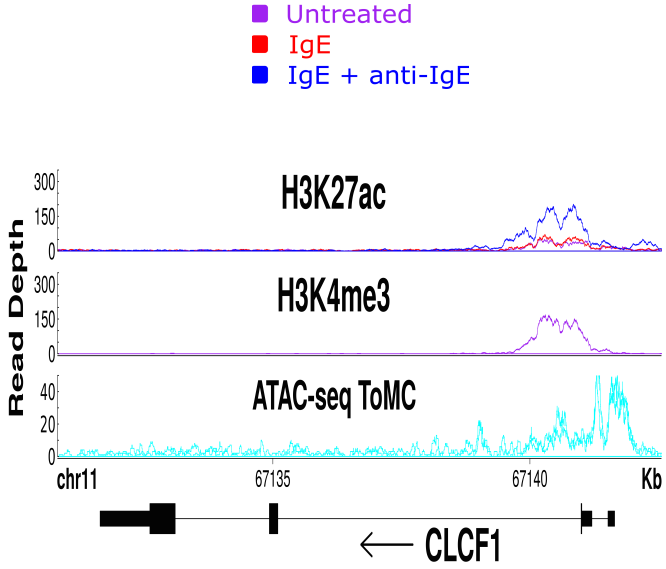

Untreated
IgE
IgE + anti-IgE
H3K27ac
ATAC-seq ToMC
Read Depth
chr7
117400
117450
117500
Kb
CTTNBP2


Untreated
IgE
IgE + anti-IgE
H3K27ac
ATAC-seq ToMC
Read Depth
chr11
124000
124050
Kb
VWA5A


Untreated
IgE
IgE + anti-IgE
H3K27ac
H3K4me3
ATAC-seq ToMC
Read Depth
chr18
52520
52540
Kb
RAB27B


Untreated
IgE
IgE + anti-IgE
H3K27ac
H3K4me3
ATAC-seq ToMC
Read Depth
chr4
55540
55560
55580
55600
Kb
KIT

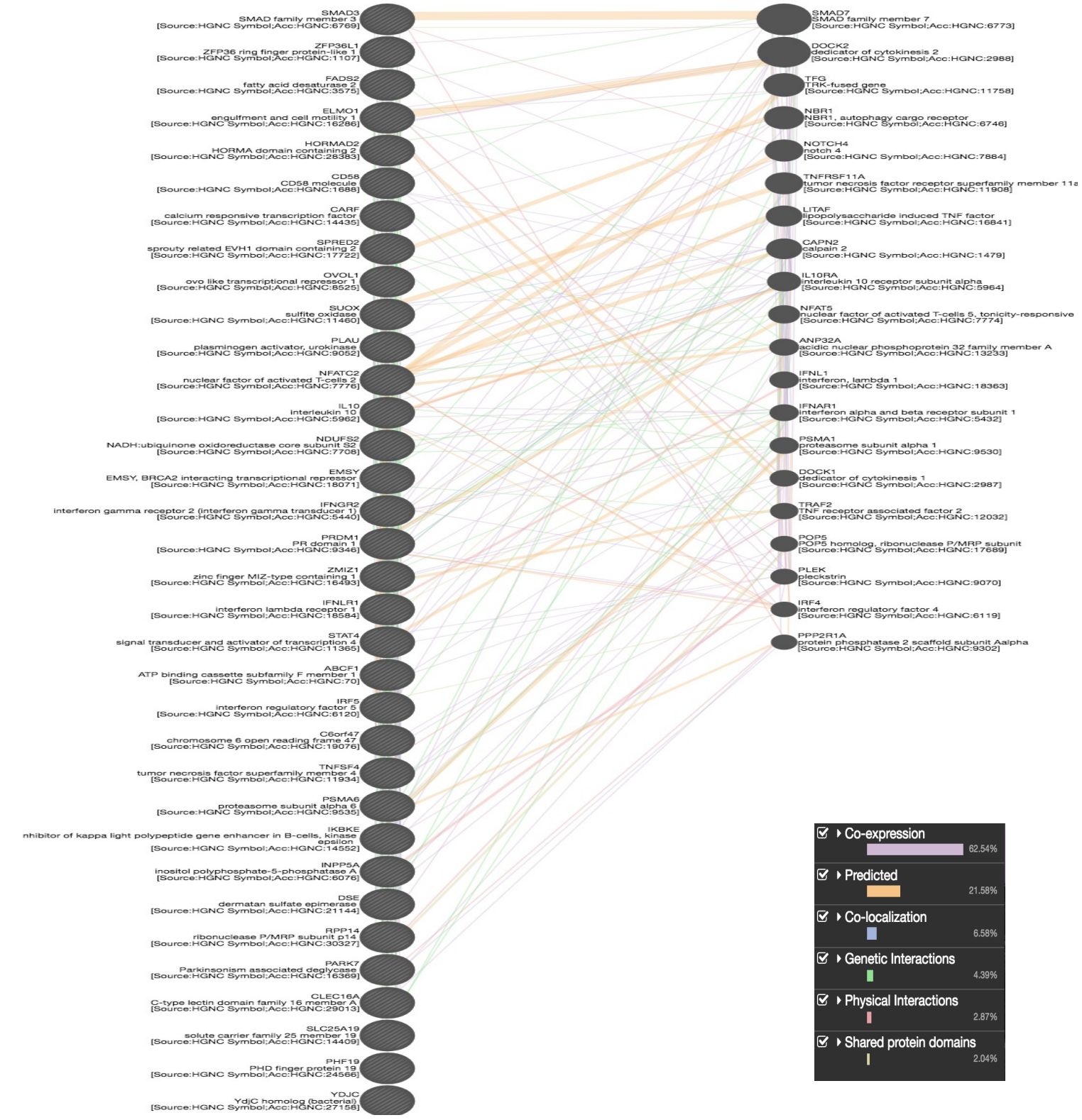

Untreated
IgE
IgE + anti-IgE
H3K27ac
H3K4me3
ATAC-seq ToMC
Read Depth
chr7
76824
76826
76828
Kb
FGL2


Untreated
IgE
IgE + anti-IgE
H3K27ac
H3K4me3
ATAC-seq ToMC
Read Depth
chr11
67135
67140
Kb
CLCF1

Supplementary Figure-6: Comparison of CHIP-seq peaks of peripheral blood-derived MCs with Omni-ATAC-seq peaks of tonsillar MCs. Related to Fig-1.

H3K27ac and H3K4me3 CHIP-seq peaks of peripheral blood-derived MCs were compared with Omni-ATAC-seq peaks of tonsillar MCs in indicated gene regions.

Figure-S7


SMAD3
SMAD family member 3
[Source:HGNC Symbol;Acc:HGNC:6769]
ZFP36L1
ZFP36 ring finger protein-like 1
[Source:HGNC Symbol;Acc:HGNC:1107]
FADS2
fatty acid desaturase 2
[Source:HGNC Symbol;Acc:HGNC:3575]
ELMO1
engulfment and cell motility 1
[Source:HGNC Symbol;Acc:HGNC:16286]
HORMAD2
HORMA domain containing 2
[Source:HGNC Symbol;Acc:HGNC:28393]
CD58
CD58 molecule
[Source:HGNC Symbol;Acc:HGNC:1688]
CARF
calcium responsive transcription factor
[Source:HGNC Symbol;Acc:HGNC:14435]
SPRED2
sprouty related EVH1 domain containing 2
[Source:HGNC Symbol;Acc:HGNC:17722]
OVOL1
ovo like transcriptional repressor 1
[Source:HGNC Symbol;Acc:HGNC:8525]
SUOX
sulfite oxidase
[Source:HGNC Symbol;Acc:HGNC:11460]
PLAU
plasminogen activator, urokinase
[Source:HGNC Symbol;Acc:HGNC:9052]
NFATC2
nuclear factor of activated T-cells 2
[Source:HGNC Symbol;Acc:HGNC:7776]
IL10
interleukin 10
[Source:HGNC Symbol;Acc:HGNC:5962]
NDUFS2
NADH:ubiquinone oxidoreductase core subunit S2
[Source:HGNC Symbol;Acc:HGNC:7708]
EMSY
EMSY, BRCA2 interacting transcriptional repressor
[Source:HGNC Symbol;Acc:HGNC:18071]
IFNGR2
interferon gamma receptor 2 (interferon gamma transducer 1)
[Source:HGNC Symbol;Acc:HGNC:5440]
PRDM1
PR domain 1
[Source:HGNC Symbol;Acc:HGNC:9346]
ZMIZ1
zinc finger MIZ-type containing 1
[Source:HGNC Symbol;Acc:HGNC:16493]
IFNLR1
interferon lambda receptor 1
[Source:HGNC Symbol;Acc:HGNC:18584]
STAT4
signal transducer and activator of transcription 4
[Source:HGNC Symbol;Acc:HGNC:11365]
ABCF1
ATP binding cassette subfamily F member 1
[Source:HGNC Symbol;Acc:HGNC:70]
IRF5
interferon regulatory factor 5
[Source:HGNC Symbol;Acc:HGNC:6120]
C6orf47
chromosome 6 open reading frame 47
[Source:HGNC Symbol;Acc:HGNC:19076]
TNFSF4
tumor necrosis factor superfamily member 4
[Source:HGNC Symbol;Acc:HGNC:11934]
PSMA6
proteasome subunit alpha 6
[Source:HGNC Symbol;Acc:HGNC:9535]
IKBKE
nhibitor of kappa light polypeptide gene enhancer in B-cells, kinase epsilon
[Source:HGNC Symbol;Acc:HGNC:14552]
INPP5A
inositol polyphosphate-5-phosphatase A
[Source:HGNC Symbol;Acc:HGNC:6076]
DSE
dermatan sulfate epimerase
[Source:HGNC Symbol;Acc:HGNC:21144]
RPP14
ribonuclease P/MRP subunit p14
[Source:HGNC Symbol;Acc:HGNC:30327]
PARK7
Parkinsonism associated deglycase
[Source:HGNC Symbol;Acc:HGNC:16369]
CLEC16A
C-type lectin domain family 16 member A
[Source:HGNC Symbol;Acc:HGNC:29013]
SLC25A19
solute carrier family 25 member 19
[Source:HGNC Symbol;Acc:HGNC:14409]
PHF19
PHD finger protein 19
[Source:HGNC Symbol;Acc:HGNC:24566]
YDJC
YdjC homolog (bacterial)
[Source:HGNC Symbol;Acc:HGNC:27158]
SMAD7
SMAD family member 7
[Source:HGNC Symbol;Acc:HGNC:6773]
DOCK2
dedicator of cytokinesis 2
[Source:HGNC Symbol;Acc:HGNC:2988]
TFG
TRK-fused gene
[Source:HGNC Symbol;Acc:HGNC:11758]
NBR1
NBR1, autophagy cargo receptor
[Source:HGNC Symbol;Acc:HGNC:6746]
NOTCH4
notch 4
[Source:HGNC Symbol;Acc:HGNC:7884]
TNFRSF11A
tumor necrosis factor receptor superfamily member 11a
[Source:HGNC Symbol;Acc:HGNC:11908]
LITAF
lipopolysaccharide induced TNF factor
[Source:HGNC Symbol;Acc:HGNC:16841]
CAPN2
calpain 2
[Source:HGNC Symbol;Acc:HGNC:1479]
IL10RA
interleukin 10 receptor subunit alpha
[Source:HGNC Symbol;Acc:HGNC:5964]
NFAT5
nuclear factor of activated T-cells 5, tonicity-responsive
[Source:HGNC Symbol;Acc:HGNC:7774]
ANP32A
acidic nuclear phosphoprotein 32 family member A
[Source:HGNC Symbol;Acc:HGNC:13233]
IFNL1
interferon, lambda 1
[Source:HGNC Symbol;Acc:HGNC:18363]
IFNAR1
interferon alpha and beta receptor subunit 1
[Source:HGNC Symbol;Acc:HGNC:5432]
PSMA1
proteasome subunit alpha 1
[Source:HGNC Symbol;Acc:HGNC:9530]
DOCK1
dedicator of cytokinesis 1
[Source:HGNC Symbol;Acc:HGNC:2987]
TRAF2
TNF receptor associated factor 2
[Source:HGNC Symbol;Acc:HGNC:12032]
POP5
POP5 homolog, ribonuclease P/MRP subunit
[Source:HGNC Symbol;Acc:HGNC:17689]
PLEK
pleckstrin
[Source:HGNC Symbol;Acc:HGNC:9070]
IRF4
interferon regulatory factor 4
[Source:HGNC Symbol;Acc:HGNC:6119]
PPP2R1A
protein phosphatase 2 scaffold subunit Aalpha
[Source:HGNC Symbol;Acc:HGNC:9302]
Co-expression
62.54%
Predicted
21.58%
Co-localization
6.58%
Genetic Interactions
4.39%
Physical Interactions
2.87%
Shared protein domains
2.04%

Supplementary Figure-7: Network analysis of genes harbouring disease-associated SNPs located in Omni-ATAC-seq peaks of tonsillar MCs. Related to Fig-7.

Network analysis of genes harbouring SNPs located in Omni-ATAC-seq peaks of tonsillar MCs using GeneMANIA tool. This analysis showed whether the indicated proteins are co-expressed, have predicted interactions, take part in same biological pathways, have shared protein domains, are colocalized or have known physical interactions.